國立臺灣大學電機資訊學院電子工程學研究所

碩士論文

Graduate Institute of Electronics Engineering

College of Electrical Engineering and Computer Science

National Taiwan University

Master Thesis

鍺錫/鍺異質結構二維電洞氣之 Rashba 自旋-軌域耦合

效應與等效質量

Rashba spin-orbit coupling and effective mass of two-dimensional hole gases in GeSn/Ge heterostructures

戴嘉澤

Chia-Tse Tai

指導教授：李峻霣 教授

Advisor: Professor Jiun-Yun Li

中華民國 110 年 1 月

January, 2021

i

國立臺灣大學碩士學位論文
口試委員會審定書

鍺錫/鍺異質結構二維電洞氣之 Rashba 自旋-軌域耦合效應與等效質量

Rashba spin-orbit coupling and effective mass of two-dimensional hole gases in GeSn/Ge heterostructures

本論文係戴嘉澤君（R07943077）在國立臺灣大學電子工程學研究所完成之碩士學位論文，於民國 110 年 1 月 20 日承下列考試委員審查通過及口試及格，特此證明

口試委員：

（指導教授）

系主任、所長

1

致謝

　　首先一定要先感謝李峻賞教授在我碩士班兩年半的時間細心指導。教授認真教導了我正確的實驗態度以及嚴謹的推理邏輯，讓我在碩士班實驗的結果有完整討論足以發表。此外也感謝教授給予我機會到美國 Sandia National Laboratories 做短期研究，讓我能夠在美國國家實驗室接受最頂尖的研究學者的指導，此趟經驗實屬難得。也特別感謝盧子敏博士在我於美國期間給我生活上以及研究上的幫助，以及願意在百忙之中替我寫推薦信協助我申請國外學校的博士班。若是沒有李教授和盧博士的指導，我也無法擁有投稿期刊論文、參加國際會議等學術經驗。也謝謝口試委員在口試時的提點，讓我發現自己的不足以及論文可以精進的地方。

　　在 QEL 的日子中，感謝實驗室的學長姊以及學弟妹們。謝謝家佑(大劉)學長跟莊嚴學長時常教我有關磊晶的知識，讓我對於自己的研究有更全面的了解。謝謝韋志學長時常跟我一起在 437 熬夜討論物理或是實驗，在我壓力很大的時候當我的垃圾桶，拉我一把。也謝謝祥順學長在實驗上的幫助。謝謝已畢業的學長姊柏元、家佑(小劉)、立耘、乃文以及崇道，在我剛進 QEL 的時候教我許多實驗撒步跟凝態物理的相關知識。尤其感謝柏元學長，教了我好多有趣的物理以及提供我想法。也感謝我的同學子茗、志穎、燿均以及俞叡，謝謝你們陪我聊天以及分享了自己的專業，讓我對於整個量子計算有更清楚概念。也謝謝學弟妹：凱鴻、承育、志力、宗穎、凱瑩、菖浚、蘇遙、宸嶢、奕潔、士傑、以琳、驊凌、睿濬、瑋哲、閎宇。相信你們未來一定無可限量。

　　再來謝謝我的高中好友們，整個大學跟碩士班期間帶給我許多快樂。最後感謝我的家人們，謝謝你們一直在我背後鼓勵跟支持我，讓我沒有後顧之憂的可以努力往前衝。也謝謝在台北的兩個堂姊對我的照顧。

　　兩年半的 QEL 生涯結束了，一路上我認為自己承接了太多的好運，也受到了無數的人的幫助。最後期許自己在未來也可以成為有能力協助他人的人。

摘要

自旋電子元件因為其低功耗的特性而被視為極具發展性的元件，如自旋電晶體和磁阻式記憶體。透過自旋–軌域耦合效應，我們可以利用外加電場操控電子自旋態，此外，自旋–軌域耦合效應也被利用在自旋量子位元中，藉以達到高速量子計算。在四族材料中，鍺錫因為較大的自旋–軌域耦合效應及較小的等效質量，而被視為具發展潛力的自旋電子材料，然而，迄今尚未有文獻探討關於鍺錫薄膜的量子傳輸性質。

在本論文中，三種無摻雜且錫比例分別為 6%、9% 及 11% 的鍺錫/鍺異質結構，經由化學氣相沉積磊晶而成。我們將樣品製作成具閘極之霍爾棒元件，在低溫系統量測其量子傳輸性質，並探討了這些無摻雜鍺錫/鍺異質結構中所形成的二維電洞氣電性以及磁傳輸特性，並首次在無摻雜鍺錫系統中展現高遷移率的二維電洞氣。我們透過 Shubnikov-de Haas 振盪震幅隨溫度的關係萃取出二維電洞氣的等效電洞質量，並發現等效質量(從 0.07 m_0 到 0.10 m_0)隨電洞濃度(從 2.7×10^{11} cm^{-2} 到 6.1×10^{11} cm^{-2})線性增加。我們將等效質量隨電洞濃度上升的趨勢歸因於鍺錫量子井中價帶的非拋物線性，這三種鍺錫/鍺異質結構(錫比例為 6%、9% 及 11%)的非拋物線性因子分別為 8.0 eV^{-1}、4.9 eV^{-1} 及 4.0 eV^{-1}。等效質量和非拋物線性因子在較高錫比例的鍺錫異質結構中較小，我們認為這起因於高錫濃度所造成的壓縮應變，導致價帶結構中的重電洞能帶有較大的形變且增加了重電洞能帶和輕電洞能帶之間的能量差。

我們亦探討了這三種鍺錫/鍺異質結構中的 Rashba 自旋–軌域耦合效應。透過量測低溫磁導率隨磁場變化並利用 Hikami-Larkin-Nagaoka (HLN)公式擬合實驗數據點，可萃取相位同調時間(phase-coherence time)、自旋鬆弛時間(spin-relaxation time)、自旋進動時間(spin-precession time)、k 立方 Rashba 參數(k-cubic Rashba coefficient)以及自旋能帶分裂能量(spin-splitting energy)。我們驗證了 Rashba 自旋–

軌域耦合效應隨閘極偏壓的可調性,並得到在目前所有四族材料中最大的 Rashba 自旋-軌域耦合強度。同時,我們也發現 Rashba 自旋-軌域耦合效應有隨錫比例增加而減弱的趨勢,我們將此歸因於壓縮應變對 Rashba 自旋-軌域耦合效應的影響。較大的壓縮應變增強了角動量在磊晶成長方向(z)的量子化效應,進而抑制了由自旋-軌域耦合效應產生的等效磁場所造成的在量子井平面(x-y)的量子化效應。最後,我們藉由相位同調時間和溫度的關係,探討在鍺錫/鍺異質結構中二維電洞氣的退相干(de-phasing)機制,實驗結果顯示相位同調時間和溫度倒數成正比,其退相干機制主要為電洞-電洞之間的非彈性散射。
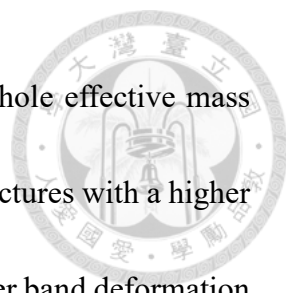
關鍵字: 鍺錫/鍺異質結構、二維電洞氣、磁傳輸性質、等效電洞質量、Rashba 自旋-軌域耦合效應、非拋物線性、Shubnikov-de Haas 震盪

Abstract

Spintronic devices such as spin field-effect transistors (FETs) and magneto-resistive random access memory (MRAM) are promising due to their low power consumption for the manipulation of spins. Spin-orbit coupling (SOC) provides a way to control the spin states through electrical gating. In addition, SOC also plays an important role in spin-based quantum computing, which enables fast spin qubit operations. Among group-IV materials, GeSn is a promising candidate for its physical properties such as expected larger SOC effect and smaller effective mass. However, there are few works on the quantum-transport properties of GeSn-based undoped heterostructures.

In this thesis, three undoped GeSn/Ge heterostructures with different Sn fractions of 6%, 9%, and 11% are epitaxially grown by chemical vapor deposition and gated Hall bar devices are fabricated for magneto-transport measurements at cryogenic temperatures. We investigate both the electro- and magneto-transport properties of the undoped GeSn/Ge heterostructures and demonstrate the first two-dimensional hole gas in this material system by gating. Hole effective masses are extracted from the temperature-dependent amplitudes of Shubnikov-de Haas oscillations, and it increases linearly from $0.07\ m_0$ to $0.10\ m_0$ as the carrier density varies from 2.7×10^{11} cm^{-2} to 6.1×10^{11} cm^{-2}. We attribute the effective mass increment to the non-parabolicity effect on the valence band with the non-parabolicity factor of 8.0 eV^{-1}, 4.9 eV^{-1}, and 4.0 eV^{-1} for the

$Ge_{0.94}Sn_{0.06}$, $Ge_{0.91}Sn_{0.09}$, $Ge_{0.89}Sn_{0.11}$ devices, respectively. Both the hole effective mass and the non-parabolicity factor are smaller in the GeSn/Ge heterostructures with a higher Sn fraction due to the larger compressive strain, which leads to a larger band deformation and energy splitting between the heavy-hole and light-hole bands.

We also studied the Rashba SOC effect in the GeSn/Ge heterostructures. Magneto-conductivity is measured and fitted to the Hikami-Larkin-Nagaoka (HLN) model. Phase-coherence time, spin-relaxation time, spin-precession time, k-cubic Rashba coefficient, and spin-splitting energy are extracted. We demonstrate the tunability of the Rashba SOC strength through gating and the strongest Rashba SOC among all group-IV materials. As the Sn fraction increases, the Rashba SOC strength becomes weaker, which is attributed to the effect of strain. The stronger compressive stain in higher Sn device enhances the quantization of angular momentum along the growth (z) direction instead along the direction of an SOC-induced magnetic field (x-y plane). The de-phasing mechanism is also investigated and the relation between phase-coherence time (τ_ϕ) and temperature ($\tau_\phi \propto T^{-1}$) suggests the dominant de-phasing mechanism is hole-hole scattering.
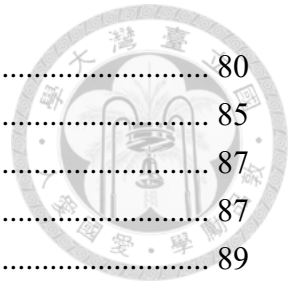
Keywords: GeSn/Ge heterostructures, two-dimensional hole gas (2DHG), magneto-transport property, hole effective mass, Rashba spin-orbit coupling (SOC), non-parabolicity, Shubnikov-de Hass (SdH) oscillations
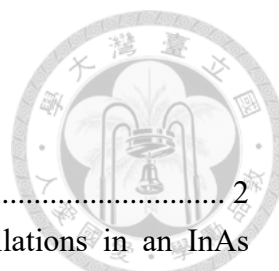
Contents

List of Figures

List of Tables

Chapter 1

Introduction

1-1 Motivation

The development of complementary metal-oxide-semiconductor (CMOS) technology has followed Moore's law for the past decades with doubling transistor numbers every two years. The requirements of high performance and energy saving may hamper CMOS scaling beyond the 1-nm technology node due to physical limitations such as short-channel effects, gate leakage, or subthreshold swing by Boltzmann tyranny [1]. Spintronics, on the other hand, is promising for more-than-Moore applications due to the low-power nature and its compatibility with Si VLSI technology [2]. For example, spin-based magnetoresistive random access memory (MRAM) is considered a promising candidate for a next-generation embedded memory [3] with spin states manipulated by spin-transfer torque (STT) [4] or spin-orbit coupling (SOC) [5]. Another interesting spin device is the spin-field-effect transistor (FET) [2, 6] whose "1" and "0" states are represented by spin orientations (Fig. 1-1) and controlled by SOC [2]. The advantage of a spin-FET is the low energy required to flip the spins, namely, to switch on/off the device via SOC [7]. However, only few works on spin-FETs were reported [8, 9] and group-IV materials are not an ideal candidate for spin-FETs owing to its weak SOC effect [10].

$\text{ON} \quad \theta = 0 \quad \alpha(V_{g1}) = 0$

$\text{OFF} \quad \theta = \dfrac{2\alpha(V_{g2})m^*}{\hbar^2}L = \pi$
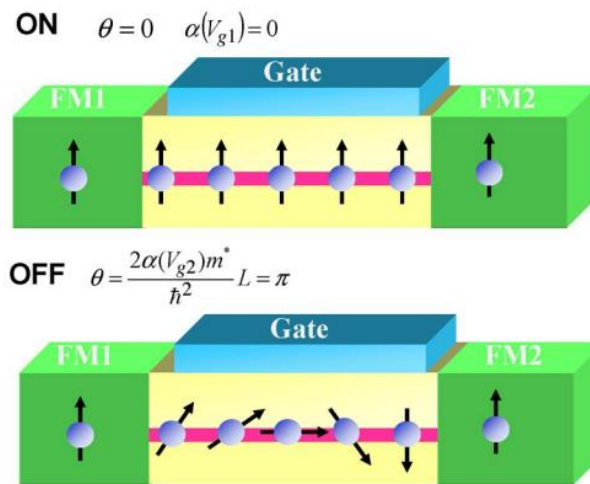
Fig. 1-1 Operation principles of a spin-FET [2].

In addition to the spin-based logic and memory devices, SOC also plays an important

role in spin-based quantum computing [11], which use the superposition of the spin states

to define the quantum bit "1" or "0". Through the coupling between spins and an electric

field, we can manipulate the spin states via gating. In 2010, the group led by

Kouwenhoven at TU Delft demonstrated a spin-orbit qubit on an InAs nanowire [12].

They built a double quantum dot structure through five gates. Fig. 1-2 (a) shows the

scanning electron microscope (SEM) image. They manipulated the spin states through

the SOC effect, achieving the highest Rabi frequency up to 58 MHz (Fig. 1-2 (b)). In

2020, the group led by M. Veldhorst at TU Delft demonstrated Ge quantum dots with two

qubits [13] (Fig. 1-2 (c)). With the strong SOC effect in Ge [14], they achieved the highest

Rabi frequency up to 100 MHz (Fig. 1-2 (d)), showing the potential of high-speed spin

qubits by SOC. To further enhance the SOC strength for device applications, materials
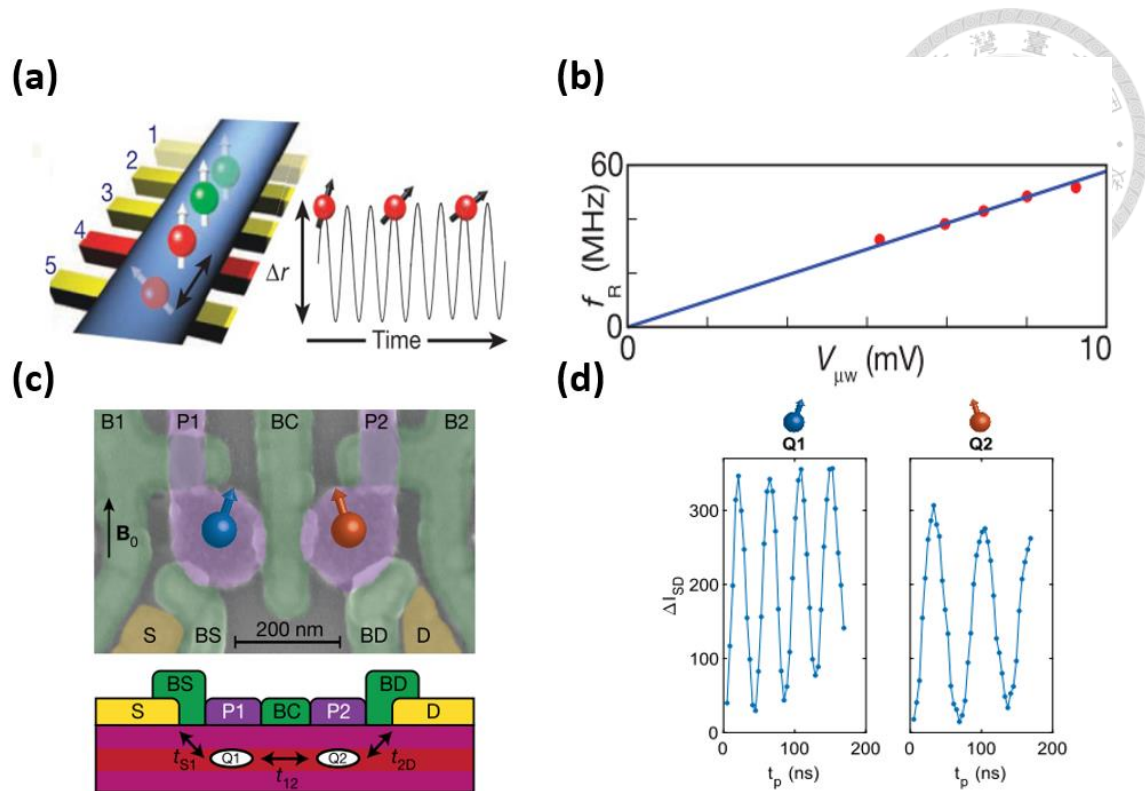
Fig. 1-2 Schematic of a Ge double quantum dots and Rabi oscillations in an InAs nanowire device. (b) The Rabi frequency (f_R) versus driving amplitude ($V_{\mu w}$) [12]. (c) Schematic of a Ge double quantum dots. (d) Rabi oscillation of two spin qubits [13].

with higher atomic numbers are preferred due to larger atomic potential variations [15].

Thus, one would expect incorporation of tin (Sn) atoms into germanium (Ge) crystals to

be a viable strategy to achieve stronger SOC [16]. Besides, GeSn is highly compatible to

Si VLSI technology [17], which has motivated us to investigate the SOC effects in GeSn

for future applications of spintronic and spin-based quantum computing devices.

3

1-2 Two-dimensional carrier systems

Two-dimensional carrier system is a platform for the realization of a spin-FET [2] and quantum computing devices [13]. A two-dimensional carrier system can be either a two-dimensional electron gas (2DEG) or a two-dimensional hole gas (2DHG), depending on the carrier type. It can be formed at the oxide interface in a metal-oxide-semiconductor structure (MOS) (Fig. 1-3 (a)) or a semiconductor heterostructure (Fig. 1-3 (b)). The carriers in a heterostructure are away from the oxide interface, which suppresses the interface scattering and leads to a higher mobility. The highest reported mobility of 2DEG is 3.5×10^7 cm^2/Vs in a modulation-doped GaAs/AlGaAs heterostructure [18]. In group-IV heterostructures, the highest mobility is 2.4×10^6 cm^2/Vs in an undoped Si/SiGe heterostructure [19]. The presence of Dresselhaus SOC in III-V materials leads to difficulty in an effective external control and the non-zero nucleus spins degrade the
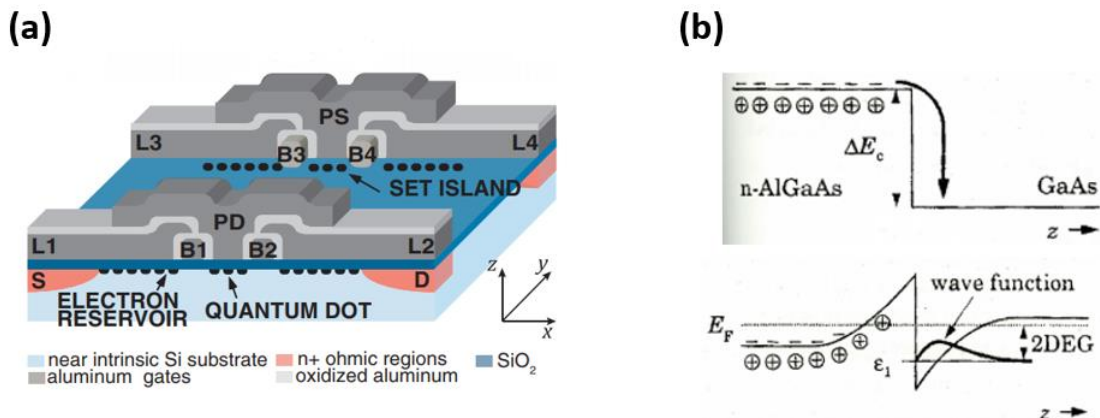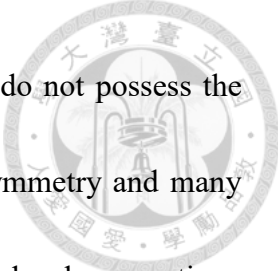
Fig. 1-3 Two-dimensional carrier system in (a) a MOS structure [20] or (b) a semiconductor heterostructure [21].

4

spin-decoherence time [22]. On the other hand, group-IV materials do not possess the Dresselhaus SOC features because of the lack of bulk inversion asymmetry and many spinless isotopes are available in nature [23] to suppress the spin decoherence time. Besides, the mature Si VLSI technology could enable large-scale quantum computing devices. Therefore, many research groups focus on the two-dimensional carrier systems in group-IV materials [13, 24-30].

To control the SOC strength externally via gating, the Rashba SOC effect is commonly used. While the Rashba SOC effect is very weak in Si [31]. A Ge-based 2DHG is a promising candidate for future quantum devices for its many superior physical properties such as high carrier mobility [32], strong SOC strength [14], and compatibility to Si VLSI technology [17]. A large Rashba SOC strength in Ge enables the spin qubits to be manipulated electrically through electric dipole spin resonance (EDSR), achieving high speed qubit operation [13]. Research groups at TU Delft have demonstrated a fast two-qubit [13] and the first four-qubit systems [24] in Ge-based 2DHGs among all semiconductor platforms. Furthermore, a large out-of-plane g-factor of ~ 28 was also reported [33]. The hole effective mass is expected to be lower than that in Si and a value of 0.08 m_0 has been reported in Ref. [34]. Under a strong compressive strain, it further reduced to 0.035 m_0 [35] because of the deformation of the valence bands.
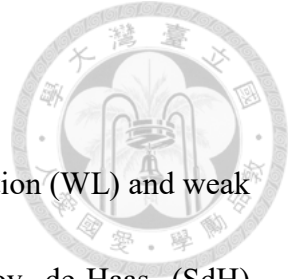
1-3 Rashba spin-orbit coupling

The Rashba SOC strength can be extracted by the weak localization (WL) and weak anti-localization (WAL) patterns [36] or beatings of Shubnikov de-Haas (SdH) oscillations [37]. The group in the University of Tokyo observed both WL and WAL patterns in a strained Ge quantum well and extracted the Rashba spin-splitting energy through the fitting to a k-cubic model in 2014 [36]. Fig. 1-4 (a) shows the magneto-conductivity versus magnetic field under different gate biases and a transition from WL to WAL is observed. Fig. 1-4 (b) shows the fitting results by a k-linear model (blue-dashed line) while the red-solid line represents the results by a k-cubic model. The Rashba SOC has k-linear dependence for LH band and k-cubic dependence for HH band. Only the k-cubic model gives the reasonable fitting results, which suggests that the carriers in the HH band contribute to the Rashba SOC effect in Ge. The extracted spin-splitting energy (Δ) varies from 0.3 meV to 0.39 meV as the density increases from 1×10^{12} cm^{-2} to 1.5×10^{12} cm^{-2} (Fig. 1-4 (c)), showing the tunability of the Rashba SOC strength through gating.
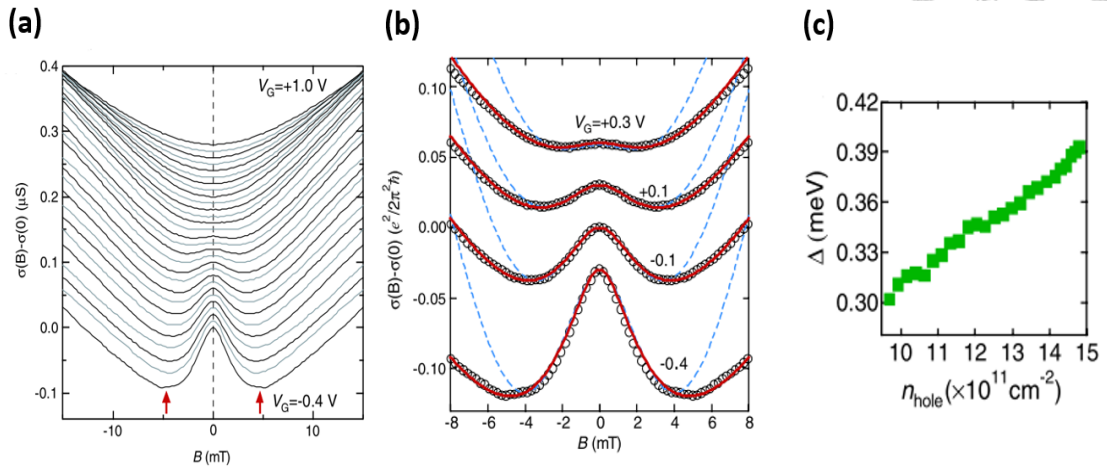
Fig. 1-4 (a) Magneto-conductivity versus magnetic field under varies gate voltages and (b) the fitting results by a k-linear relation (blue-dashed line) and a k-cubic model (red-solid line). (c) The extracted Rashba spin-splitting energy versus carrier density [36].

In 2014, the group in Warwick University extracted the Rashba spin-splitting energy through the beatings in SdH oscillations in a strained Ge quantum well by a modulation doped technique [37]. Fig. 1-5 shows their epitaxial structure and SdH oscillations with the inset presenting the Fourier transformation results of the sheet resistance. In the Fourier transformation spectrum, the first or second peak corresponds to the carrier density in the first or second spin-subband ($p_\uparrow$ or $p_\downarrow$). The third peak corresponds to the total carrier density ($p_\uparrow + p_\downarrow$). The Rashba coefficient is estimated by the following equation:

$$\beta_{so} = \sqrt{\frac{2}{\pi}} \frac{\hbar^2}{2m^*} \frac{p(p_+ - p_-) + \Delta p(p_+ + p_-)}{6p^2 + 2\Delta p^2} \qquad \text{Eq. 1-1}$$

p is the sum of the hole densitites in the spin-up and spin-down subbands and Δp is the difference between them. $p_\pm$ is defined as $\sqrt{p \pm \Delta p}$. The resulting Rashba spin-splitting energy is listed in Table 1-1 with other materials.

7
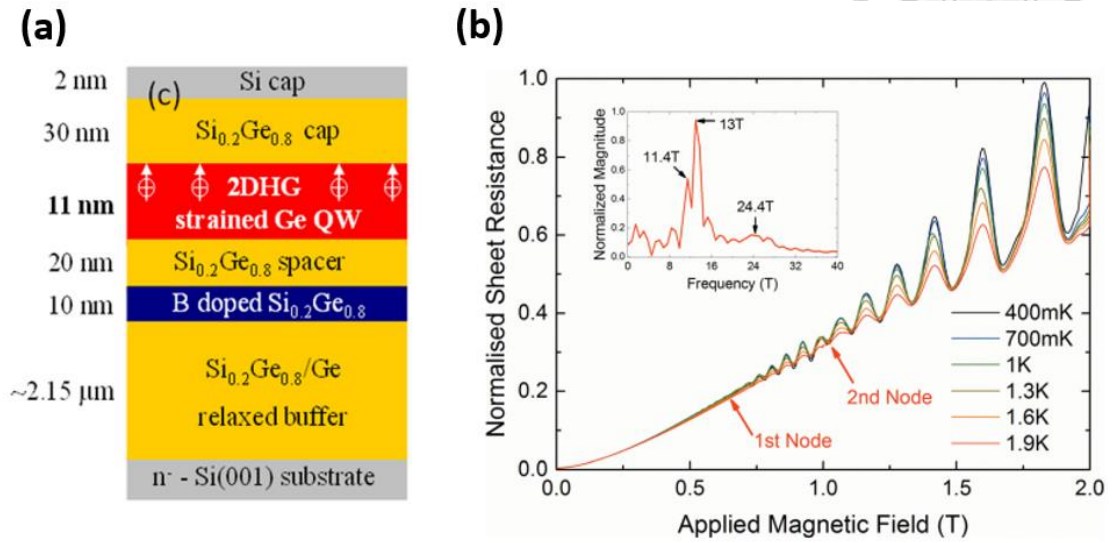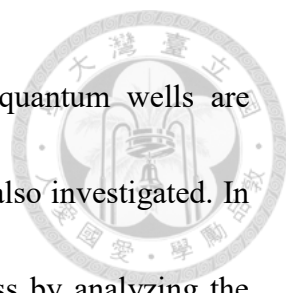
Fig. 1-5 (a) Schematic of a Ge/GeSi heterostructure and (b) the measured SdH oscillations at different temperatures. The inset shows the Fourier transformation results of the sheet resistance [37].

Table 1-1 Low-temperature mobility, Rashba coefficient, Rashba spin-splitting energy, and the strain condition of different heterostructures Refs. [31, 36-41].

	AlGaN /GaN 2DEG[8] (L)	GaSb /InAs 2DEG[9,10] (L)	InGaAs /InAlAs 2DEG[11] (L)	Ge 2DHG (C)	Ge 2DHG (C)[24]	Si 2DEG[23] (L)
Low Temperature Mobility (cm²/Vs)	…	~20 000	95 000	450 000	~5 000	200 000
Rashba spin-orbit parameter α or β	8.1×10^{-12} eVm	9×10^{-12} eVm	4×10^{-12} eVm	1.0×10^{-28} eVm³	0.2×10^{-28} eVm³	5.5×10^{-15} eVm
Rashba spin-orbit energy (meV)	11.6	4.0	2.50	1.4	0.30	~0.001
Lattice mis-match strain	…	…	…	0.8%	2.1%	…

1-4 Thesis outline

In this thesis, we investigate the properties of electro-transport, magneto-transport, effective mass, and the Rashba SOC effect in three GeSn/Ge heterostructures with different Sn fractions. The thesis is outlined as follows: in chapter 2, the physical background of 2DHGs, SOC effect, and WL/WAL patterns are introduced. In chapter 3, gated Hall bars devices are fabricated and characterized by Hall measurements at

cryogenic temperatures. Effective masses of holes in the GeSn quantum wells are extracted and the non-parabolicity effects on the effective mass are also investigated. In chapter 4, the Rashba SOC effects in the GeSn/Ge heterostructuress by analyzing the WL/WAL patterns are demonstrated. Both the density and temperature dependence of WL/WAL features are presented and the magneto-conductivity is fit by an Hikami-Larkin-Nagaoka (HLN) model. As the Sn fraction in GeSn increases, the strength of Rashba SOC is reduced, which is attributed to the competition between the z-direction quantization by compressive strain and the in-plane direction quantization by SOC-induced effective magnetic field. Finally, a summary of this thesis and future work are given in chapter 5.

Chapter 2

Background of Two-Dimensional Hole Gases and Spin-Orbit Coupling

2-1 Two-dimensional hole gas (2DHG) in Ge

Two-dimensional hole gases (2DHGs) can be formed in a Ge/GeSi heterostructure [42] or a GeSn/Ge heteorstructure [43] based on the valence band offset. The band alignments of strained $Si_{1-x}Ge_x$ on relaxed $Si_{1-y}Ge_y$ [44] and strained $Ge_{1-x}Sn_x$ on relaxed $Ge_{1-y}Sn_y$ [45] are shown in Fig. 2-1. A square quantum well is expected to form in the Ge/GeSi and GeSn/Ge heterostructures.

There are two ways to provide holes into the quantum wells. One is to use the modulation-doped structure (Fig. 2-2 (a)) and the other is the undoped structure by top gating (Fig. 2-2 (b)). The device fabrication process is simpler for the modulation-
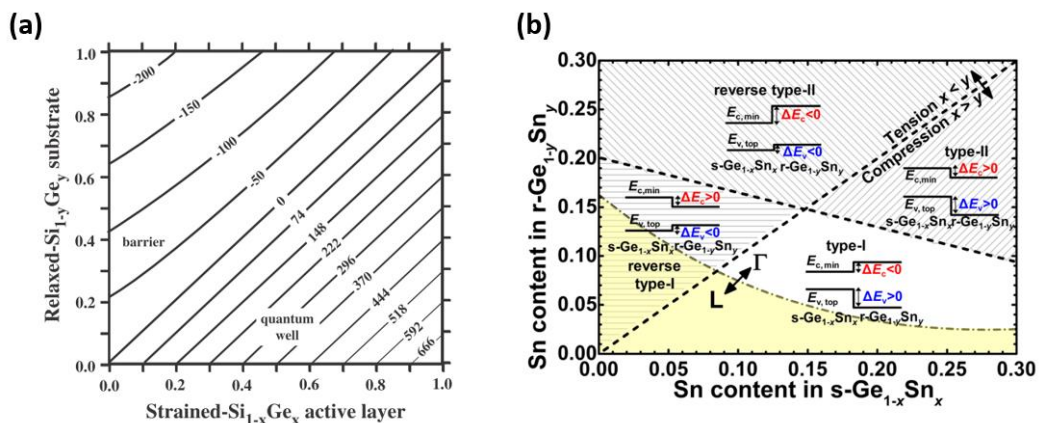
Fig. 2-1 Band alignments of (a) strained $Si_{1-x}Ge_x$ on relaxed $Si_{1-y}Ge_y$ [44] and (b) strained $Ge_{1-x}Sn_x$ on relaxed $Ge_{1-y}Sn_y$ [45].
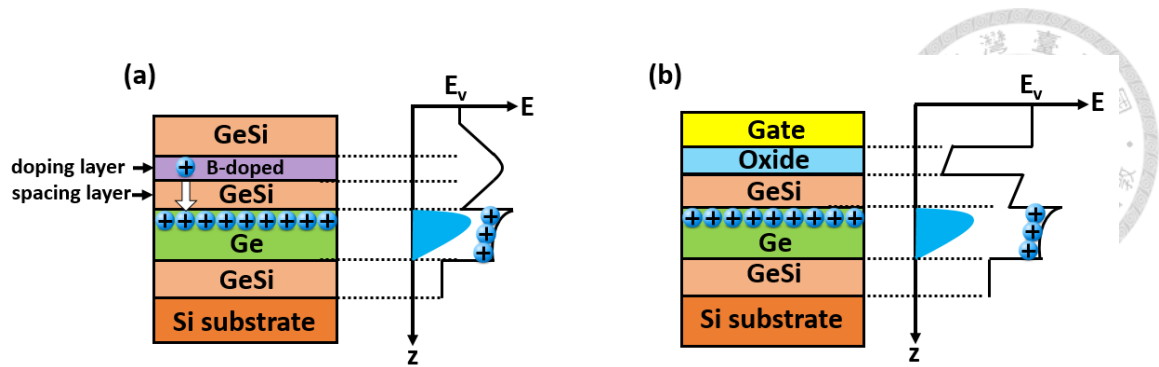
Fig. 2-2 Ge-based two-dimensional hole gas in (a) a modulation-doped structure and (b) an undoped structure by top gating.

doped structure, but the carrier density is fixed. To tune the carrier density in the modulation-doped devices, we need to change the doping concentration in the doped layer or the thickness of the spacing layer (Fig. 2-2 (a)), which requires multiple growths for different epitaxial structures. While we can deposit a metal/oxide gate or a Schottky gate to tune the carrier density, it suffers from the ineffectiveness of gate control [46] or severe gate leakage [47]. Another disadvantage of the modulation-doped structure is the ionized impurities in the doping layer, which cause remote charged impurities scattering and reduce the carrier mobility in the quantum well [48]. In an undoped structure, holes can be induced and accumulated in the quantum well by applying a negative gate bias. The carrier density can be tuned capacitively [49] and the gate leakage issue can be effectively suppressed [50], but the device fabrication is more complicated compared to the modulation-doped structures. In this work, we focus on 2DHG in the undoped GeSn/Ge heterostructures.

2-2   Shubnikov-de Haas oscillation and integer quantum Hall effect

According to the Drude model [51], the longitudinal resistance (ρ_{xx}) is invariant to the magnetic field while the transverse resistance (ρ_{xy}) changes linearly with the magnetic field. However, as the magnetic field increases, the longitudinal resistance starts to oscillate, which is called Shubinkov-de Haas (SdH) oscillation, and the emergence of plateaus in transverse resistance is referred to the integer quantum Hall effect (Fig. 2-3).

The oscillation behavior of longitudinal resistance is due to the formation of the quantized Landau levels. At a zero magnetic field, the density of states (DOS) in a two-dimensional system is independent of energy and proportional to the effective mass (Fig. 2-4 (a)) [21]. Discrete Landau levels are formed when a magnetic field is applied
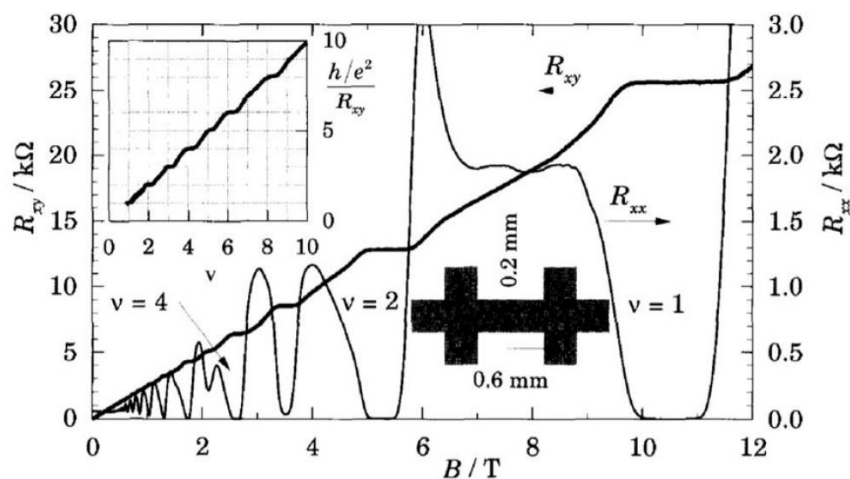
Fig. 2-3 Shubinkov-de Haas oscillations and integer quantum Hall effect. Inset: Transverse resistance versus filling factor [21].

12
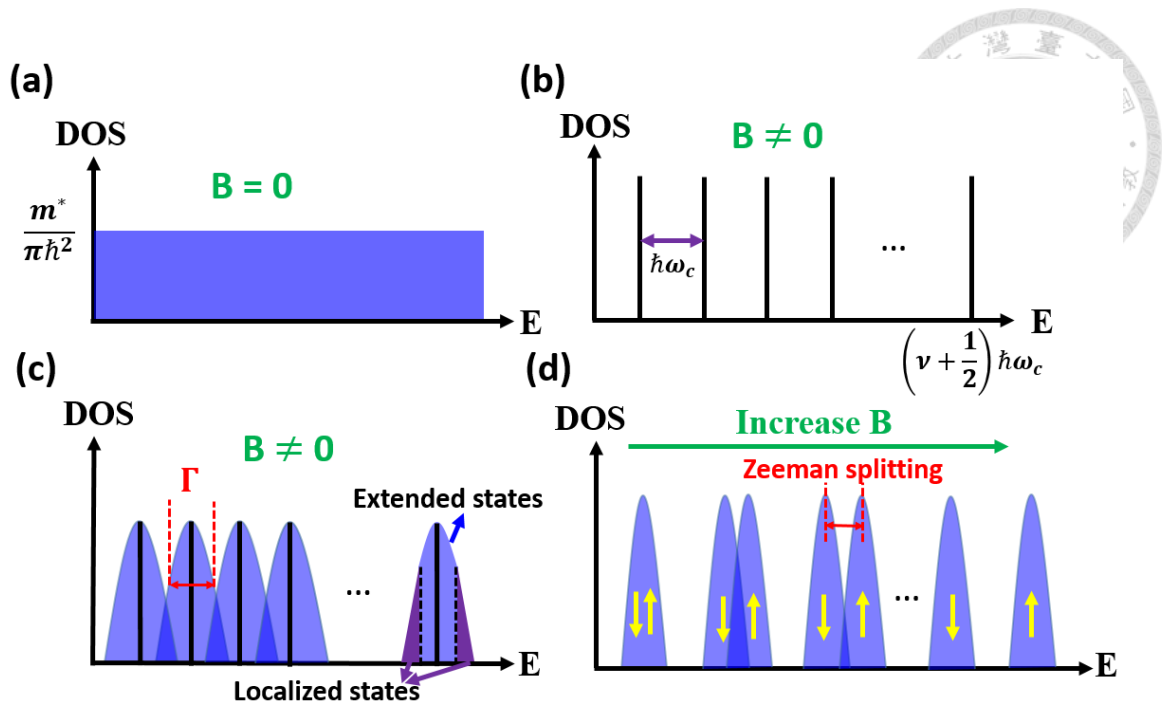
Fig. 2-4 (a) The density of states for a two-dimensional system with a zero magnetic filed and (b) a finite magnetic field. (c) Landau level broadening. (d) The physical picture of Zeeman splitting.

(Fig. 2-4 (b)). For the νth Landau level, its energy is $\left(\nu + \frac{1}{2}\right)\hbar\omega_c$, and the Landau level is equally spaced with an energy difference of $\hbar\omega_c$, where ω_c is the cyclotron frequency ($\omega_c = eB/m^*$). ν is called the filling factor, indicating the number of highest occupied Landau level. In an ideal case, the DOS in a two-dimensional system under a magnetic field would be a series of delta-functions with the degeneracy of eB/h for each Landau levels (or $2eB/h$ if spin-degeneracy is ignored.). However, in real situations, the Landau levels would be broadened with an energy scale of $\Gamma = \hbar/\tau_q$ [21] due to scattering (Fig. 2-4 (c)). τ_q represents the quantum lifetime which includes all scattering events and is different from the transport lifetime (τ_{tr}). The states in the middle of each Landau level are called extended states, which also contributes to the conductivity. Those at the edges of a Landau level are called localized states, which cannot contribute to the conductivity.

13

At low temperatures with $\hbar\omega_c > kT$, the thermal energy is too small to excite carriers to

any higher Landau levels, and only the carriers near the Fermi level can conduct at low

temperature. The longitudinal resistance would oscillate as the Fermi level is swept over

consecutive Landau levels. In addition, the separation between each Landau level ($\hbar\omega_c$)

needs to be larger than the width (Γ) to observe the oscillations. This can be written as

$\tau_q \omega_c > 1$ or equivalently $\mu_q B > 1$ [52], where $\mu_q = e\tau_q/m^*$ is the quantum mobility.

The physical picture of spin-splitting is depicted in Fig. 2-4 (d). At a small magnetic field,

each Landau level is doubly degenerate with two spin states, so only the even filling

factors are observed. As the magnetic field increases the Zeeman splitting ($g\mu_B B$)

becomes more pronounced and hence the odd filling factors emerge. g is the Landé g-

factor and μ_B is the Bohr magneton.

The origin of integer quantum Hall plateaus in transverse resistance is the presence

of the discrete Landau level. Fig. 2-5 (a) shows the Landau level energy in real space. At

a given carrier density, the Fermi level intersects with some Landau levels. These Landau

levels act like conduction channels with the same resistance for each channel and

contribute to the transverse resistance (Fig. 2-5 (b)). Therefore, the transverse resistance

remains constant as the Fermi level is within a specific Landau levels, and a plateau is

14

(a)   **(b)**
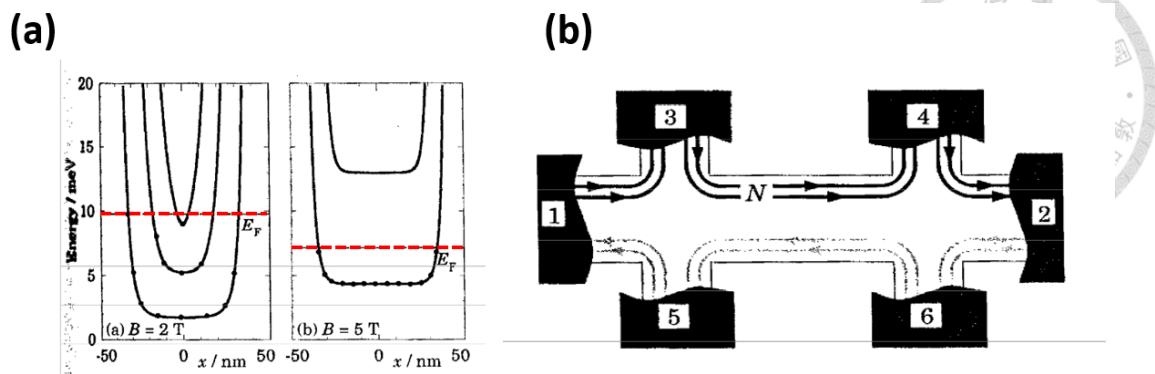
Fig. 2-5 (a) Discrete Landau level distribution in real space and (b) in a Hall bar device [21].

observed. As the magnetic field increases, the spacing between Landau levels increases.

When the Fermi level is swept over a Landau level and intersect with the next one, the

transverse resistance raises to another plateau, so we observe a stair-like pattern. The

relationship between the transverse resistance and filling factor is $R_{xy} = \frac{h}{\nu e^2}$ [21].

2-3   Spin-orbit coupling (SOC) effect

Spin-orbit coupling (SOC) arises from the relative motion between electrons and

nuclei. Under the relativistic effect, the moving electron would view an electric field as

an effective magnetic field by Lorentz transformation (Fig. 2-6) [10]. An electron in the

solid feels a k-dependent magnetic field that interacts with the electron's spin, which is

similar to the Zeeman effect, so the electron's spin and its motion couple together. In

general, the associated Hamiltonian is called the Pauli SO term and given by $-\frac{\hbar}{4m_0^2 c^2}\sigma \cdot$

$p \times (\nabla V_0)$, where σ is the Pauli spin matrix, p is the momentum of the electron, and

V_0 is the atomic potential.

15
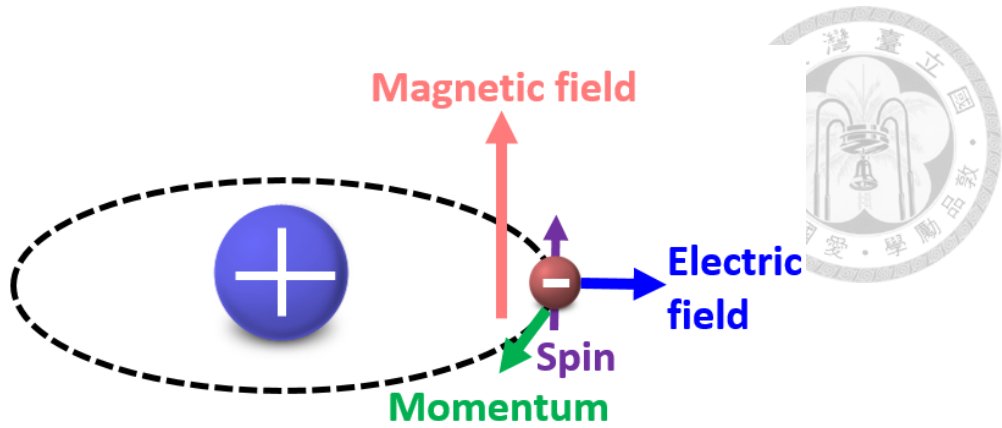
Fig. 2-6 Physical picture of SOC effects.

The valence band splits into heavy hole (HH), light hole (LH), and split-off (SO)

bands [10] when the Pauli SO term is included in the Hamiltonian. Fig. 2-7 (a) shows the

band structure with the isolated electron motion and spin as the SOC effect is ignored.

The orbital quantum number (l) and spin (s) are two individual quantum numbers, and

each band can be expressed by four quantum numbers $|l, m_l, s, m_s\rangle$. Fig. 2-7 (b) shows

the band structure by considering the SOC effects. The electron motion and spin couple,

so we need to use J (defined as $\vec{J} = \vec{L} + \vec{S}$) to describe the total angular momentum. This

results in a further splitting in the valence band. The HH, LH, and SO bands are expressed

in terms of $|j, m_j\rangle = |3/2, \pm 3/2\rangle$, $|3/2, \pm 1/2\rangle$, and $|1/2, \pm 1/2\rangle$, respectively. Δ

denotes the energy difference between the SO and HH bands at $\Gamma = 0$. The term V_0 in

the Pauli SO term represents the atomic potential. For an atom with a larger atomic

number, the potential variation in space is larger (more protons in a nucleus), and hence

the SOC effect is stronger. The value of Δ is expected to be 44 meV for Si, 290 meV for

Ge, and 800 meV for α-Sn. To break the spin-degeneracy, either the time-reversal
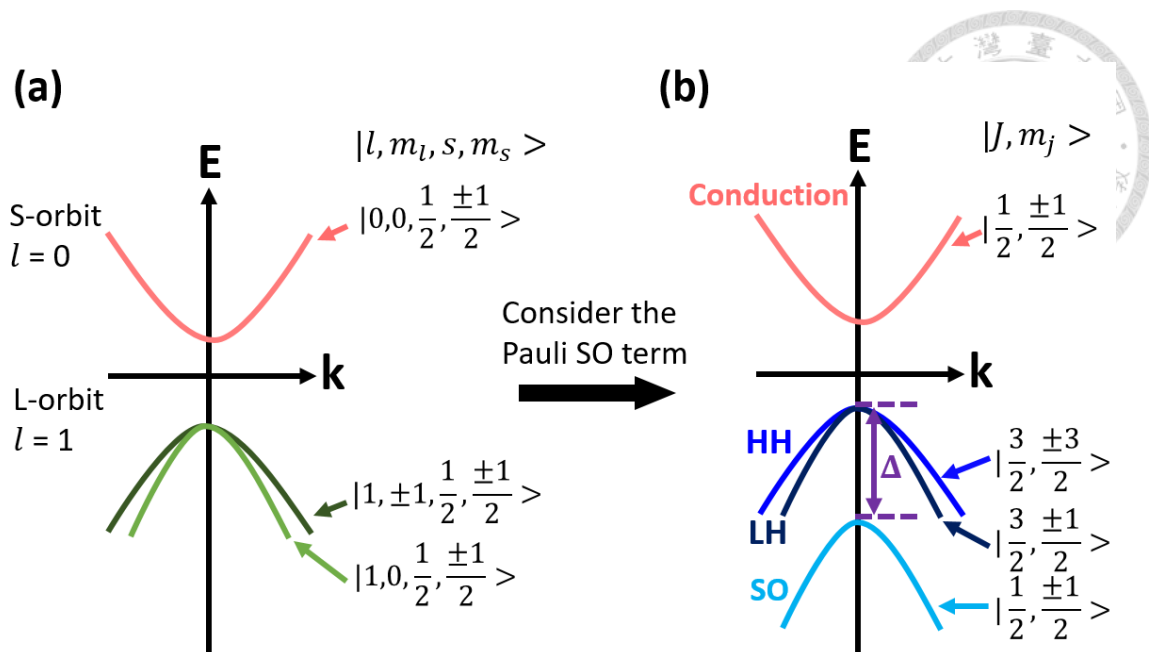
Fig. 2-7 Band structures as the SOC effect is (a) ignored or (b) included [10].

symmetry or the space-reversal symmetry needs to be broken [10]. One example of

breaking the time-reversal symmetry is to apply an external magnetic field. The spin

degeneracy is lifted and this is known as the Zeeman-splitting. On the other hand, there

are two ways to break the space-reversal symmetry: bulk inversion asymmetry (BIA) and

structure inversion asymmetry (SIA). The SOC effect due to the BIA is called the

Dresselhaus SOC [53], while SIA leads to the Rashba SOC effects by an electric field

[54].

The Dresselhaus SOC effect has been observed in III-V materials such as GaAs [55-

57], InAs [58], InGaAs [41] and GaN [38]. The Zinc-Blende structure in III-V materials

lacks of an inversion symmetric point in the crystal structure. This crystal asymmetry acts

like a built-in electric field (Fig. 2-8), which cannot be eliminated or controlled by

external modulation. On the other hand, the diamond structure of group-IV materials

17
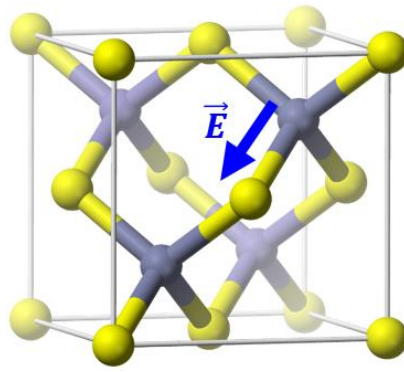
Fig. 2-8 The built-in electric field ($\vec{E}$) in a Zinc-Blend structure [59].

possesses symmetry points. Therefore, no Dresselhaus SOC effect is observed in group-IV materials. In this thesis, we focus on the analysis of SOC effect in GeSn/Ge heterostructures, so the Dresselhaus SOC is not considered.

The Rashba SOC effect can be controlled by external gating through the modulation of the electric fields [54]. Fig. 2-9 shows the band diagram of an undoped Ge/GeSi heterostructure as an example. Under a flat band condition, there is no SIA and the Rashba SOC effect vanishes. Through gating, we can change the extent of SIA and adjust the strength of Rashba SOC. The advantage of the Rashba SOC over the Dresselhaus SOC is the tunability of the SOC strength through gating, which is critical for device applications. In III-V materials, the Dresselhaus and Rashba SOC effects are mixed. There has been much work focused on disentangling their contributions [60] and the interplay between them [61]. On the other hand, group-IV materials only exhibit the Rashba SOC effect due to the absence of BIA [36]. Prior work on Si [31] and Ge quantum wells [14, 36, 37], bulk Ge [62], and GeSn quantum well [16] showed Rashba SOC effects. The Rashba SOC

18
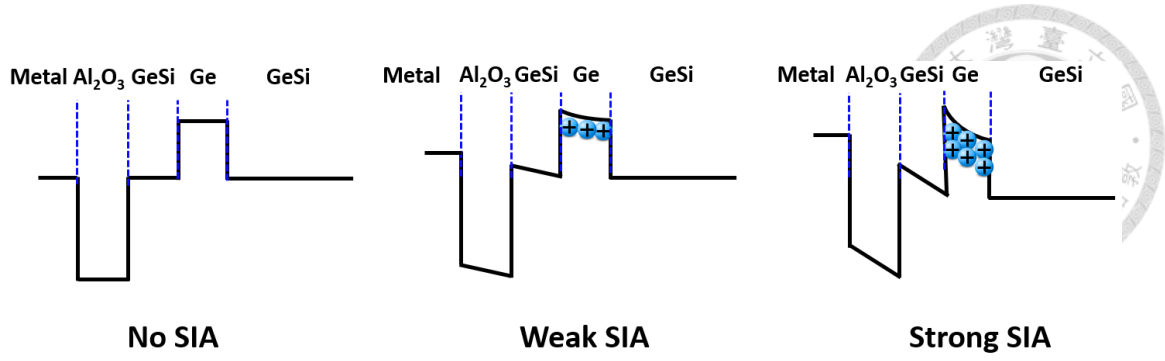
Fig. 2-9 Structure inversion asymmetry induced by gating.

effects in Ge is much stronger than in Si. Our group has demonstrated a ballistic transport

in a Ge/GeSi heterostructure [14], which is a necessary to realize a working spin FET. In

2020, we demonstrated a strongest Rashba SOC in GeSn/Ge heterostructures [16].

We now investigate the Rashba SOC Hamiltonian in the valence band. The

Hamiltonian of the LH band is linearly dependent on k and written as $H_{so}^{LH} = \alpha_1 E_z i(k_- \sigma_+ - k_+ \sigma_-)$, while for the HH band, it is k-cubic dependent given by $H_{so}^{HH} = \alpha_3 E_z i(k_-^3 \sigma_+ - k_+^3 \sigma_-)$ [36]. $\alpha_{3(1)}$ represent the k-cubic (linear) Rashba coefficient and

E_z represents the average electric field along the z-direction. $k_\pm = k_x \pm i k_y$ are the

combination of two $k_\parallel$ components, and $\sigma_\pm = (\sigma_x \pm \sigma_y)/2$ are the combinations of

Pauli spin matrices. The resulting effective magnetic field has different orientations in the

$k_\parallel$ plane for the LH and HH bands (Fig. 2-10) [63]. For the LH band, the SOC-induced

magnetic field is given by $\overrightarrow{B_{LH}}(k_\parallel) = |B_{LH}|(\pm \sin\theta, \mp \cos\theta)$ while for the HH band, it

is $\overrightarrow{B_{HH}}(k_\parallel) = |B_{HH}|(\pm \sin 3\theta, \mp \cos 3\theta)$. θ is the angle between the wavevector

$\overrightarrow{k_{//}} = (k_x, k_y)$ and the k_x axis. For a given k-state, the directions of effective magnetic

fields are different for the HH and LH bands.

19
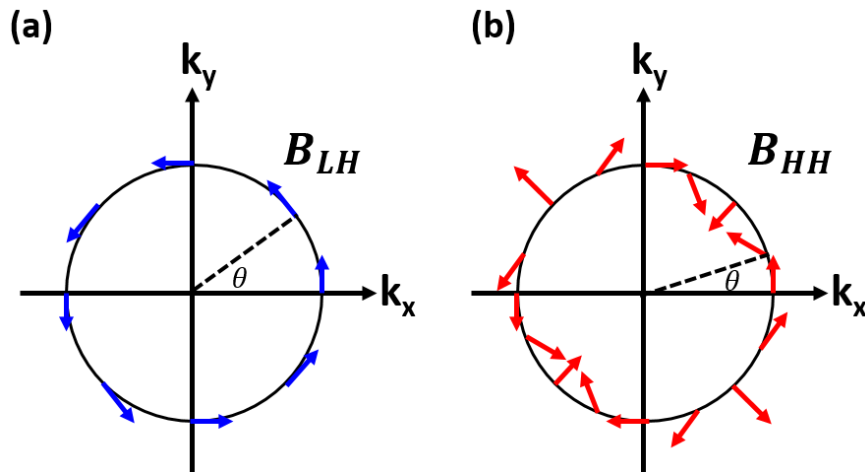
Fig. 2-10 The effective magnetic field orientations in k-space for (a) the LH band and (b) the HH band.

Finally, the spin-splitting energy due to SOC for the LH band has a k-linear dependence ($E_{LH} = \pm\alpha_1 E_z k$) and a k-cubic dependence for the HH band ($E_{HH} = \pm\alpha_3 E_z k^3$) [10]. The splitting energy is proportional to k and E_z because the SOC effect arises from the Lorentz transformation of an electric field for a moving carrier, and hence it depends on the electric field (E_z) and the carrier's momentum ($\vec{k}$). This also shows the tunability of the Rashba SOC strength by changing the electric field (as well as SIA) and the carrier density via gating.

2-4 Characteristic times of carriers in two-dimensional carrier systems

In this section, we introduce various characteristic times: transport lifetime (τ_{tr}), phase-coherence time (τ_ϕ), spin-relaxation time (τ_{so}), and spin-precession time (τ_{pre}). All of them are important parameters for the weak-localization and weak-anti localization effect, which have been used to identify the Rashba SOC effects (section 2-5). (i) The transport lifetime is an average time between two consecutive scattering events (Fig. 2-11 (a)). The corresponding characteristic length is the mean free path defined as $L_{tr} = \tau_{tr} \times V_F$. (ii) The phase-coherence time (τ_ϕ) represents the time scale of carriers in phase with its corresponding length ($L_\phi = \sqrt{D\tau_\phi}$), where D is the diffusion coefficient. Fig. 2-11 (b) shows the physical picture of the phase-coherence time. For a carrier moving clockwise (green path) or counter-clockwise (blue path), the associated wave is originally in-phase during a time scale of τ_ϕ, resulting in a constructive interference pattern (red line). However, beyond this duration, the phase difference gradually accumulates and the carriers become out-of-phase, so the interference pattern fades away as well. The carriers cannot maintain in-phase for infinitely long due to the inelastic scattering events [52]. Qualitatively, the wavefunction of a propagating electron can be expressed as

$$\psi(\vec{r}, t) = A(\vec{r}, t) exp\left[i(\vec{k} \cdot \vec{r} - Et/\hbar)\right]$$
<div align="right">Eq. 2-1</div>

21

(a)

Transport lifetime (τ_{trans})

(b)

Phase-coherence time (τ_ϕ)
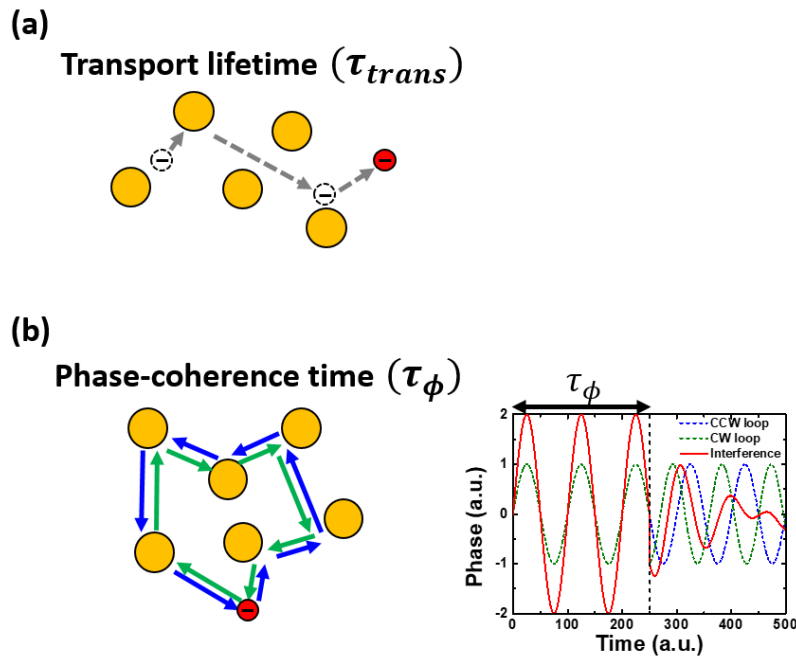
Fig. 2-11 Physical picture of (a) transport lifetime and (b) phase-coherence time.

The phase is proportional to the term $(\vec{k} \cdot \vec{r} - Et/\hbar)$. The phase of the electron wave

accumulates as the electron moves through the spatial term $(\vec{k} \cdot \vec{r})$ and temporal term

$(Et/\hbar)$. For electrons moving clockwise and counter-clockwise, the phase accumulation

of spatial part is the same: $\int_a^b \vec{k} \cdot \vec{r} \, (clockwise) = \int_a^b (-\vec{k}) \cdot$

$(-\vec{r}) \, (counterclockwise)$ since both the direction of $\vec{k}$ and the integral path have

opposite direction. If only elastic scattering events occur when the electron moves along

the paths, the energy of the electron remains constant and the phase accumulation of

temporal term is also the same. Hence, the carriers for different paths remain in phase.

However, inelastic scattering events change the electron's energy via scattering, so the

phase temporal term $(Et/\hbar)$ would not be conserved and finally the carriers become out-

of-phase. A single inelastic scattering may not be strong enough to cause de-phasing, so

the carriers can remain in-phase during a finite period. In semiconductors, there are two

major inelastic scattering sources: electron-phonon scattering and electron-electron

scattering [52]. Detailed discussion will be given in section 4-5.

(iii) The spin-relaxation time (τ_{so}) represents the time scale of carriers holding the

same spin orientations with a corresponding spin-relaxation length ($L_{so} = \sqrt{D\tau_{so}}$). For

a semiconductor lack of inversion symmetry (BIA or SIA), the SOC-induced effective

magnetic field can randomize the spin-orientations. This is called D'yakonov-Perel (DP)

spin-relaxation mechanism [64] and illustrated in Fig. 2-12 (a) (left). Due to the SOC

effect, the carriers feel a k-dependent effective magnetic field and the direction of

magnetic field changes with the momentum. The spin orientation changes between two

collision events and finally randomized. If the collisions happen too frequently, the time

interval between two collisions is too short for a spin to follow the fast changing magnetic

field. Thus, the DP spin-relaxation rate is inversely proportional to the scattering rate.

Besides DP mechanism, there is another mechanism called Elliott-Yafet mechanism [65,

66] to interpret the spin-relaxation in metals and semiconductors with inversion symmetry.

The physical picture of EY mechanism is shown in the right of Fig. 2-12 (b). The EY

mechanism states that when the carriers collide with impurities, there is a probability to

flip over the spin state [67]. Therefore, the more collision events, the higher chance to
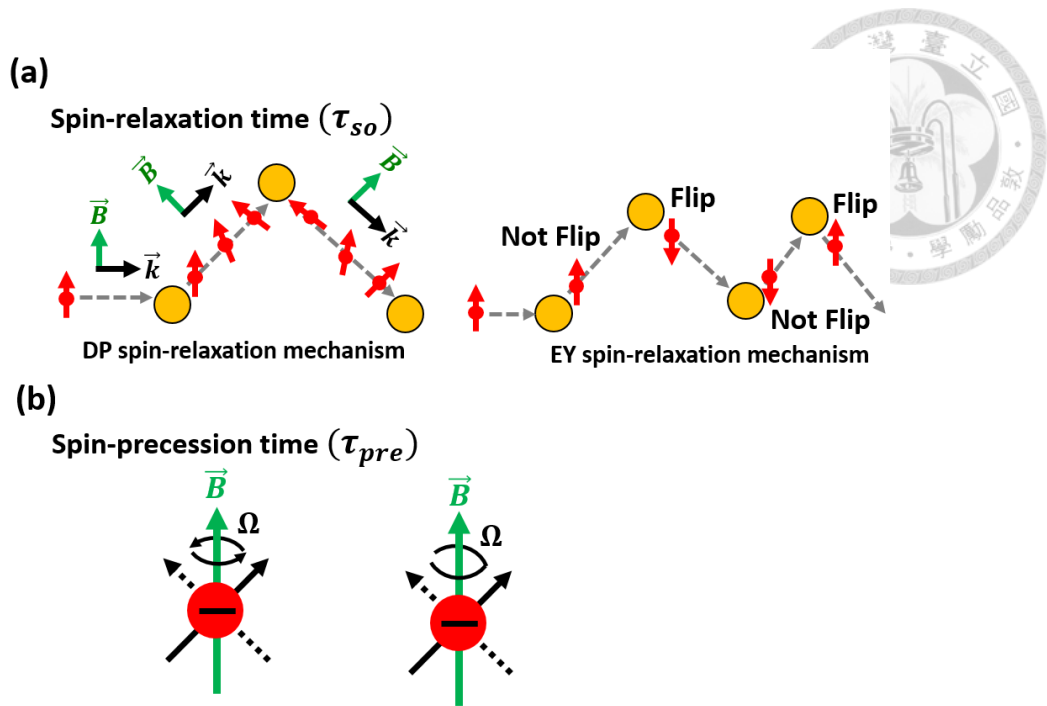
Fig. 2-12 Physical picture of (a) spin-relaxation mechanism and (b) spin-precession mechanism.

observe a different spin states. The spin-relaxation rate for the EY effect is proportional

to the scattering rate, which is the major difference from the DP mechanism. Finally, (iv)

The spin-precession time (τ_{pre}) describes the time scale for a spin to complete a full

precession under a magnetic field (i.e Larmor precession), and the corresponding length

$L_{pre} = V_F \times \tau_{pre}$ is the travelling distance within τ_{pre}. All those characteristic times

and their corresponding characteristic lengths are important parameters for the analysis

of WL/WAL patterns and Rashba SOC effect.

2-5 Weak localization and weak-anti localization
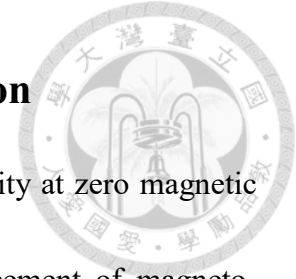
Weak localization (WL) effect reduces the magneto-conductivity at zero magnetic field and weak-anti localization (WAL) effect leads to an enhancement of magneto-conductivity. Both of them represent the interference effects of a carrier traveling a closed loop clockwise and counter-clockwise [68]. Those two paths possess time reversal symmetry as the trajectory is exactly the same and the moving direction is opposite. The perimeter of the loop is defined as L_{loop}. For large loops, as long as their perimeters are longer than the phase-coherence length ($L_{loop} > L_\phi$), the carrier wavefunctions are out-of-phase, so neither WL nor WAL will be observed no matter what the spin-relaxation length is. For the loops whose perimeters are smaller than the phase-coherence length ($L_{loop} < L_\phi$), the carrier wavefunction remains in-phase, so WL or WAL will be observed depending on the length of L_{so}. If the spin direction remains the same ($L_{loop} < L_\phi < L_{so}$ or $L_{loop} < L_{so} < L_\phi$), the constructive interference will occur, leading to a decrease of the magneto-conductivity at $B = 0$, which refers to the WL effect (Fig. 2-13 (a)).

If the spin-relaxation length is so small that the relationship of $L_{so} < L_{loop} < L_\phi$ is satisfied, the spin orientation will alter along the loop (Fig. 2-13 (b)). The constructive interference turns into a destructive one due to a phase difference of π [68]. The physical reason is described as follows. The initial spin state of a carrier is $|\psi\rangle$, and the spin rotation operator is given as [69]:

25

$$\hat{R} = \begin{bmatrix} e^{i(\phi+\gamma)/2}\cos(\theta/2) & ie^{i(\gamma-\phi)/2}\sin(\theta/2) \\ ie^{-i(\gamma-\phi)/2}\sin(\theta/2) & e^{-i(\phi+\gamma)/2}\cos(\theta/2) \end{bmatrix} \qquad \text{Eq. 2-2}$$

For a carrier moving clockwise, the state becomes $|\psi_{CW}\rangle = \hat{R}|\psi\rangle$. For a carrier moving counter-clockwise, its movement is opposite. The direction of the SOC-induced magnetic field is opposite as well since the effective magnetic field is proportional to the cross-product of wavevector ($\vec{k}$) and electric field (E_z). Therefore, the spin rotates in an opposite way, and $|\psi_{CCW}\rangle$ can be written as $|\psi_{CCW}\rangle = \hat{R}^{-1}|\psi\rangle$. The interference term is $\langle\psi_{CW}|\psi_{CCW}\rangle = \langle\psi\hat{R}^{\dagger}|\hat{R}^{-1}\psi\rangle$, and $\hat{R}^{\dagger}\hat{R}^{-1}$ is equal to

$$\hat{R}^{\dagger}\hat{R}^{-1} = \begin{bmatrix} e^{-i(\phi+\gamma)}\cos^2\left(\dfrac{\theta}{2}\right) - \sin^2\left(\dfrac{\theta}{2}\right) & \dfrac{-i}{2}\sin(2\theta)\left[e^{-i\phi} + e^{i\gamma}\right] \\ \dfrac{-i}{2}\sin(2\theta)\left[e^{i\phi} + e^{-i\gamma}\right] & e^{i(\phi+\gamma)}\cos^2\left(\dfrac{\theta}{2}\right) - \sin^2\left(\dfrac{\theta}{2}\right) \end{bmatrix} \qquad \text{Eq. 2-3}$$

We need to consider all loops satisfying $L_{so} < L_{loop} < L_{\phi}$, where carriers can rotate in arbitrary angles. With the integral of $\int_0^{2\pi} \sin^2\left(\dfrac{\theta}{2}\right) d\theta = \pi$, $\hat{R}^{\dagger}\hat{R}^{-1}$ becomes

$$\hat{R}^{\dagger}\hat{R}^{-1} = \begin{bmatrix} -\pi & 0 \\ 0 & -\pi \end{bmatrix} = -\pi\begin{bmatrix} 1 & 0 \\ 0 & 1 \end{bmatrix} \qquad \text{Eq. 2-4}$$
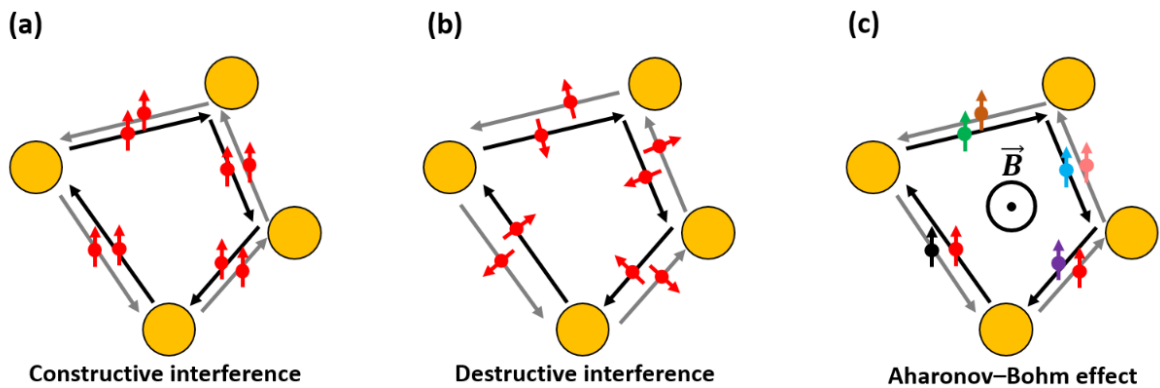
Fig. 2-13 Mechasnism of (a) WL, (b) WAL, and (c) Aharonov–Bohm effect.

and the interference term becomes $\langle\psi\hat{R}^{\dagger}|\hat{R}^{-1}\psi\rangle = -\pi\langle\psi|\psi\rangle$. An additional π-phase shows up, turning the constructive interference ($\because L_{loop} < L_{\phi}$) into destructive interference. Thus, an enhancement in the magneto-conductivity would be observed without applying a magnetic field and this is called WAL effect.

When applying a magnetic field, an additional phase difference will emerge for a carrier travelling clockwise and counter-clockwise due to Aharonov–Bohm (AB) effect (Fig. 2-13 (c)) [69]. We use different colors in Fig. 2-13 (c) to represent the accumulated phase difference induced by the AB effect. This phase difference (AB phase) is proportional to the magnetic flux (Φ_B) of a closed loop given by $2e\Phi_B/\hbar$, so the larger loops acquire more phase difference under the same magnetic field. The AB phase can destroy the in-phase condition and smear out the interference pattern.

The effects of a combination of the WL/WAL patterns on the magneto-resistance are shown in Fig. 2-14. We use "Random" with the gray color to represent the carriers being out-of-phase for larger loops satisfying $L_{loop} > L_{\phi}$. The "Constructive" label with the blue color represents the in-phase carriers for the loops satisfying $L_{loop} < L_{\phi}$. The "Destructive" label with the green color represents the carriers being in-phase and their spin states change if the condition of $L_{so} < L_{loop} < L_{\phi}$ is satisfied. The "AB phase" label with the red color represents the loops that are influenced by a magnetic field. We

27
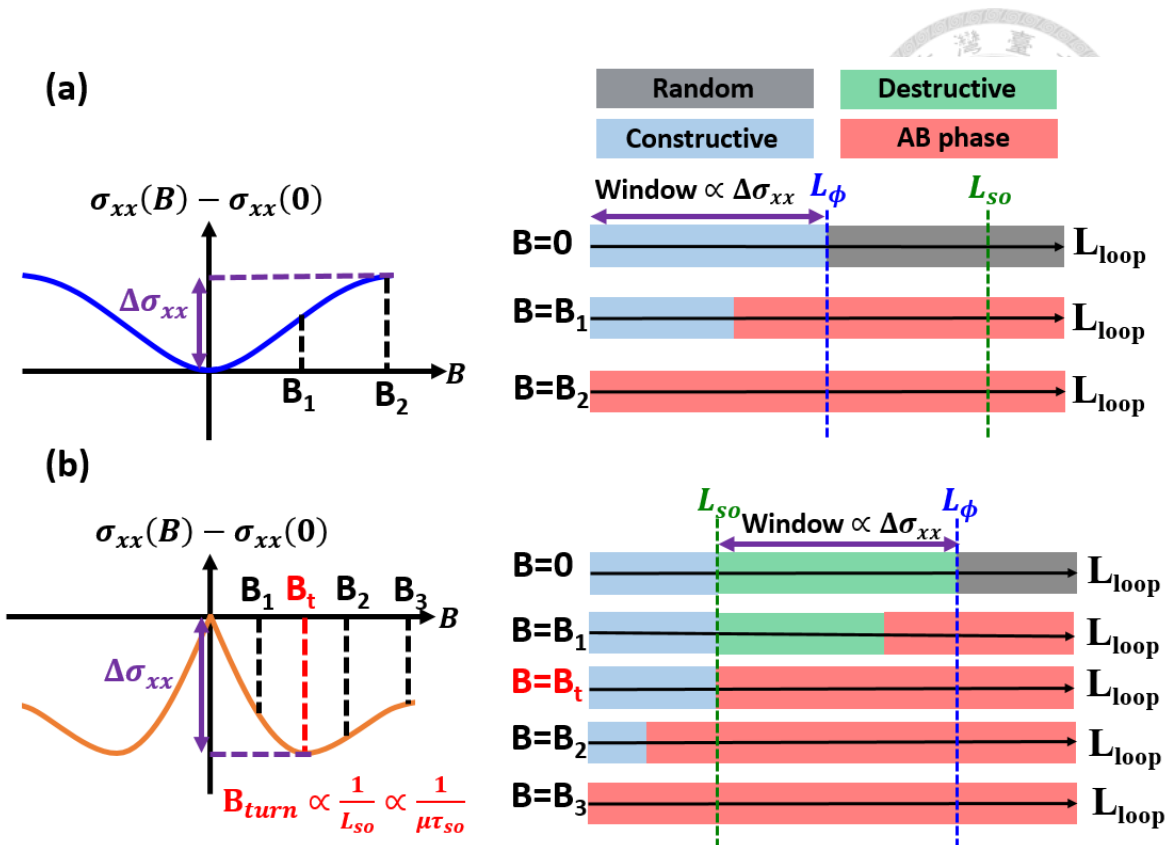
Fig. 2-14 The relationship between L_ϕ, L_{so}, L_{loop} and the magnetic field for (a) WL and (b) WAL

first focus on the WL pattern in Fig. 2-14 (a). A WL pattern occurs as the SOC effect is

weak, and the spin-relaxation length is longer than the phase-coherence length ($L_{so} >$

L_ϕ). For the loops with the perimeters smaller than L_ϕ, they contribute to constructive

interference and the WL effect is observed because the electron is "localized". The WL

pattern is more pronounced (larger $\Delta\sigma_{xx}$ defined in Fig. 2-14 (a)) when more loops

contribute to the constructive interference. Hence, the length "Constructive" label is

proportional to $\Delta\sigma_{xx}$. By applying a magnetic field, those in-phase carriers become out-

of-phase as the AB effect becomes stronger. The constructive interference disappears and

the magneto-conductivity increases because the electron waves are delocalized. Finally,

the magnetic field is so strong that even the smallest loops are affected by the AB effect.

28
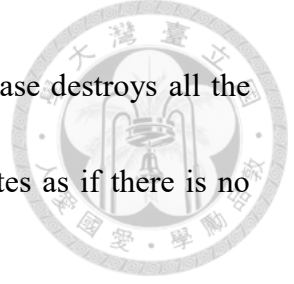
No interference pattern can be observed since the additional AB phase destroys all the constructive interference patterns. The magneto-conductivity saturates as if there is no magnetic effect.

The WAL pattern occurs if the SOC effect is strong enough that the spin-relaxation length is shorter than the phase-coherence length ($L_{so} < L_\phi$). The loops satisfying $L_{so} < L_{loop} < L_\phi$ contribute to destructive interference, leading to the WAL effect. The window range of "Destructive" label is proportional to the WAL signal ($\Delta\sigma_{xx}$ defined in Fig. 2-14 (b)). The dip of WAL pattern is proportional to $\frac{L_\phi}{L_{so}} = \frac{\tau_\phi}{\tau_{so}}$ [70]. The external magnetic field suppresses the WAL feature as well. The carriers have a phase difference of π (Eq. 2-4) due to the changing of spin states, but the additional AB phase changes this value and destroys the destructive interference. When the external small magnetic field is small ($B = B_1 < B_t$), the larger loops have more magnetic fluxes due to their larger enclosed areas and hence acquire more AB phases. On the other hand, the smaller loops are almost not affected by the AB effect. Therefore, the AB phase destroys the destructive interference first, and the magneto-conductivity decreases. At $B = B_t$, all the destructive interferences are washed away by the AB phase, resulting in a dip of the magneto-conductivity. B_{turn} is inversely proportional to L_{so}. For a smaller L_{so}, more small loops contribute to destructive interference and a larger magnetic field is required to gain enough AB phases. At $B = B_2 > B_t$, the AB phase starts to destroy constructive

29

interference and an increase in magneto-conductivity will be observed. Finally, the magneto-conductivity saturates since all interference patterns disappear because of the AB effect.

2-6　Summary

In this chapter, the physical background of SOC and WL/WAL effects are introduced. The SOC effects arise from the relative motion between electrons and nuclei, and there are two types of SOC effects: Dresselhaus and Rashba SOC due to BIA and SIA, respectively. The Rashba SOC strength can be adjusted by external gating, which is of great interest for device applications. Four characteristic times such as lifetime (τ_{tr}), phase-coherence time (τ_{ϕ}), spin-relaxation time (τ_{so}), and spin-precession time (τ_{pre}), and their corresponding lengths are introduced and the dephasing mechanism and spin-relaxation mechanism are also discussed. The relationship between the phase coherence length (L_{ϕ}), spin-relaxation length (L_{so}), and the loop length (L_{loop}) and the resulting interference patterns are described and accounted for the WL and WAL effects. We also described the AB effect and how it suppresses the WL/WAL features.

Chapter 3

Properties of Electro- and Magneto-Transport and Non-Parabolicity Effects on Hole Effective Mass in GeSn/Ge Heterostructures

GeSn is expected to become a direct band gap material when its Sn fraction exceeds $8 \sim 12\%$ [71]. The development of high-quality GeSn epitaxial films has led to high-performance optoelectronic devices such as LEDs [72] , photodetectors [73], and lasers [74]. Besides, the effective mass in GeSn is expected to be lower than that in Ge [75], showing a great potential for electronics application such as metal-oxide-semiconductor field effect transistors (MOSFETs) [76]. However, there is only few work on the quantum transport properties of 2D carriers in the GeSn-based structures [43] and the prior work on the effective mass was limited to the theoretical calculation [77]. Only very recently, the effective mass in a GeSn QW was reported in a modulation-doped (MOD) system [43]. The hole effective mass can be very complicated due to the non-parabolic shape of the valence band. It can be influenced by the quantum confinement [78], strain [79], and carrier density [80]. A linear relationship between the effective mass and carrier density has been reported in a strained Ge QW [81], but not reported in the MOD GeSn QW because of the lack of the density tunability [43]. In this chapter, we demonstrate the first modulation of the carrier density in GeSn 2DHGs on undoped GeSn/Ge heterostructures

with different Sn fractions. We examine their electro-transport properties, magneto-transport properties, and extracting their effective mass. The non-parabolicity effects in the valence band in the GeSn QWs are demonstrated for the first time, too.
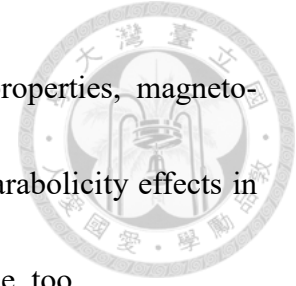
3-1 Material growth and characterization of GeSn/Ge heterostructures and fabrication of Hall bar devices

Undoped GeSn/Sn heterostructures with three Sn fractions of 6%, 9%, and 11% were epitaxially grown by reduced-pressure chemical vapor deposition (RPCVD) on the Si wafers. The epitaxial structure is shown in Fig. 3-1 (a). We used a 200-mm (100) p-Si wafer as a substrate, and a 500-nm relaxed Ge layer, a 10-nm $Ge_{1-x}Sn_x$ QW, and a 23-nm Ge top barrier were deposited subsequently. The details of the epitaxial processes are described as follows. First, before the epitaxial process, we clean the Si substrate with diluted HF (1:50) to remove the native oxides, followed by DI water rinse. The Si wafer was then sent into the RPCVD chamber and baked at 1100 ℃ or 2 minutes. The chamber pressure was controlled at 100 torr. We first deposited a 500-nm Ge layer on top of the Si wafer with Ge_2H_6 as the precursor by using two steps growth to avoid 3D island formation [82]. First, a 5-nm Ge layer was grown at 325 ℃, and another 500-nm Ge layer was grown

32
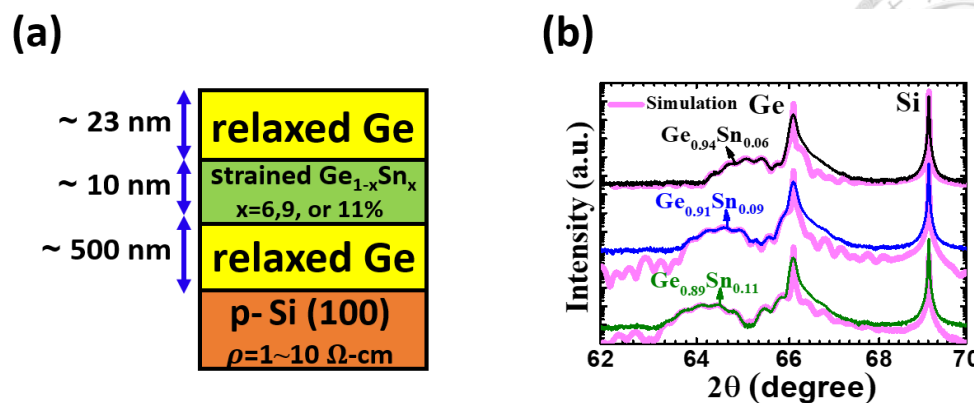
Fig. 3-1 (a) Epitaxial structures of the GeSn/Ge heterostructures with (b) XRD results.

at 375 °C. Subsequently, the wafer was annealed at 800 °C for 10 minutes to decrease

threading dislocations [83]. We then injected Ge_2H_6 and $SnCl_4$ for the growth of the

GeSn/Ge heterostructures at 320 °C to avoid Sn segregation [84] and strain relaxation

[85]. By controlling the ratio of the flow rates of Ge_2H_6 and $SnCl_4$, a 10-nm undoped

strained GeSn layers with three different Sn fractions (6%, 9%, or 11%) were deposited

as a QW layer for the 2DHG formation. Finally, a 23-nm Ge top barrier was grown at 320

°C by Ge_2H_6. The Sn fractions in the GeSn layer were extracted by X-ray diffraction (XRD)

and shown in Fig. 3-1 (b). We used the software of X'pert Epitaxy to analyze the XRD

signals. The derived Sn fractions are very close to the target numbers for each structure.

The Sn fractions and other impurity concentrations were characterized by secondary

ion mass spectroscopy (SIMS) and the results are shown in Fig. 3-2 (a). The Sn fractions

are in agreement with the fitting results of XRD. The concentrations of carbon and oxygen

in the QW is at the order of 10^{18}~10^{20} cm^{-3}, which may contribute to the background

charge scattering. Fig. 3-2 (b) shows a TEM image of an undoped GeSn/Ge

33
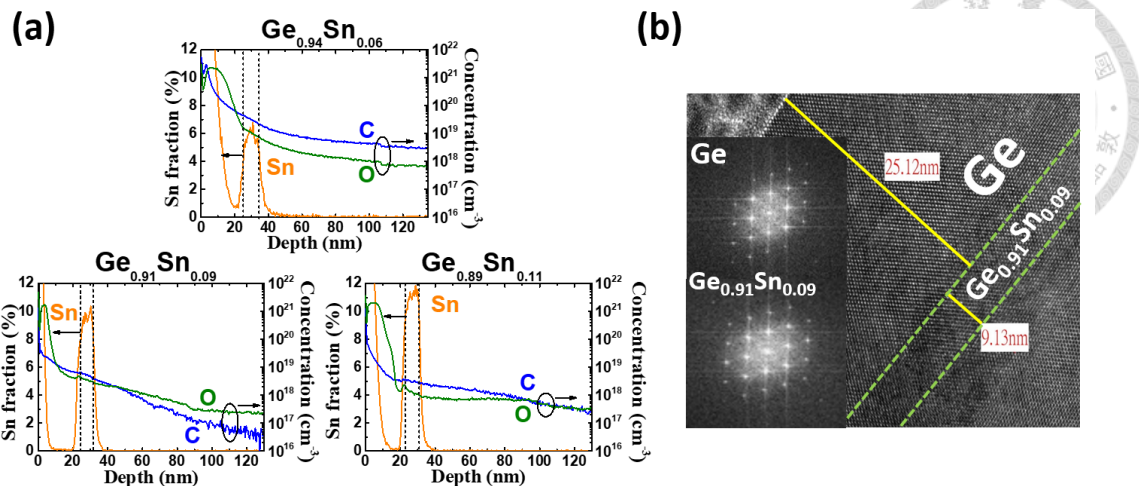
Fig. 3-2 (a) SIMS profiles of the GeSn/Ge heterostructures and (b) TEM image of $Ge_{0.91}Sn_{0.09}$ heterostructures. Inset: diffraction patterns of Ge and $Ge_{0.91}Sn_{0.09}$.

heterostructure with [Sn] = 9%. No observable defects can be seen. The inset presents the diffraction patterns of $Ge_{0.91}Sn_{0.09}$ and Ge respectively, showing the high-quality of the epitaxial structures. The thickness of each layer is consistent with the XRD analysis.

Fig. 3-3 (a) shows the surface roughness of each heterostructure with the root mean square of surface roughness below 3 nm. To investigate the strain conditions of the heterostructures, we performed the reciprocal space mapping (RSM). The results are shown in Fig. 3-3 (b). The peaks of the $Ge_{1-x}Sn_x$ QWs are vertically aligned with the peaks of the Ge layers, meaning they are fully strained. The strain of Ge_xSn_{1-x} is calculated as -0.57 %, -0.96 %, and -1.24 % for [Sn] = 6 %, 9 %, and 11 %, respectively. The Ge layer is slightly tensile strained to the Si substrate, which is due to the difference of the thermal expansion coefficients between Si and Ge [86].
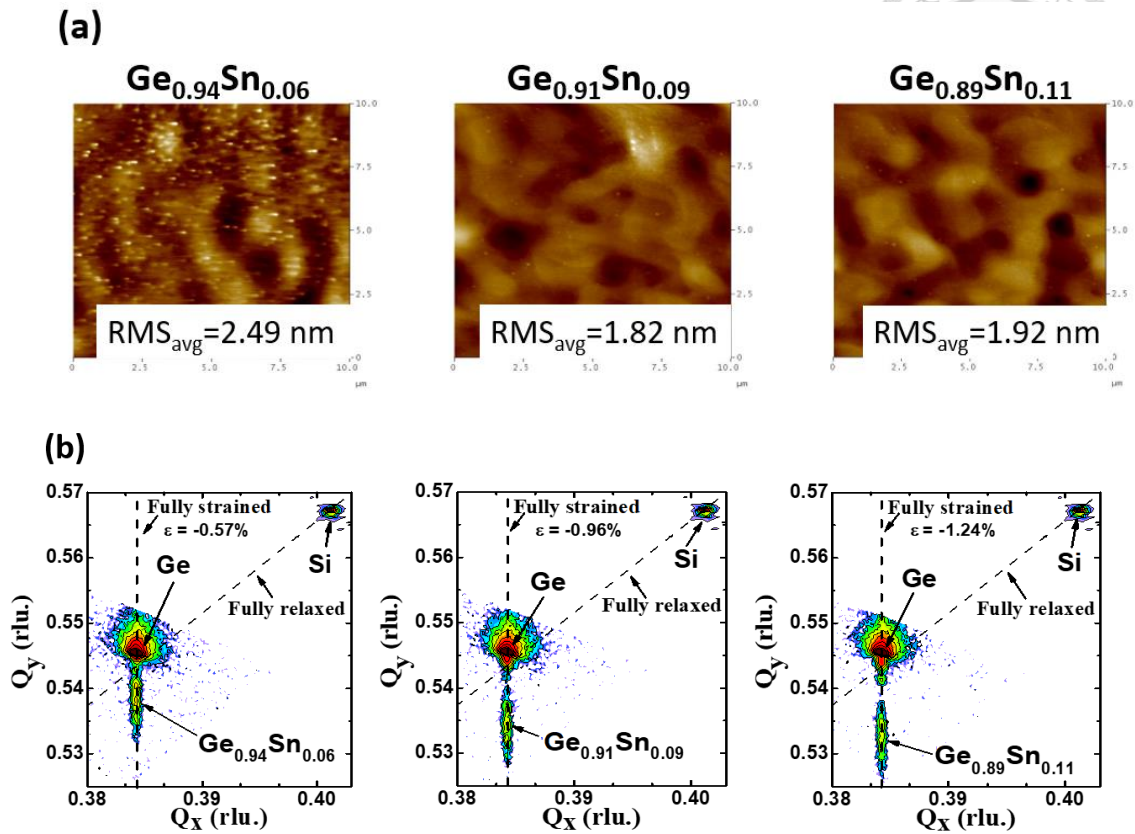
Fig. 3-3 (a) AFM images and (b) RSM contours of the GeSn/Ge heterostructures.

Fig. 3-4 shows the band diagrams of the undoped GeSn/Ge heterostructures with different Sn fractions and the associated wavefunctions simulated by a Scrödinger-Poisson self-consistent solver with the boundary condition of zero electric field in the bulk region. The valence band energy of relaxed Ge is lower than that of strained GeSn, leading to a rectangular GeSn quantum well [45]. The band diagrams of the GeSn/Ge heterostructures were calculated based on the valence band offset reported in Ref. [45] and the relativity dielectric constants in Ref. [87]. As the Sn fraction increases, the band offset becomes larger, resulting in a stronger quantum confinement in the GeSn QW. The wavefunction is more strongly confined in the quantum well with a higher Sn fraction.
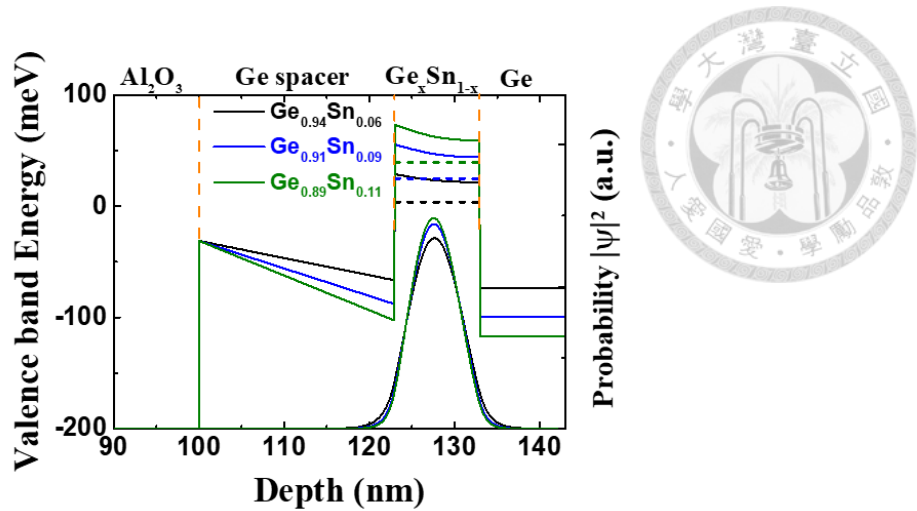
Fig. 3-4 Band diagram and the distribution of wavefunctions of GeSn/Ge heterostructures.

To investigate the 2DHG characteristics, we fabricated gated Hall bar devices. The fabrication process flow is shown in Fig. 3-5 (a). The samples were first cleaned by acetone, methanol, and isopropanol. Then we used photolithography to define the contact patterns and deposited 50-nm Al by e-beam evaporation followed by a lift-off process for Ohmic contacts. A 90-nm Al_2O_3 layer was grown in an ALD chamber at 200 °C. Meanwhile, the Al atoms would diffuse down to the depth of the QW layer to provide carriers. We used 1:6 buffer oxide etchant (BOE) to remove Al_2O_3 to open vias and deposited Ti/Au as a metal gate and contact pads. Finally, photolithographic steps were performed to define the hall-bar patterns. The microscopic picture of a gated Hall bar device is shown in Fig. 3-5 (b). Magneto-transport measurements were performed at T = 1.2 K ~ 4 K by a ^{3}He fridge pumped helium cryostat with a maximum magnetic field of 5 T. The experimental setup is shown in Fig. 3-6. The 10 MΩ resistor is served as a current source
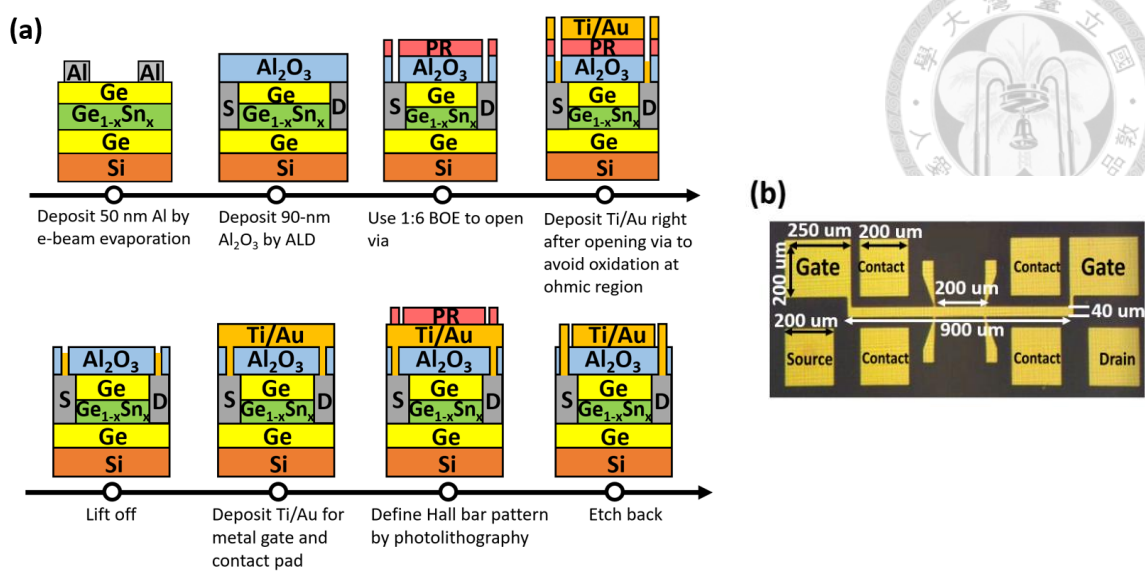
Fig. 3-5 (a) Fabrication process and (b) microscopic picture of a gated Hall bar device.

to convert an 1-V signal into a current of 100 nA. We measured the longitudinal voltage (V_{xx}), transverse voltage (V_{xy}), and the source-to-drain current (I_{DS}) by three lock-in amplifiers. The longitudinal resistivity (ρ_{xx}) was derived by $V_{xx}/I_{DS} \times (W/L)$ and the transverse resistivity (ρ_{xy}) was calculated by V_{xy}/I_{DS}, where L is the length between two measurement contacts and W is the channel width. The carrier density (p_{2D}) was extracted from the slope of ρ_{xy}-B with the relation of $\rho_{xy} = B/(ep_{2D})$, and the mobility μ was derived by $\mu = 1/(ep_{2D}\rho_{xx})$. The longitudinal magneto-conductance was defined as $\sigma_{xx} = \rho_{xx}/(\rho_{xx}^2 + \rho_{xy}^2)$.
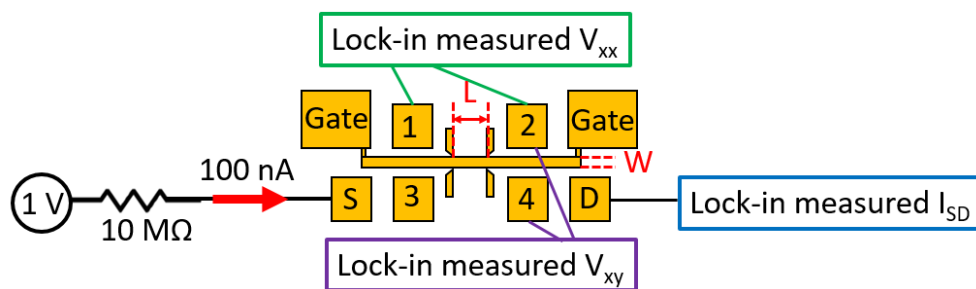
Fig. 3-6 The measurement setup for Hall measurements.

3-2 Properties of electro-transport and magneto-transport in GeSn/Ge heterostructures

Fig. 3-7 (a)~(c) show the I_D-V_G curves of the gated Hall bar devices with different Sn fractions at 4 K under different drain voltages to investigate the transistor characteristics. All the drain currents are saturated at high gate biases, which has been observed for both Si 2DEGs [88] and Ge 2DHGs [42], and can be attributed to the surface tunneling effect [42]. As the gate voltage increases, more holes would be induced in the QW and the electric field becomes stronger. The carriers could tunnel to the Ge/oxide interface and are trapped at the interface states (Fig. 3-7 (d)). The carriers induced by gating are injected from the reservoirs to the buried GeSn QW at the same rate as the tunneling rate to the oxide interface, which leads to the current saturation [89]. Note that all I_D-V_G curves show counter-clockwise hysteresis patterns. This is induced by the trap states between the Ge/oxide interface. When the gate voltage first sweeps from zero to a negative bias, some holes tunnel to the oxide interface and are trapped in the defect states. As the gate voltage is swept back, the trapped holes might not be able to activate, leading to a potential shift in the heterostructure and a shift of the threshold voltages for two different scans. Details of surface tunneling in the 2DEG or 2DHG systems can be referred to Refs. [42, 88-92].
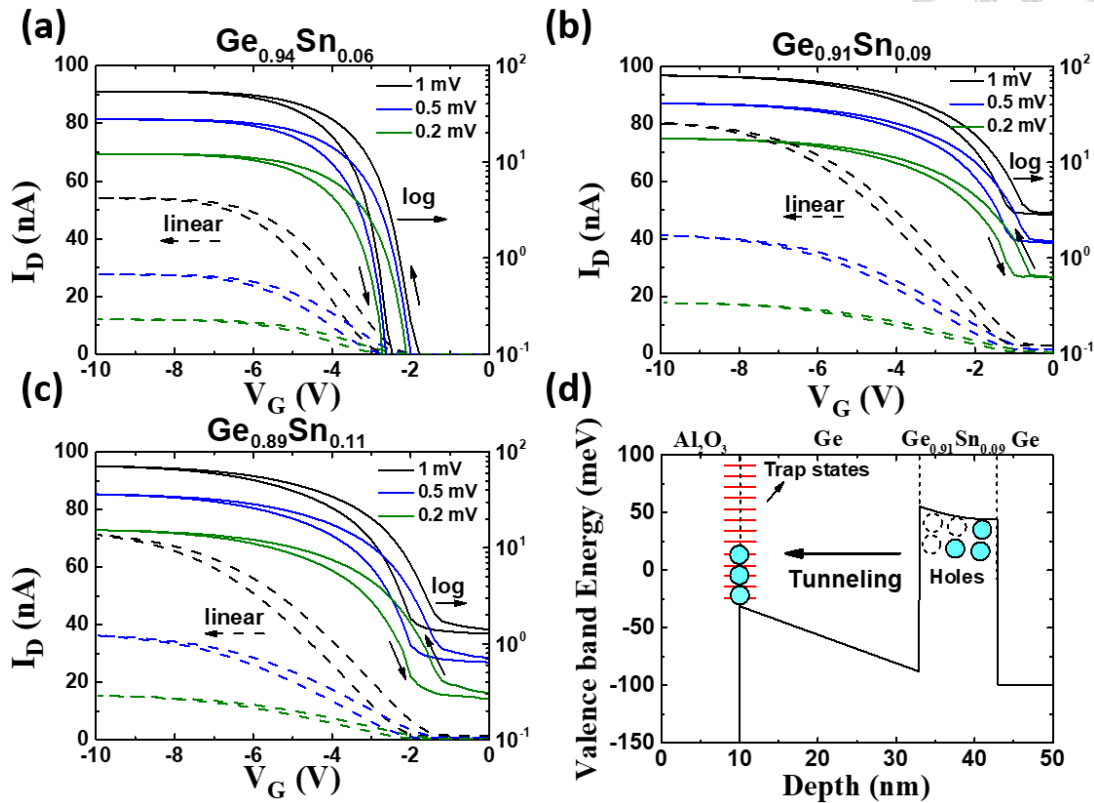
Fig. 3-7 (a)~(c) I_D-V_G curves of the GeSn/Ge gated Hall bar devices at T = 4 K. (d) Schematic of the surface tunneling effect.

Magneto-transport measurements were performed at 1.2 K with standard lock-in techniques. Fig. 3-8 (a) shows the Hall density versus gate voltage. As the gate voltage decreases (more negative), the hole density increases through capacitive coupling with the extracted capacitances of 15.0 nF, 18.3 nF, and 19.3 nF-cm^{-2} for the $Ge_{0.94}Sn_{0.06}$, $Ge_{0.91}Sn_{0.09}$, and $Ge_{0.89}Sn_{0.11}$ devices, respectively. We used a linear extrapolation to extract the effective series capacitance of Al_2O_3 and Ge layers. An unexpected smaller capacitance was obtained compared to the expected series capacitance of the Al_2O_3 and Ge layers ($C_{eff} = \frac{1}{\frac{1}{C_{Ge}} + \frac{1}{C_{Al2O3}}} \sim 50$ nF-cm^{-2}). This could be attributed to the surface tunneling effect since the top Ge layer is so thin, resulting in a small tunneling barrier

39
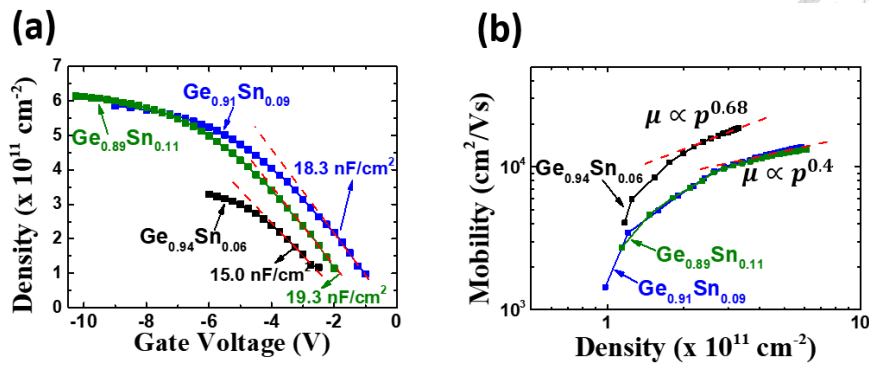
Fig. 3-8 (a) Hall density versus gate voltage of the gated Hall bar devices and (b) Hall density versus mobility at T = 1.2 K.

width and larger tunneling rate. As a result, there exists a carrier loss in the quantum well

and the effective capacitance is reduced [42]. The extracted effective capacitance is larger

in higher Sn device, which is due to the larger band offset, resulting in a smaller tunneling

rate. Moreover, a higher saturation density was observed for the GeSn device with a

higher Sn fraction due to the larger band offset at the GeSn/Ge heterojunction, which has

also been reported for the Si/SiGe heterostructures [91].

A log-log plot of Hall mobility versus density is shown in Fig. 3-8 (b). For all

GeSn/Ge heterostructures, the maximum mobilities are above 10,000 cm^2/Vs. As the

carrier density increases, the mobility is increased due to the screening effects with the

highest mobility of 20,000 cm^2/Vs. On the other hand, the mobility is reduced as the Sn

fraction in the GeSn QW increases possibly due to alloy scattering [93, 94]. The power

law dependence of mobility on carrier density ($\mu \propto p_{2D}^{\alpha}$) reflects the dominant scattering

mechanism. Remote charge scattering can be characterized with $\alpha \sim 1.5$, while

$\alpha \sim 0.5$ refers to background charged impurity scattering. A negative α may be

attributed to interface roughness scattering [48, 95]. At a low density, a strong dependence

between mobility and density ($\mu \propto p_{2D}^{\alpha}, \alpha > 2$) is due to metal-insulator transition (MIT)

at low temperatures [96]. As the density increases, α gradually saturates to roughly 0.4

~ 0.7, which could be attributed to the background impurity scattering [95].

Fig. 3-9 shows the longitudinal and transverse magnetoresistance of $Ge_{0.94}Sn_{0.06}$,

$Ge_{0.91}Sn_{0.09}$, and $Ge_{0.89}Sn_{0.11}$ devices with the integer numbers representing the filling

factors at $T = 1.2$ K. Clear Shubnikov-de Haas (SdH) oscillations and integer quantum

Hall plateaus were observed. As the magnetic field increases to ~ 2.7 T, the Zeeman

splitting emerges at an odd filling factor of 5 in the $Ge_{0.94}Sn_{0.06}$ device. More analysis of

SdH oscillations for the extraction of hole effective mass will be given in following

sections.
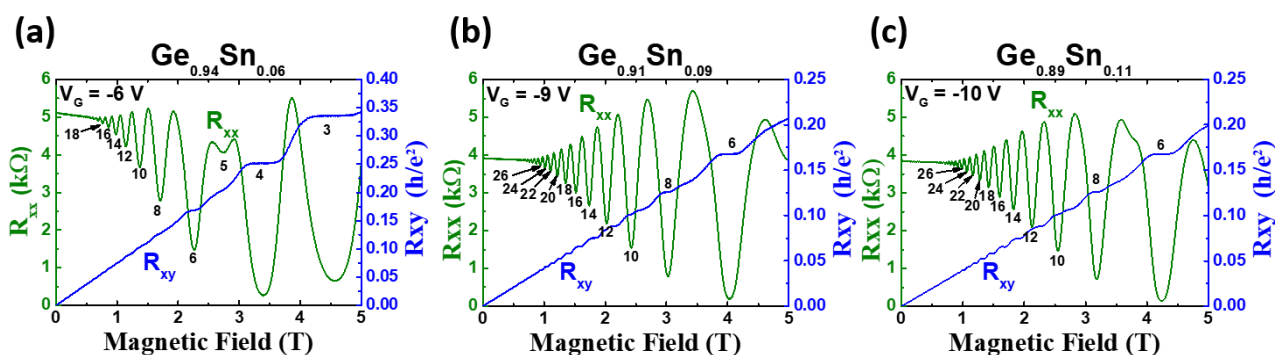
Fig. 3-9 R_{xx} and R_{xy} of the $Ge_{0.94}Sn_{0.06}$, $Ge_{0.91}Sn_{0.09}$, and $Ge_{0.89}Sn_{0.11}$ devices at $T = 1.2$ K. The integer numbers represent the filling factors of Landau levels.
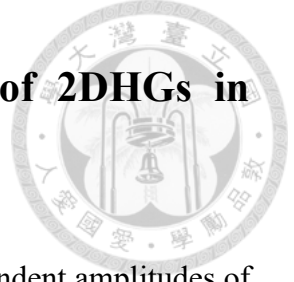
3-3 Non-parabolicity effect on effective mass of 2DHGs in GeSn/Ge heterostructures

To extract the hole effective mass, we use the temperature-dependent amplitudes of SdH oscillations [97]. Fig. 3-10 shows the SdH oscillations at various temperatures (10, 8, 6, 4, 3, 2, 1.6, and 1.2 K) with the integers indicating the corresponding filling factors for all GeSn/Ge heterostructures. When extracting the effective mass, we only focus on the five lowest temperatures (T = 4, 3, 2, 1.6, and 1.2 K), where the thermal energy is much smaller than the energy of a cyclotron gap. We employ the relationship [97]

$$\rho_{xx}(B) = \rho_{xx}(0)\left[1 + 4\frac{\chi}{sinh(\chi)}exp\left(\frac{-\pi}{\omega_c\tau_q}\right)cos\left(\frac{2\pi E_F}{\hbar\omega_c} - \pi\right)\right] + \rho_{quadratic} \qquad \text{Eq. 3-1}$$

$$\chi = \frac{2\pi^2 k_B T}{\hbar\omega_c} = \frac{2\pi^2 k_B T m^*}{\hbar eB} \qquad \text{Eq. 3-2}$$

to derive the effective mass (m^*) and quantum lifetime (τ_q). The $\rho_{quadratic}$ term originates from the carrier-carrier interaction [98]. Fig. 3-11 (a) shows the magneto-resistivity of the $Ge_{0.89}Sn_{0.11}$ device measured at T = 1.2 K ~ 4 K up to a magnetic field
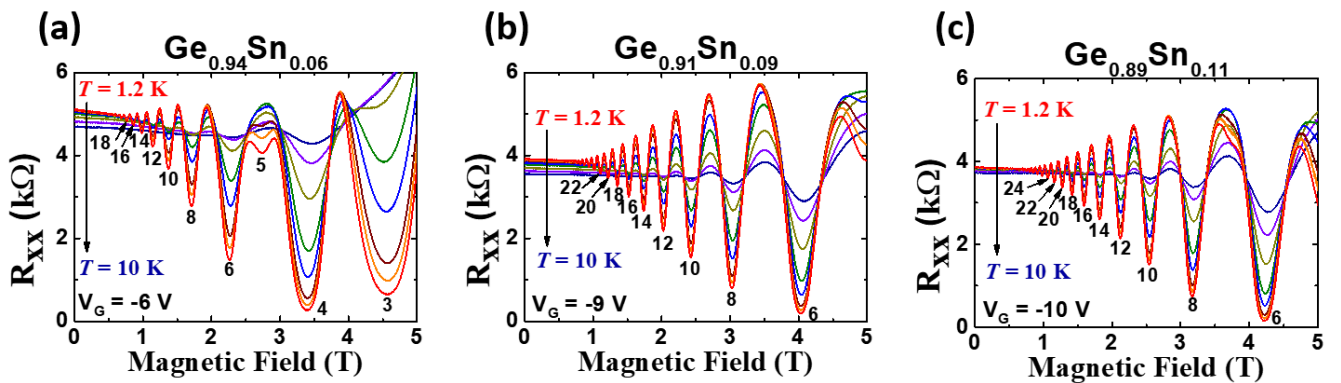
Fig. 3-10 SdH oscillations at different temperatures for the GeSn/Ge heterostructures.
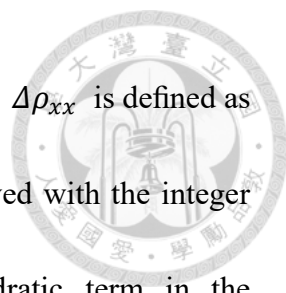
of 5 T with a carrier density (p_{2D}) of 6.1×10^{11} cm^{-2} ($V_G = -10$ V). $\Delta\rho_{xx}$ is defined as $\rho_{xx}(B) - \rho_{xx}(0)$. Shubnikov-de Haas (SdH) oscillations are observed with the integer numbers indicating the corresponding filling factors. The quadratic term in the longitudinal resistivity ($\rho_{quadratic}$) was removed by a moving average filter method [33]. For a given function *f(x)* and a given filter window (Δx), the moving average filter is used to calculate the value at point x_0 by using the following relation:
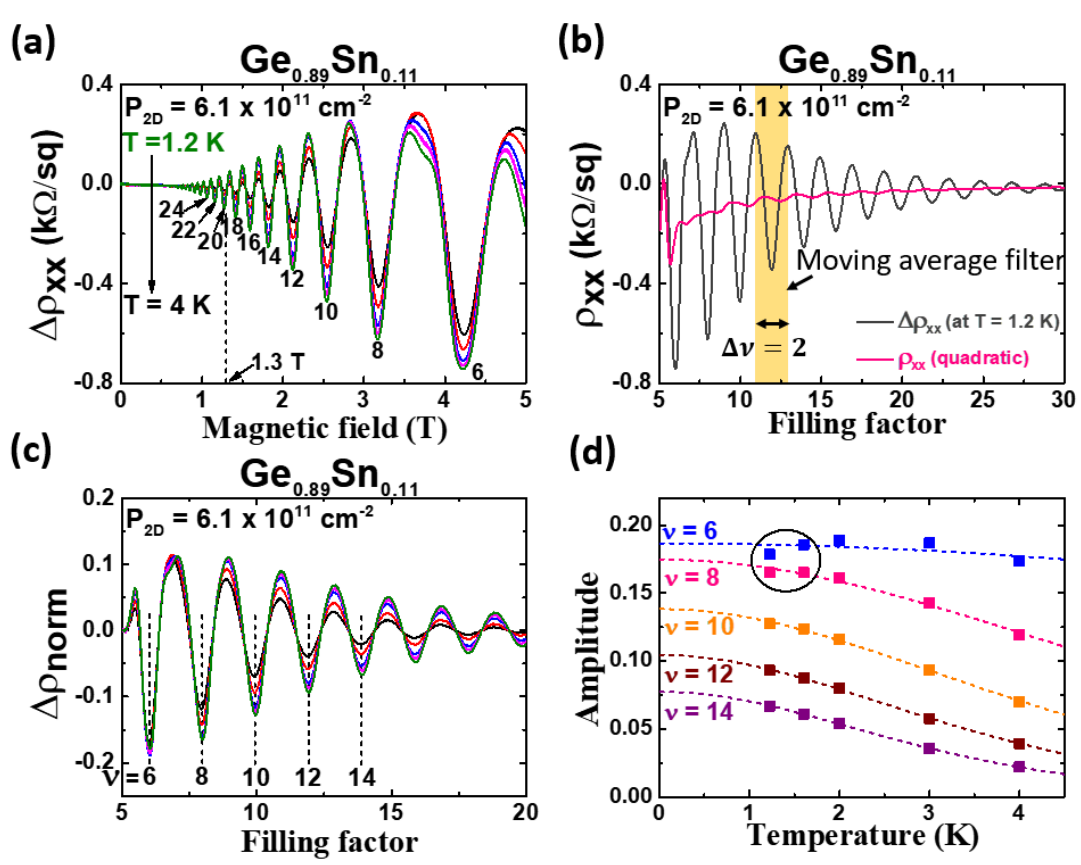
Fig. 3-11 (a) Magneto-resistivity up of the Ge$_{0.89}$Sn$_{0.11}$ device at *T* = 4, 3, 2, 1.6, and 1.2 K. The integer numbers represent the Landau levels. $\Delta\rho_{xx}$ is defined as $\rho_{xx}(B) - \rho_{xx}(0)$. (b) Magneto-resistivity versus filling factor with the gray curve representing $\Delta\rho_{xx}$ taken at *T* = 1.2 K and the pink curve representing $\rho_{quadratic}$ derived by a moving average method. (c) Magneto-resistivity after removing the $\rho_{quadratic}$ term and divided by $4\rho_{xx}(0)$. (d) Fitting results at filling factors of $\nu =$ 6, 8, 10, 12, and 14.

43
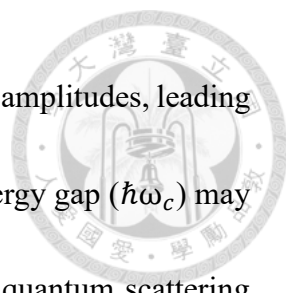
$$\bar{f}(x_0) = \frac{\int_{x_0 - \frac{\Delta x}{2}}^{x_0 + \frac{\Delta x}{2}} f(x)dx}{\Delta x} \qquad \text{Eq. 3-3}$$

We transformed a magnetic field into a filling factor by $\frac{eB}{h} \times \nu = p_{2D}$, and set the filter

window as $\Delta \nu = 2$ (a complete SdH oscillation period). Therefore, the $\rho_{quadratic}$ at

given ν_0 can be expressed as:

$$\rho_{quadratic}(\nu_0) = \frac{\int_{\nu_0 - 1}^{\nu_0 + 1} \rho_{xx}(\nu)\, d\nu}{2} \qquad \text{Eq. 3-4}$$

The gray curve in Fig. 3-11 (b) shows $\Delta \rho_{xx}$ at $T = 1.2$ K versus the filling factor

and the pink curve is the $\rho_{quadratic}$ term. Fig. 3-11 (c) shows $\Delta \rho_{xx}$ after removing the

quadratic term and normalized by $4\rho_{xx}(0)$ (Eq. 3-1). We can use the amplitude of

$\frac{\chi}{sinh(\chi)} exp\left(\frac{-\pi}{\omega_c \tau_q}\right)$ for each valley to extract m^* and τ_q by fitting them to the measured

data. Filling factors of 6, 8,10, 12, and 14 are labeled and the fitting results are shown in

Fig. 3-11 (d). The SdH amplitude increases as the temperature decreases due to the

smaller thermal agitation [21]. However, at $\nu = 6$ and 8, there is a slight decrease in the

SdH amplitude, which is probably due to the effect of Zeeman-splitting. At a small filling

factor corresponding to a large magnetic field, the Zeeman splitting affects the amplitudes

of the SdH oscillations. The Zeeman effect splits the spin-degenerate Landau levels under

a strong magnetic field and causes the SdH amplitudes smaller than expected (as in Fig.

3-11 (d) for $\nu = 6$ and 8) before the odd filling factor emerges [97]. On the other hand,

at a large filling factor corresponding to a small magnetic field, two non-ideal effects

44

could reduce the amplitudes of the SdH oscillations than the expected amplitudes, leading

to a deviation of the extracted effective mass. First, the cyclotron energy gap ($\hbar\omega_c$) may

be too small compared to the Landau level broadening induced by quantum scattering

events ($\hbar/\tau_q$), resulting in poor-resolved SdH oscillation signals [21]. The criterion for

observing a clear oscillation is $\hbar eB/m^* > \hbar/\tau_q$, which is equivalent to $eB\tau_q/m^* > 1$

[21, 52] or $\mu_q B > 1$, where $\mu_q \equiv e\tau_q/m^*$ is the quantum mobility. For the Ge$_{0.89}$Sn$_{0.11}$

device, the highest quantum mobility is 7,500 cm^2/Vs and the corresponding magnetic

field is 1.3 T (Fig. 3-11 (a)). Therefore, the SdH oscillation signals are very weak for $\nu >$

18, and should be excluded for the following analysis. Besides, the inhomogeneous

broadening effects of Landau levels [97] resulting from the spatial variations of the Fermi

level is stronger at a small magnetic field. Thus, the magnetic field needs to be even larger

to observe clear SdH oscillations. To avoid the above discrepancy, we focus on the

intermediate filling factors for the extraction of the effective mass. Fig. 3-12 (a) shows

the Dingle ratio ($\equiv \tau_{tr}/\tau_q$) versus carrier density for the GeSn/Ge heterostructures at $\nu =$

10. τ_{tr} is the transport lifetime defined as

$$\frac{1}{\tau_{tr}} = \int_0^\pi W(k,k')(1-cos\theta)d\theta \qquad \text{Eq. 3-5}$$

$W(k,k')$ is the scattering probability from an initial k-state to a final k'-state and

$(1-cos\theta)$ is a weighing function to include the effects of different scattering angles.
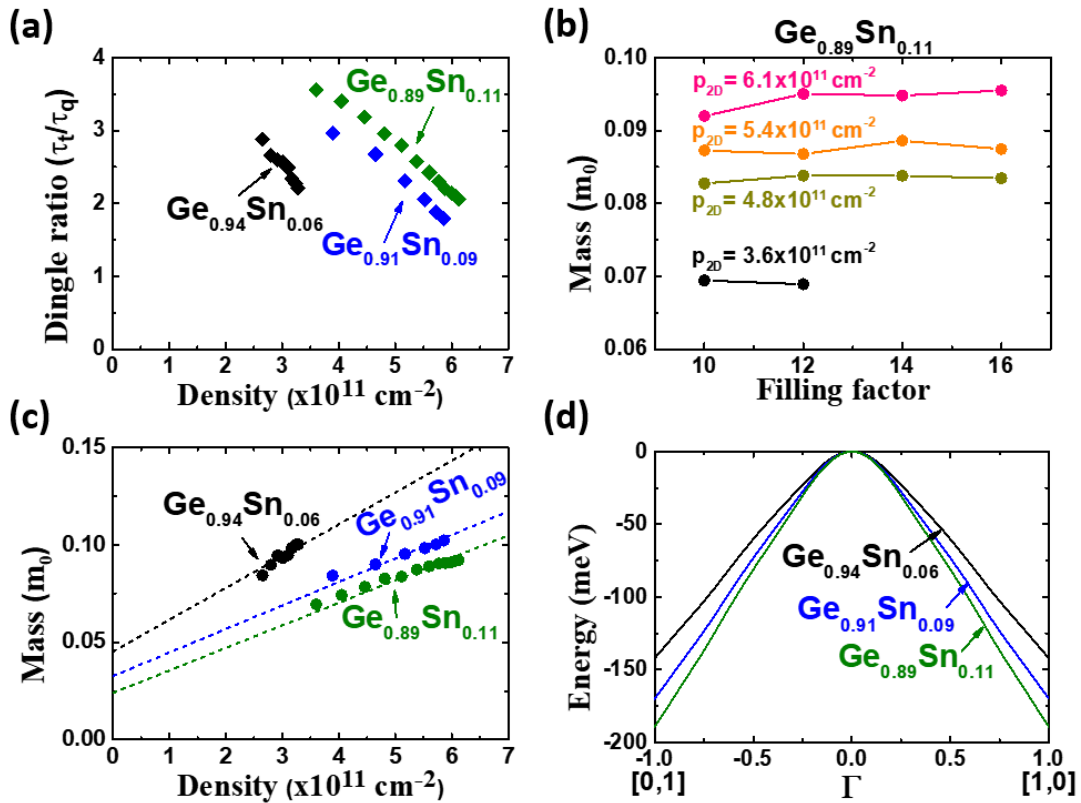
Fig. 3-12 (a) Dingle ratio at $\nu = 10$ versus carrier density for different GeSn/Ge heterostructures. (b) Hole effective mass in the $Ge_{0.89}Sn_{0.11}$ device versus filling factor with different carrier densities. (c) Extracted effective mass versus carrier density at $\nu = 10$. The dashed-lines represent the fitting results by Eq. 3-1 (d) Simulated band structures of GeSn QW's in $k_{\parallel}$ plane. The subband energy at Γ point is shifted to zero for a better view.

From Eq. 3-5, we can see the large-angle scattering events contribute more to the transport scattering rate. On the other hand, the quantum lifetime (τ_q) only depends on the scattering probability.

$$\frac{1}{\tau_q} = \int_0^\pi W(k, k') d\theta \qquad \text{Eq. 3-6}$$

The ratio of τ_{tr}/τ_q is called the Dingle ratio, which is used as an indicator to identify the dominant scattering events (~ 1 for large-angle scattering and $\gg 1$ for small-angle scattering) [99]. From the experiment results, the Dingle ratios is close to one, which suggests that the large-angle scattering events are dominant [100]. This could be

46

attributed to the background charge impurity scattering or alloy scattering [99, 100], which is consistent with the weak density dependence of mobility. The Dingle ratio decreases with increasing carrier density because the scattering rate is $1/\tau_{tr} \propto p_{2D}^{-1.5}$ for remote charged impurity scattering and $1/\tau_{tr} \propto p_{2D}^{-0.5}$ for background charged impurity scattering [95]. The background charged impurity scattering (large-angle scattering) becomes more dominant at high carrier density [101], resulting in a small Dingle ratio.

Fig. 3-12 (b) shows the variations of the effective mass with respect to the filling factor with different carrier densities. The variations are small for the intermediate filling factors. At $v = 10$, we observe a larger effective mass with the carrier density (Fig. 3-12 (c)). The effective mass increases linearly from 0.07 m_0 to 0.1 m_0 as the density increases from 2.7×10^{11} cm^{-2} to 6.1×10^{11} cm^{-2}. This is due to the non-parabolic shape of the valence band in a GeSn QW [81]. The extracted hole mass in Ge$_{0.91}$Sn$_{0.09}$ is close to the reported in Ref. [43] ($m^* = 0.09$ m_0 at 4.1×10^{11} cm^{-2}).

We now investigate the effective mass quantitatively by using a 4-band Lüttinger-Kohn (LK) Hamiltonian [102] with the Bir-Pikus (BP) strain terms [103]. The Hamiltonian is written as [104]

$$\hat{H}_{BP} = - \begin{bmatrix} P+Q & -S & R & 0 \\ -S^\dagger & P-Q & 0 & R \\ R^\dagger & 0 & P-Q & S \\ 0 & R^\dagger & S^\dagger & P+Q \end{bmatrix} \quad \begin{cases} P = P_k + P_\epsilon \\ Q = Q_k + Q_\epsilon \\ R = R_k + R_\epsilon \\ S = S_k + S_\epsilon \end{cases} \quad \text{Eq. 3-7}$$

$P_k, Q_k, R_k,$ and S_k are the Lüttinger-Kohn (LK) term. $P_\epsilon, Q_\epsilon, R_\epsilon,$ and S_ϵ are the Bir-

Pikus (BP) strain term [104]:

$$\begin{cases} P_k = \dfrac{\hbar^2\gamma_1}{2m_0}\left(k_x^2+k_y^2+k_z^2\right) \\ Q_k = \dfrac{\hbar^2\gamma_2}{2m_0}\left(k_x^2+k_y^2-2k_z^2\right) \\ R_k = \dfrac{\hbar^2}{2m_0}\left[-\sqrt{3}\gamma_2\left(k_x^2-k_y^2\right)+i2\sqrt{3}\gamma_3 k_x k_y\right] \\ S_k = \dfrac{\hbar^2\gamma_3}{m_0}\sqrt{3}\left(k_x-ik_y\right)k_z \end{cases} \quad \begin{cases} P_\epsilon = -a_v(\epsilon_{xx}+\epsilon_{yy}+\epsilon_{zz}) \\ Q_\epsilon = \dfrac{-b}{2}(\epsilon_{xx}+\epsilon_{yy}-2\epsilon_{zz}) \\ R_\epsilon = \dfrac{\sqrt{3}b}{2}(\epsilon_{xx}-\epsilon_{yy})-id\epsilon_{xy} \\ S_\epsilon = -d(\epsilon_{xz}-i\epsilon_{yz}) \end{cases}$$

Eq. 3-8

γ_i are the Lüttinger parameters. $a_v, b,$ and d are the deformation potentials. We ignore the coupling from the SO band since the energy difference between the SO and HH bands at the Γ point is relatively large (~ 300 meV [105]). Under a biaxial strain and with a small-k expansion, we can have the energy dispersion relation of the HH band in the following form [104]:

$$\mathrm{E}_{HH} \approx -P_\epsilon - Q_\epsilon - \frac{\hbar^2}{2m_\parallel}k_\parallel^2 - \frac{\hbar^2}{2m_\perp}k_\perp^2 \qquad \text{Eq. 3-9}$$

$m_\parallel$ is the transverse effective mass and defined as $m_0/(\gamma_1+\gamma_2)$. $m_\perp$ denotes the longitudinal effective mass and defined as $m_0/(\gamma_1-2\gamma_2)$. $k_\parallel = k_x^2+k_y^2$. ϵ_{xx} is the strain condition and can be calculated from the RSM data. It is assumed to be equal to ϵ_{yy} while ϵ_{zz} is calculated by $\epsilon_{zz} = \dfrac{-2C_{12}}{C_{11}}\epsilon_{xx}$.

We introduce a non-parabolicity factor (α) into the formula [80] and consider quantized k_z to include the quantum confinement effect. We then have the $E-k$ relation as follows:

48

$$E(1 - \alpha E) \approx -\left(P_\epsilon + Q_\epsilon + \frac{\hbar^2}{2m_\perp} k_{z1}^2\right) - \frac{\hbar^2}{2m_\parallel} k_\parallel^2 \qquad \text{Eq. 3-10}$$

where k_{z1} denotes the wavenumber of the first HH subband. E(k) function can be solved

analytically and the effective mass is calculated by the definition of $m^* = \hbar^2 \left[\frac{d^2 E}{dk^2}\right]^{-1}$.

The E(k) is expressed as:

$$\text{E} = \frac{1}{2\alpha} - \frac{\sqrt{1 + 4\alpha\left[\frac{\hbar^2}{2m_\parallel} k_\parallel^2 + P_\epsilon + Q_\epsilon + \frac{\hbar^2}{2m_\perp} k_{z1}^2\right]}}{2\alpha} \qquad \text{Eq. 3-11}$$

and the second derivative with respect to $k_\parallel$ is

$$\frac{d^2 E}{dk_\parallel^2} = -\frac{\frac{\hbar^2}{m_\parallel}\left[1 + 4\alpha\left(P_\epsilon + Q_\epsilon + \frac{\hbar^2}{2m_\perp} k_{z1}^2\right)\right]}{\left[1 + 4\alpha\left(\frac{\hbar^2}{2m_\parallel} k_\parallel^2 + P_\epsilon + Q_\epsilon + \frac{\hbar^2}{2m_\perp} k_{z1}^2\right)\right]^{3/2}} \qquad \text{Eq. 3-12}$$

By substituting the term of $k_\parallel^2 = k_x^2 + k_y^2 = k_F^2 = 2\pi p_{2D}$ into Eq. 3-12, the effective

mass is

$$m^* = m_\parallel \frac{\left[1 + 4\alpha\left(\frac{\pi\hbar^2}{m_\parallel} p_{2D} + P_\epsilon + Q_\epsilon + \frac{\hbar^2}{2m_\perp} k_{z1}^2\right)\right]^{3/2}}{\left[1 + 4\alpha\left(P_\epsilon + Q_\epsilon + \frac{\hbar^2}{2m_\perp} k_{z1}^2\right)\right]} \qquad \text{Eq. 3-13}$$

For a small k, we can use Taylor expansion $(1 + x)^n \approx 1 + nx$ and the effective mass

becomes

$$m^* = m_\parallel \frac{\left[1 + 6\alpha\left(\frac{\pi\hbar^2}{m_\parallel} p_{2D} + P_\epsilon + Q_\epsilon + E_0\right)\right]}{[1 + 4\alpha(P_\epsilon + Q_\epsilon + E_0)]} \qquad \text{Eq. 3-14}$$

where E_0 is equal to $\frac{\hbar^2 k_\parallel^2}{2m_\parallel}$, which corresponds to the first subband energy. We used Eq.

3-14 with the non-parabolicity factor (α) as a fitting parameter to fit the data. All other

49
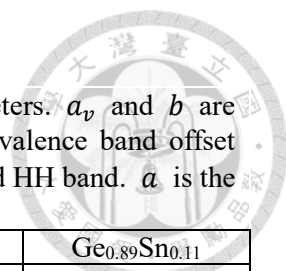
Table 3-1 Material parameters of Ge$_{1-x}$Sn$_x$. γ_i are the Lüttinger parameters. a_v and b are the deformation potentials. C_{ij} are the elastic constants. E_{VBO} is the valence band offset between GeSn/Ge. Δ_{SO} is the energy difference between the SO band and HH band. a is the lattice constant and ϵ_r is the relativity dielectric constant.

	Ge	Ge$_{0.94}$Sn$_{0.06}$	Ge$_{0.91}$Sn$_{0.09}$	Ge$_{0.89}$Sn$_{0.11}$
γ_1 [105]	11.1100	13.2005	14.5298	15.5212
γ_2 [105]	3.2520	4.2789	4.9348	5.4248
γ_3 [105]	4.6890	5.7405	6.4081	6.9058
a_v [eV] [87]	1.240	1.2604	1.2706	1.2774
b [eV] [87]	-2.900	-2.888	-2.882	-2.878
C_{11} [GPa] [87]	128.53	124.96	123.17	121.98
C_{12} [GPa] [87]	48.26	47.12	46.55	46.17
C_{44} [GPa] [87]	68.3	66.37	65.41	64.77
E_{VBO} [eV] [45]	0	95.3	143.6	176.1
Δ_{SO} [eV] [105]	291.0	329.9	348.0	359.6
a [Å] [87]	5.6573	5.7072	5.7322	5.7488
ϵ_r [87]	16.20	16.67	16.90	17.06

parameters are derived by the linear interpolation between Ge and Sn reported in Ref. [87] or using the quadratic expression reported in Ref. [105]. E_0 is calculated by a finite quantum well model with the valence band offset reported in Ref. [45]. All the parameters are listed in Table 3-1.

The fitting results (dash lines) is shown in Fig. 3-12 (c), showing a good agreement with the experiment data. The non-parabolicity factor is 8.0 eV^{-1}, 4.9 eV^{-1}, and 4.0 eV^{-1} for Ge$_{0.94}$Sn$_{0.06}$, Ge$_{0.91}$Sn$_{0.09}$, and Ge$_{0.89}$Sn$_{0.11}$ at $\nu = 10$, respectively. The variation of α is less than 10% when other filling factors are used ($\nu = 6, 8$ for Ge$_{0.94}$Sn$_{0.06}$ and $\nu = 8, 12$ for Ge$_{0.89}$Sn$_{0.11}$ and Ge$_{0.91}$Sn$_{0.09}$). The hole effective mass of GeSn is smaller for a higher Sn fraction, which is due to the larger deformation of the HH band by a stronger compressive strain. To verify this, we used a 6-band $k \cdot p$ method to simulate the band structures of the GeSn QWs by Nextnano software. Fig. 3-12 (d) shows the band structure
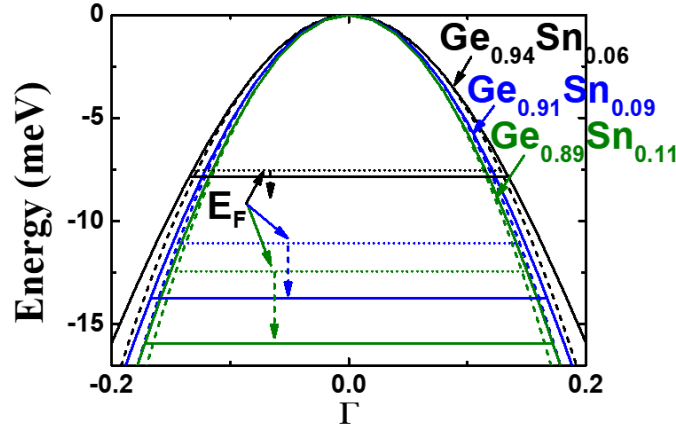
Fig. 3-13 The zoom-in band structure of GeSn QWs. The dashed lines represent perfect parabolas. The horizontal lines represent the Fermi levels corresponding to the initial carrier density (dotted line) and saturated carrier density.

of the first HH subband in $k_{\parallel}$ plane and the subband energy at the Γ point have been shifted to zero for a better view. Clearly, as the Sn fraction increases, the larger strain induces a stronger deformation of the HH band. The larger curvature in band structure results in a smaller effective mass. Fig. 3-13 shows the zoom-in band structure of GeSn QWs with the Fermi levels. The Fermi levels are calculated by $\hbar^2 k_F^2 / 2m^*$, where $k_F = \sqrt{2\pi p_{2D}}$. p_{2D} is derived from the Hall measurement and m^* is derived from the SdH oscillations. The Fermi levels (dotted lines) correspond to the initial carrier density while the solid lines represent the Fermi levels for the case of the saturated carrier density. The perfect parabolic band structures are constructed from five k points that are closet to $k = 0$, which are $(k_x, k_y) = (0.04, 0), (0.02, 0), (0, 0), (0, 0.02),$ and $(0, 0.04)$. We can see the band structures are deviated from the perfect parabolas at the Fermi level, so it is possible the non-parabolicity effect must be considered.

51
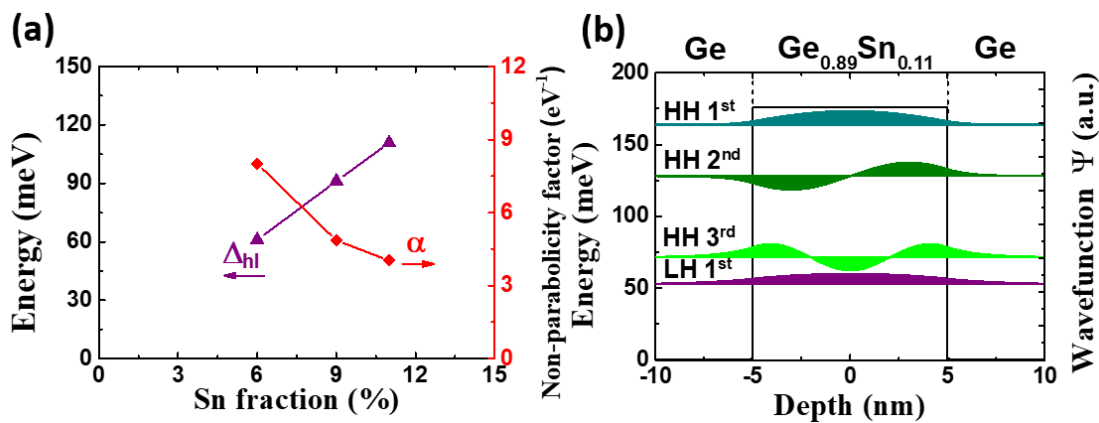
Fig. 3-14 (a) Non-parabolicity factor (α) and HH-LH splitting energy (Δ_{hl}) versus Sn fraction. (b) Simulated band diagram and subband levels with corresponding wavefunctions in a $Ge_{0.89}Sn_{0.11}$ QW.

We now investigate the non-parabolicity effect in the GeSn QW. In Fig. 3-14 (a), the energy difference between HH and LH bands (Δ_{hl}) calculated by Nextnano are plotted with respect to the Sn fraction. α decreases with the Sn fraction and the energy splitting of HH and LH bands increases. The origin of non-parabolicity is the band mixing [106], which is stronger as different bands are closer. The larger compressive strain in GeSn with a higher Sn fraction causes a larger energy splitting between the HH and LH bands, suppressing the band mixing and resulting a smaller non-parabolicity factor. The mixing between different HH subbands is a higher-order effect compared to the mixing between the ground HH subband and the LH subband. Fig. 3-14 (b) shows the band diagram of $Ge_{0.89}Sn_{0.11}$ and the wavefunctions with each subband specified. Compared to the first subband of the LH band, the second and third subbands of the HH band are closer to the first subband of the HH band. However, they cannot contribute to the band mixing since

52
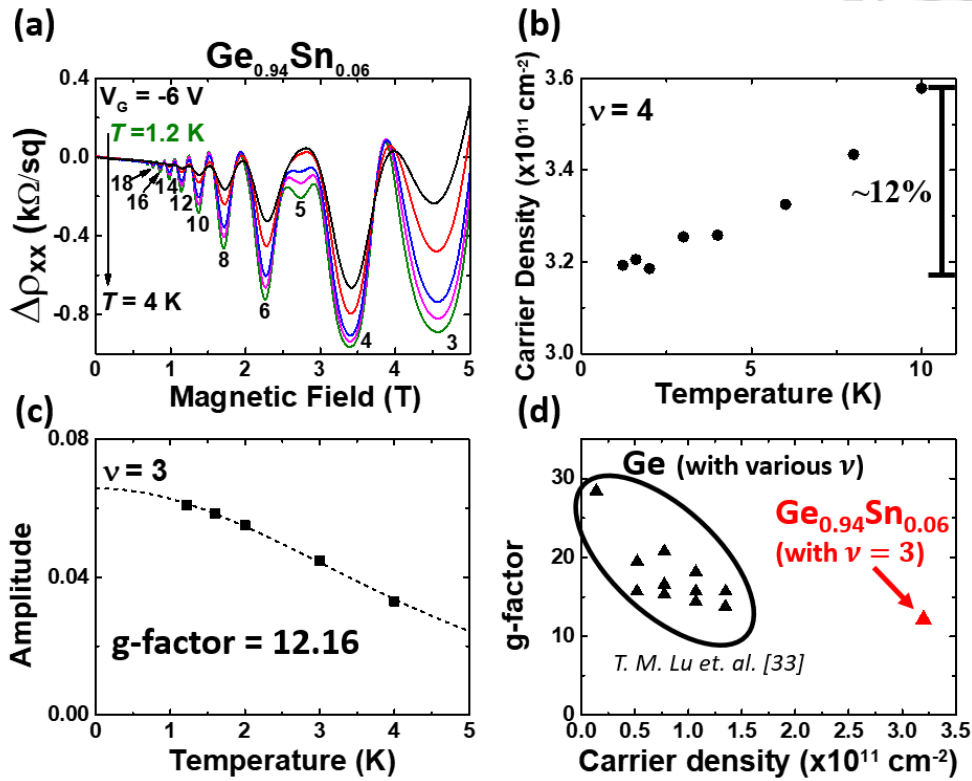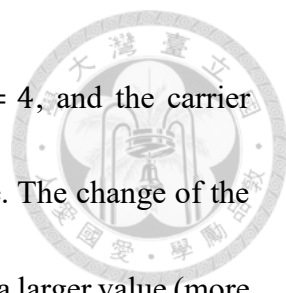
Fig. 3-15 (a) SdH oscillations of $Ge_{0.94}Sn_{0.06}$ at varies temperatures. (b) Carrier density versus temperature at $\nu = 4$. (c) Fitting results at filling factors of $\nu = 3$ and the extracted g-factor is 12.16. (d) Extracted g-factor versus carrier density in Ge QW [33] and $Ge_{0.94}Sn_{0.06}$ QW.

they are orthogonal (i.e. $\langle \Psi_i^{HH} | \hat{H} | \Psi_j^{HH} \rangle = \delta_{ij} E_j$) and the Hamiltonian only contains the non-zero diagonal terms. The coupling between the LH and HH bands can be written as $\langle \Psi_i^{LH} | \hat{H} | \Psi_j^{HH} \rangle = E_j \langle \Psi_i^{LH} | \Psi_j^{HH} \rangle$, where $\langle \Psi_i^{LH} | \Psi_j^{HH} \rangle$ represents the non-zero coupling term. Therefore, the decrease of non-parabolicity factor with the Sn fraction is attributed to the weaker coupling between the HH and LH bands due to the larger compressive strain in GeSn with a higher Sn fraction.

Finally, the odd filling factor ($\nu = 3$) in $Ge_{0.94}Sn_{0.06}$ allows us to extract the g-factor (Fig. 3-15 (a)). The valleys of the SdH oscillations shift when the temperature is reduced at $\nu = 4$, which is due to the changes of the carrier density. Fig. 3-15 (b) shows the carrier

53

density extracted by Hall measurements versus temperature at $\nu = 4$, and the carrier

density variation is 12% between the highest and lowest temperature. The change of the

carrier density can be attributed to the shift of the threshold voltage to a larger value (more

negative) as the temperature is decreased. Hence, at a given gate bias ($V_G = -6$ V), the

carrier density decreases. We use the five lowest temperatures and $\nu = 3$ to extract the

g-factor. The fitting procedures are the same as what we extracted the effective mass by

replacing the denominator of χ in Eq. 3-3 with the Zeeman splitting energy $g\mu_B B$

$\left(\chi = \frac{2\pi^2 k_B T}{g\mu_B B} \right)$ [33]. Fig. 3-15 (c) shows the fitting results and the extracted g-factor is

12.16, which is slightly lower than that in the Ge QW [33] (Fig. 3-15 (d)).

3-4 Summary

In summary, three undoped GeSn/Ge heterostructures with Sn fractions of 6%, 9%,

and 11% were grown by RPCVD and gated Hall bar devices were fabricated for magneto-

transport measurements at cryogenic temperatures. All devices show transistor

characteristics and the highest mobility is 20,000 cm^2/Vs. Clear SdH oscillations and

integer quantum Hall plateaus were observed. We extracted the hole effective mass and

quantum lifetime by the amplitudes of the SdH oscillations at various temperatures. The

low Dingle ratios suggest the large-angle scattering events such as background impurity

scattering are the dominant scattering mechanisms. The extracted effective mass is

smaller in the device with a higher Sn fraction, which is due to the larger compressive

strain and the stronger band deformation. As the carrier density increases, the hole

effective mass increases due to the non-parabolicity effects. The non-parabolicity effect

is weaker as the Sn fraction in the GeSn QW increases due to a larger HH-LH splitting

energy, which results in a weaker band mixing between the HH and LH bands. Finally,

the extracted g-factor in $Ge_{0.94}Sn_{0.06}$ device is 12.16, which is slightly lower than that in

a Ge QW [33].

Chapter 4

Spin-Orbit Coupling in GeSn/Ge Heterostructures

GeSn is a promising material for future spintronics and spin-based quantum computing applications for its strong Rashba spin-orbit coupling (SOC) effect [16] and compatibility to Si VLSI technologies. In this chapter, we analyze the Rashba SOC in the GeSn/Ge heterostructures through analysis of the weak-localization (WL) and weak-anti localization (WAL) patterns. Fig. 4-1 (a) shows a schematic of the valence band structures for compressively-strained GeSn (bulk). The heavy hole (HH) and light hole (LH) bands split with an energy difference Δ_{hl} and deform due to compressive strain [36]. The spin degeneracy of the HH band is broken and two subbands are formed because of the SOC effects (inset of Fig. 4-1 (a)) [10]. The green dashed line in the inset represents the degenerate HH bands with a parabolic E-K dispersion of $E = \hbar^2 k^2 / 2m^*$ in the absence of SOC, where m^* is the effective mass and k is the wavevector. In the presence of SOC effects, the HH band splits into two subbands with energy shifts of $\pm \alpha_3 E_z k^3$ around the degenerate point $k = 0$. At small wavevectors, the cubic splitting is negligibly small. As the wavevector increases, the energy difference becomes larger and follows a cubic law, which was observed experimentally in a compressively strained Ge QW [14, 36]. We also notice that the spin-orientation in the two spin subbands are opposite for $+k$ and $-k$

56
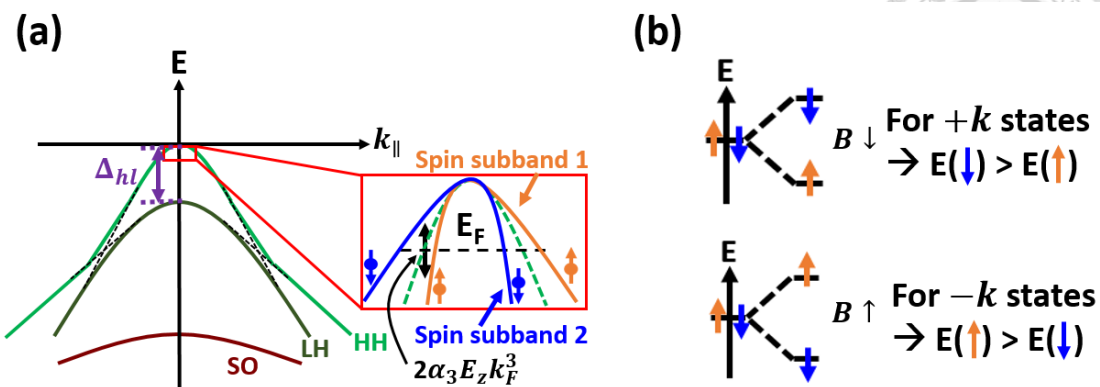
Fig. 4-1 (a) Valence band structure of compressively strained GeSn. Inset : Zoom-in of the HH band structure with (orange and blue) and without (green) SOC effects near $k = 0$ (b) Schematic explanation on the spin-orientation of two HH spin subband.

states [63]. This is because the effective magnetic field is opposite for holes with opposite momentum ($+k$ and $-k$ states). We can assume the effective magnetic field points "downward" for $+k$ states and the energy for spin-down (parallel) is larger than for spin-up (anti-parallel). However, for $-k$ states, the effective magnetic field becomes "upward" and the energy for spin-up (parallel) is larger than that for spin-down (anti-parallel) (Fig. 4-1 (b)). Hence, the spin-orientations are opposite for $+k$ and $-k$ states in the band structure.

By fitting experimental data to the Hikami-Larkin-Nagaoka (HLN) formula, phase-coherence time (τ_ϕ) and spin-relaxation time (τ_{so}) are extracted. We further calculate spin-precession time (τ_{pre}), k-cubic Rashba coefficient (α_3) and spin-splitting energy (Δ_{so}) by a DP spin-relaxation mechanism. We observe an enhancement of the SOC strength in the GeSn devices compared to a pure Ge device as expected. However, we also observed a negative strain effect that would reduce the SOC strength when adding
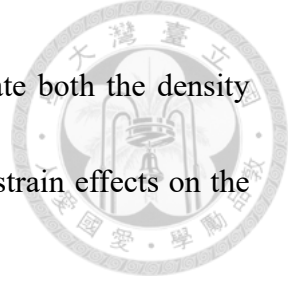
more Sn atoms in the Ge host crystal. In this chapter, we investigate both the density dependence and temperature dependence of WL/WAL features, the strain effects on the strength of Rashba SOC, and the dephasing mechanisms.

4-1 Density dependence of weak localization and weak-anti localization in GeSn/Ge heterostructures

To measure the magneto-conductivity, we fabricated the gated Hall bars (Fig. 3-5), and measured the longitudinal resistivity (ρ_{xx}) and transverse resistivity (ρ_{xy}) at 1.2 K. We then derived the longitudinal conductivity (σ_{xx}) and transverse conductivity (σ_{xy}) through the relation of [51]

$$\sigma_{xx} = \frac{\rho_{xx}}{\rho_{xx}^2 + \rho_{xy}^2}, \sigma_{xy} = \frac{\rho_{xy}}{\rho_{xx}^2 + \rho_{xy}^2} \qquad \text{Eq. 4-1}$$

The measured magneto-conductivity is the sum of σ_{xx}^{Drude} and σ_{xx}^{HLN} [107]. The component of σ_{xx}^{Drude} is the magneto-conductivity derived from the Drude model, which only includes the classical effects. The second component of σ_{xx}^{HLN} is the Hikami-Larkin-Nagaoka (HLN) correction to the classical magneto-conductivity when the quantum effects such as WL or WAL are considered. To analyze the quantum effects on the magneto-conductivity, the classical term must be removed. The longitudinal resistance in the presence of WL (WAL) effects is larger (smaller) than that with only classical effects
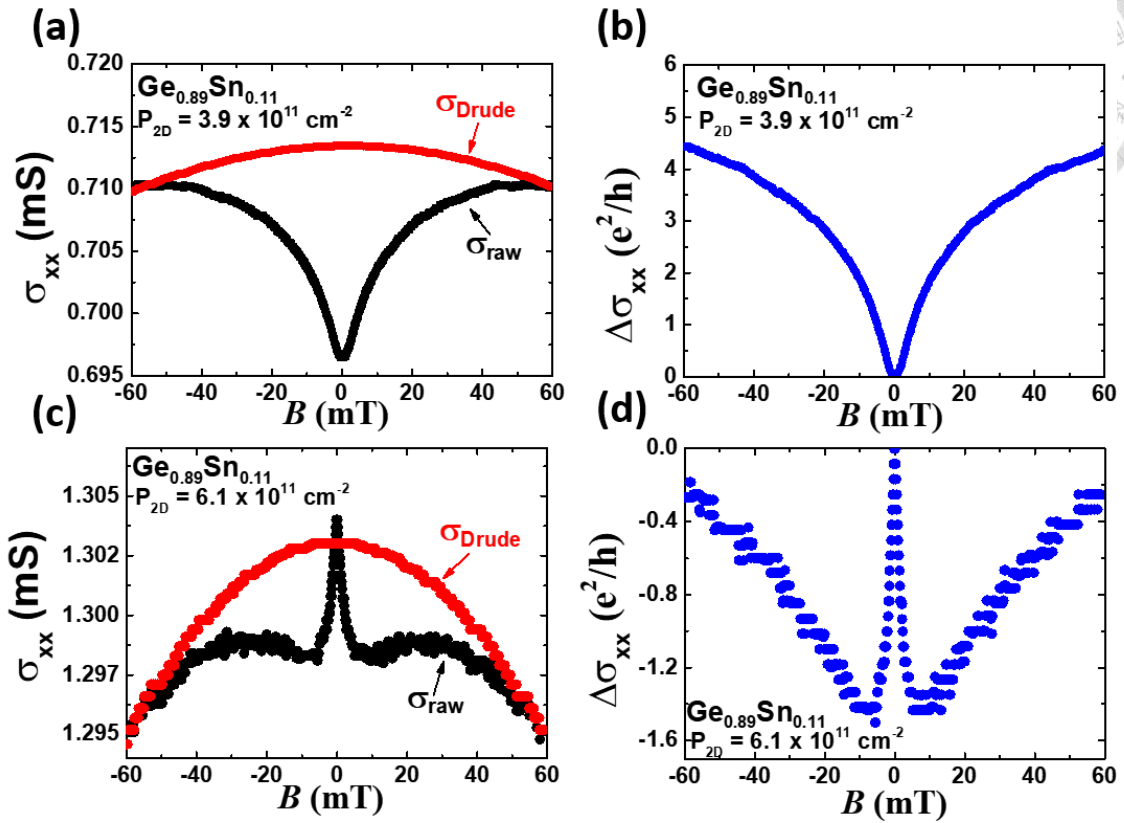
Fig. 4-2 Raw data of longitudinal conductivity (black) and the estimated σ_{xx}^{Drude} (red) for p_{2D} = (a) 3.9×10^{11} cm^{-2} and (c) $p_{2D} = 6.1 \times 10^{11}$ cm^{-2}. The corrected conductivity σ_{xx}^{HLN} after shifting $\sigma_{xx}^{HLN}(0)$ to zero for (b) $p_{2D} = 3.9 \times 10^{11}$ cm^{-2} and (d) $p_{2D} = 6.1 \times 10^{11}$ cm^{-2}. The Sn fraction in the GeSn/Ge heterostructure is 11%.

at $B = 0$ [68]. Applying a perpendicular magnetic field suppresses the WL/WAL effects.

In this work, the classical part of the longitudinal resistance (ρ_{xx}) was taken at $B = 60$ mT,

and we used

$$\sigma_{xx}^{Drude}(B) = \rho_{xx,B(60mT)}/[\rho_{xx,B(60mT)}^2 + \rho_{xy}^2(B)] \qquad \text{Eq. 4-2}$$

to estimate the contributions of σ_{xx}^{Drude}. This is shown in Fig. 4-2 (a) and (c) in red color,

and the black curve represents the raw data of the measured conductivity. After the

subtraction of the Drude term, we define $\Delta\sigma_{xx}(B) \equiv \sigma_{xx}^{HLN}(B) - \sigma_{xx}^{HLN}(0)$ (Fig. 4-2 (b)

and (d)).
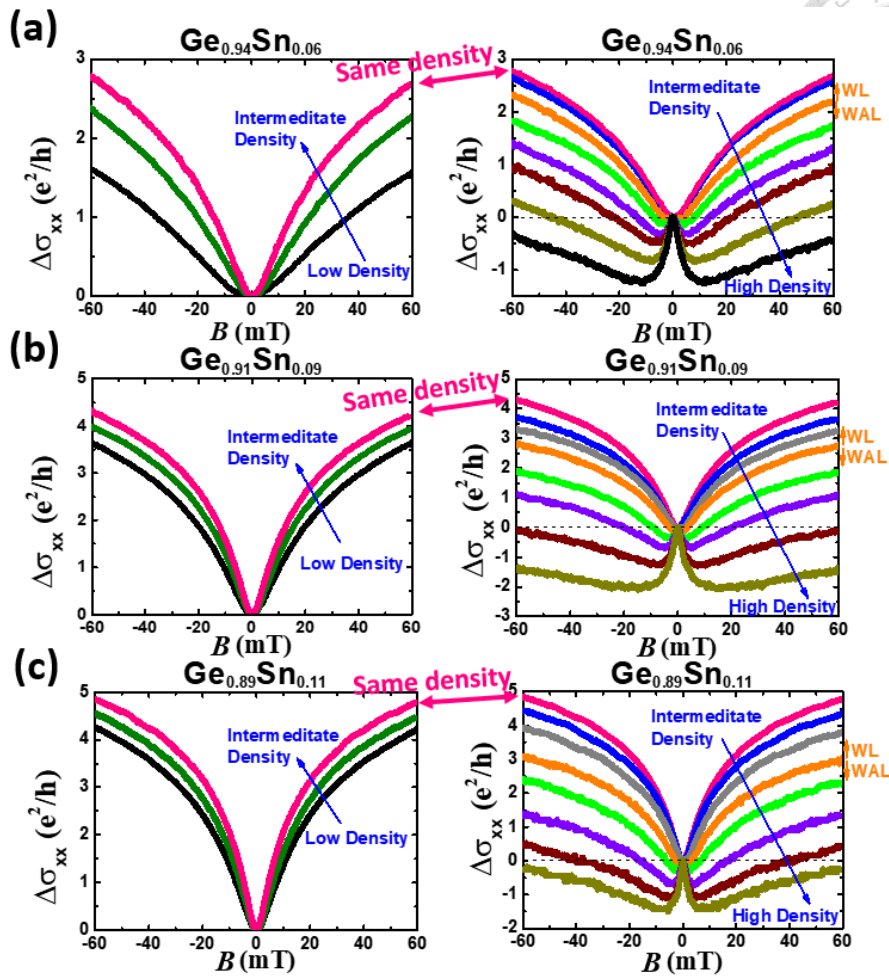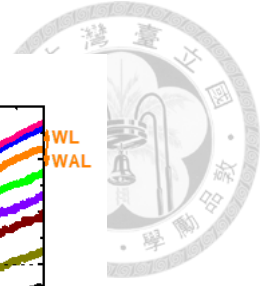
Fig. 4-3 (a)-(c) $\Delta\sigma_{xx}^{HLN}$ versus magnetic field under various carrier densities for the Ge$_{0.94}$Sn$_{0.06}$/Ge, Ge$_{0.91}$Sn$_{0.09}$/Ge, and Ge$_{0.89}$Sn$_{0.11}$/Ge heterostructures, respectively. The orange curves indicate the onsets of WAL.

Fig. 4-3 (a)-(c) show the WL/WAL patterns under various carrier densities with Sn fractions of 6%, 9%, and 11%, respectively. Transitions from WL to WAL pattern are observed in all GeSn/Ge heterostructurs. They also have similar trends: at a low density regime, the WL patterns are more pronounced as the density increases (left column). At an intermediate density regime, the WL pattern shows the opposite trend as the density increases. Finally, the WAL features appear (orange curve) and become more pronounced as the density increases further.

60
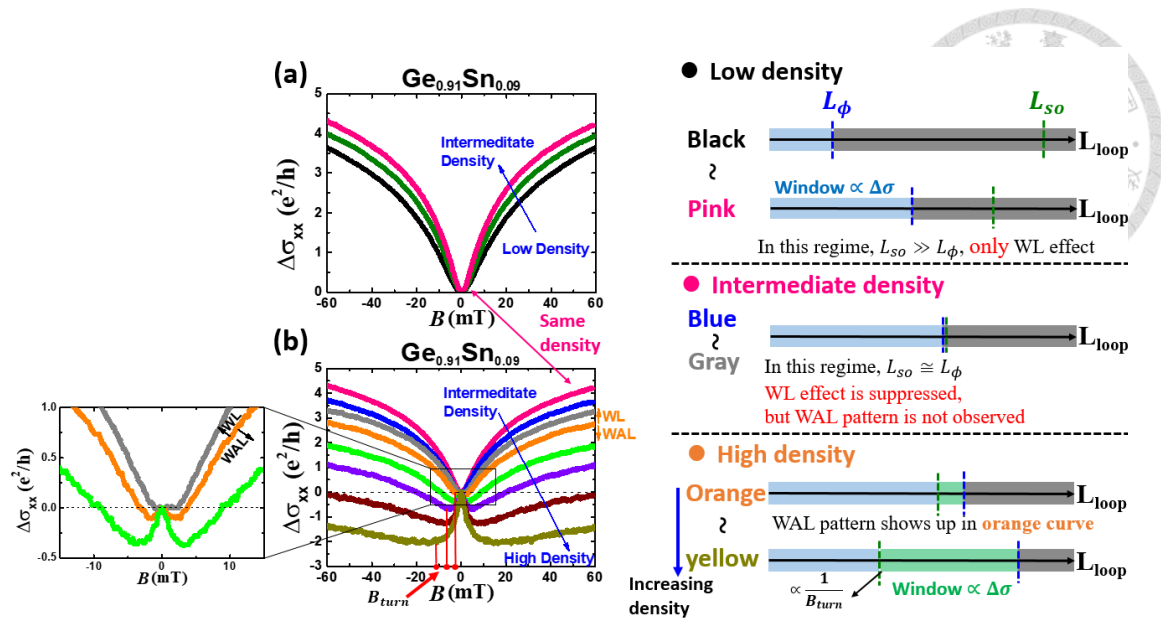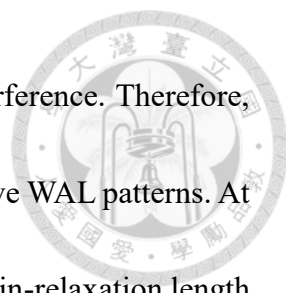
Fig. 4-4 (a)-(b) The density dependence of WL/WAL pattern for the $Ge_{0.91}Sn_{0.09}$/Ge heterostructure and the relationship between L_ϕ and L_{so} with different carrier densities. Inset of (b): A zoom-in figure to show transition clearly.

We explain this trend by using the picture described in section 2-3 (Fig. 4-4). As the density increases, the diffusion coefficient ($D = V_F^2 \times \tau_{tr}/2$) also increases due to a larger Fermi velocity and a longer transport lifetime because of stronger screening effects. Hence, the phase-coherence length ($L_\phi = \sqrt{D\tau_\phi}$) increases as well. However, the spin-relaxation length decreases due to the stronger SOC effect. As the density increase at a low density regime (black curve to pink curve), the SOC strength is very weak since both the Fermi wavevector and electric field are small. The spin-relaxation length (L_{so}) is much longer than the phase-coherence length (L_ϕ) (Fig. 4-4 (a)), so only WL patterns are observed. The change in the magneto-conductivity with the magnetic field becomes larger as the density increases since more loops contribute to the constructive interference. In an intermediate density regime (pink curve to gray curve), the phase-coherence length and spin-relaxation length becomes comparable, so there are some loops satisfying the

61

relation of $L_{so} < L_{loop} < L_\phi$ and contribute to the destructive interference. Therefore, the WL pattern is suppressed, but this effect is still too weak to observe WAL patterns. At a higher density regime, the SOC strength is strong enough, so the spin-relaxation length becomes shorter than the phase-relaxation length, leading to the presence of WAL features (orange curve). When the density increases, the difference between the phase-coherence length and spin-relaxation length becomes larger, and more loops satisfy the relation $L_{so} < L_{loop} < L_\phi$. Thus, the difference between the smallest magneto-conductivity and the conductivity at zero magnetic field becomes larger (orange curve to yellow curve). Furthermore, the magnetic field (B_{turn} defined in chapter 2) corresponding to the lowest $\Delta\sigma_{xx}$ increases as the density increases owing to a shorter spin-relaxation length.

4-2 Hikami-Larkin-Nagaoka (HLN) model

To quantitatively analyze the WL/WAL features, we evaluate the SOC strength by fitting the magnetoresistance data to the HLN model. The Rashba SOC Hamiltonian in a HH band is k-cubic dependent and written as $\boldsymbol{H}_{so}^{HH} = \alpha_3 E_z i(k_-^3\sigma_+ - k_+^3\sigma_-)$ while the Hamiltonian in a LH band is linearly dependent on k by $\boldsymbol{H}_{so}^{LH} = \alpha_1 E_z i(k_-\sigma_+ - k_+\sigma_-)$ [36]. $\alpha_{3(1)}$ represent the k-cubic (linear) Rashba coefficient and E_z represents the average vertical electric field along the z-direction. $k_\pm = k_x \pm ik_y$ are the two $k_\parallel$ components, and $\sigma_\pm = (\sigma_x \pm \sigma_y)/2$ are the combinations of Pauli spin matrices. The
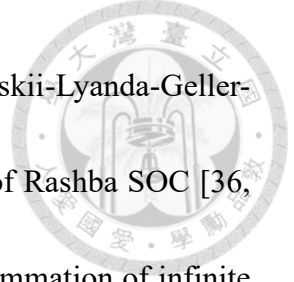
most general form to describe the WL/WAL patterns is the Iordanskii-Lyanda-Geller-Pikus (ILP) model which includes both k-linear and k-cubic terms of Rashba SOC [36, 63]. The ILP model does not have a closed form and includes the summation of infinite series of B_ϕ and B_{so}. If we only consider the contributions of the Rashba SOC effects from the HH band (i.e. only the k-cubic contribution), ILP model could be simplified to a closed form [63], which is known as the HLN model [108]. The formula is written as follows [14, 63]:

$$\Delta\sigma_{xx} = \frac{e^2}{2\pi^2\hbar}\left\{\Psi\left(\frac{1}{2}+\frac{B_\phi}{B}+\frac{B_{so}}{B}\right)+\frac{1}{2}\Psi\left(\frac{1}{2}+\frac{B_\phi}{B}+\frac{2B_{so}}{B}\right)\right.$$
$$-\frac{1}{2}\Psi\left(\frac{1}{2}+\frac{B_\phi}{B}\right)-ln\left(\frac{B_\phi+B_{so}}{B}\right)-\frac{1}{2}ln\left(\frac{B_\phi+2B_{so}}{B}\right) \qquad \text{Eq. 4-3}$$
$$\left.+\frac{1}{2}ln\left(\frac{B_\phi}{B}\right)\right\}$$

, where B_ϕ and B_{so} are the characteristic magnetic field corresponding to the phase-coherence time and spin-relaxation time.

To justify this assumption, we need to check whether the carriers only occupy in the HH band by taking the Fourier transform of the longitudinal resistivity (ρ_{xx}). The inset in Fig. 4-5 (a)~(c) shows the periodical oscillations of ρ_{xx} versus the reciprocal magnetic field. The presence of the periodicity is due to the Fermi level sweeping over consecutive Landau levels (Fig. 2-4). Each Landau level has a degeneracy of eB/h, so
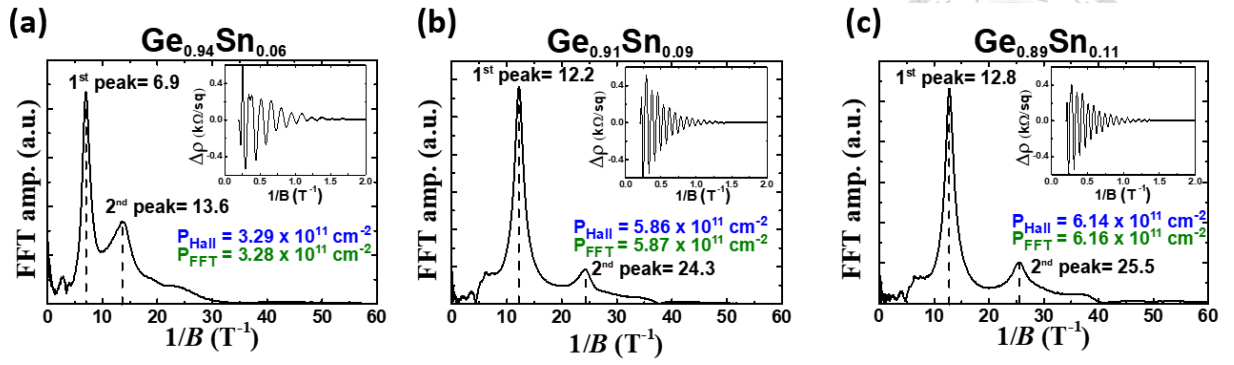
Fig. 4-5 Fast Fourier transformation of $\Delta\rho_{xx}$ for (a) $Ge_{0.94}Sn_{0.06}$/Ge, (b) $Ge_{0.91}Sn_{0.09}$/Ge, and (c) $Ge_{0.89}Sn_{0.11}$/Ge heterostructures.

we have the relationship of $\nu \times eB/h = p_{2D}$. The periodicity of reciprocal magnetic field

can be calculated as [21]

$$\frac{1}{B_{period}} = \frac{1}{B_{\nu+2}} - \frac{1}{B_\nu} = \frac{2}{p_{2D}}\frac{e}{h}$$

Eq. 4-4

We define $p_{FFT} \equiv \frac{2eB_{FFT}}{h}$ with the B_{FFT} term corresponding to the peak amplitude in

the reciprocal magnetic field domain. The transformed results of the longitudinal

resistivity are shown in Fig. 4-5. There are two peaks observed and one peak has twice

the value of the other. The major peak corresponds to the carrier density and the second

peak is the harmonic term [109]. We used the first peak to calculate p_{FFT} and compared

it to the Hall measurement results (p_{Hall}). Those carrier densities match with each other

very well and no extra peak of B_{FFT} in the SdH oscillations shows that only the lowest

HH subband is occupied.

There are two other criteria to meet when using the HLN model. Since the HLN

model is only valid in the spin-diffusive regime [14], the spin-precession length (L_{pre})

(the distance over which holes can travel during one period of Larmor precession) needs

64
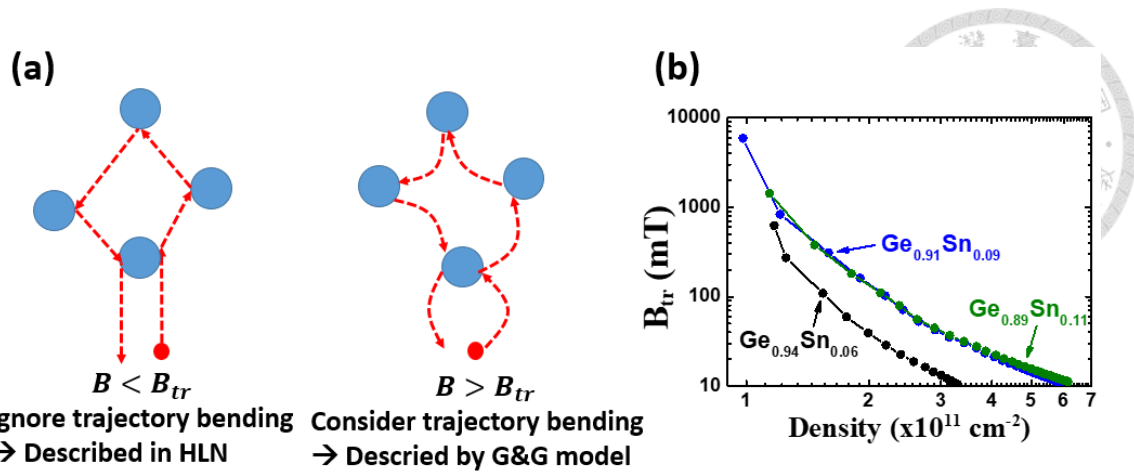
Fig. 4-6 (a) A physical picture of the transport magnetic field. (b) The transport magnetic field versus carrier density for different GeSn/Ge heterostructures.

to be longer than the mean free path (L_{tr}) as the applied magnetic field (B) is smaller than

the corresponding transport field (i.e. $B < B_{tr} = \hbar/(2eL_{tr}^2)$). The physical picture of the

transport field (B_{tr}) is shown in Fig. 4-6 (a). For a magnetic field smaller than the

transport field, the orbital bending due to the magnetic field can be ignored compared to

the scale of mean free path (L_{tr}) [68]. On the other hand, for a magnetic field larger than

the transport field, we need to consider the orbital bending and the more general

formalism is described by the Glazov and Golub (G&G) model [110]. The calculated

results of the transport field are shown in Fig. 4-6 (b). Since the smallest transport field

is 10 mT, we focus our fitting regime within ± 10 mT.

We used the HLN model (Eq. 4-3) with B_ϕ and B_{so} as the fitting parameters to fit

the WL/WAL patterns. Fig. 4-7 (a) and Fig. 4-8 (a) show the fitting results when only WL

or WAL patterns are observed, respectively. To evaluate the fitting results, we calculate

the coefficient of determination (R^2) [111], which reflects how "good" the fitting function

is. For a set of data points $\{(x_1, y_1), (x_2, y_2), (x_3, y_3)...(x_N, y_N)\}$, we can find a fitting

65
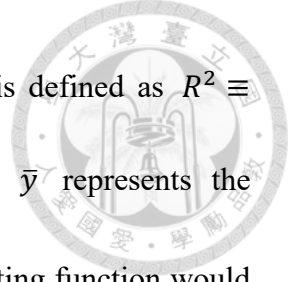
function $f(x)$ with $f_i = f(x_i)$. The coefficient of determination is defined as $R^2 \equiv$

$1 - \frac{SS_{res}}{SS_{tot}}$, where $SS_{res} = \sum(y_i - f_i)^2$ and $SS_{tot} = \sum(y_i - \bar{y})^2$. $\bar{y}$ represents the

average of y_i. The closer to one for R^2 is, the more precise this fitting function would

be. Fig. 4-7 (b)-(e) show the color mapping of R^2. For R^2 greater than 0.8 (0.9, 0.95, or

0.98), we set the color to be skin color, while the other cases are set to be black. At a low

density regime with only WL patterns, B_{so} is not converged, which expands from 10^{-4}

to 10^{-12} with high R^2 values. On the other hand, at a high density regime when both WL

and WAL patterns are observed (Fig. 4-8 (b)-(d)), the highest R^2 converges for a limited

region of B_{so}.
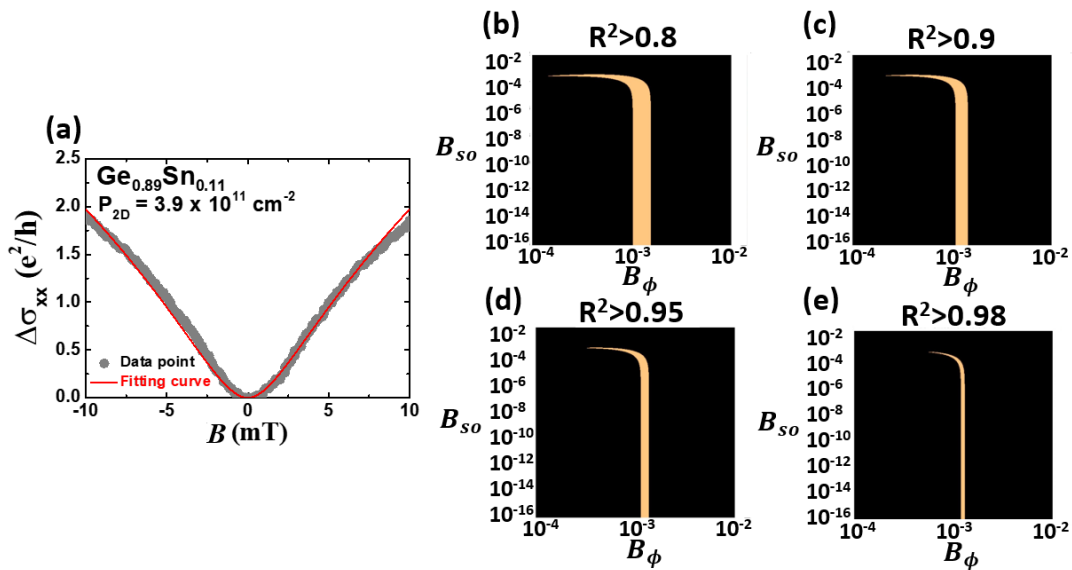
Fig. 4-7 (a) Fitting results of $\Delta\sigma_{xx}$ for the Ge$_{0.89}$Sn$_{0.11}$/Ge heterostructure with only WL patterns observed. (b)-(e) Color mapping of B_{so} and B_{ϕ} for different R^2.
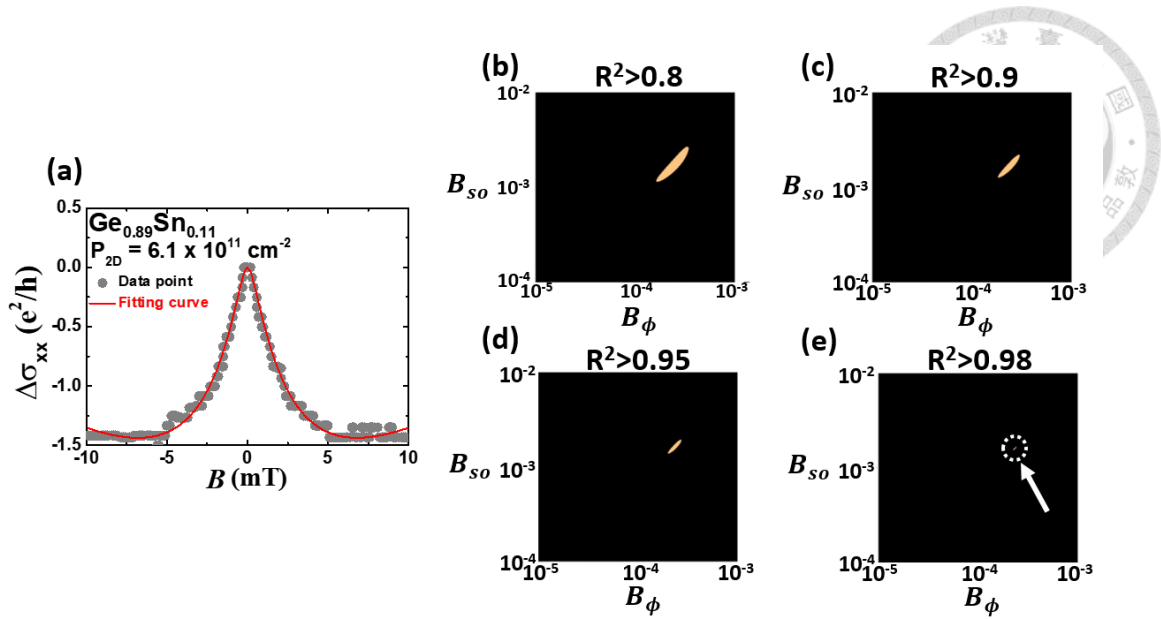
Fig. 4-8 (a) Fitting results of $\Delta\sigma_{xx}$ for the Ge$_{0.89}$Sn$_{0.11}$/Ge heterostructure with both WL/WAL patterns observed. (b)-(e) Color mapping of B_{so} and B_{ϕ} for different R^2.

The fitting results for the GeSn/Ge heterostructures under various carrier densities are shown in Fig. 4-9 (a)-(c). For all structures, as the density increases, a transition from WL to WAL is observed. The magneto-conductivity near the cross-over density is shown as the orange curve in each plot. By increasing the gate voltage to induce more holes in the GeSn QW, a larger electric field perpendicular to the hetero-interface is created, which results in stronger SIA and enhances the Rashba SOC effects [112]. The strength of Rashba SOC in the HH band is expected to be proportional to k_F^3 [10, 14, 36]. A higher carrier density leads to a larger k_F and stronger SOC effects. Similar to our prior work
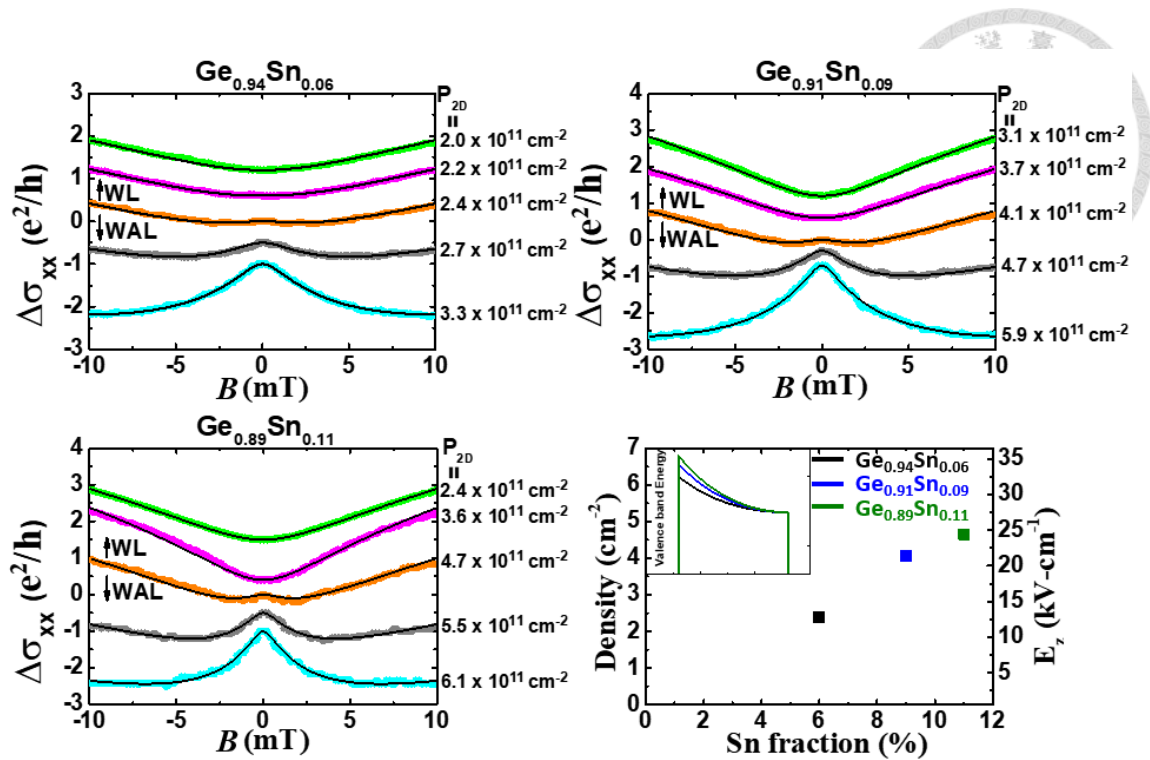
Fig. 4-9 (a)-(c) Magneto-conductivity for different GeSn/Ge heterostructures. Black lines are the fitting curves by the HLN formula, and the experimental data are shifted vertically for a better view. (d) The carrier density of the WL-WAL transition and the corresponding electric field (E_z) versus Sn fraction. The inset shows the corresponding band diagrams.

on SOC in Ge [14], tuning the SOC strength is enabled by top gating the undoped GeSn/Ge heterostructures. The transition density and the corresponding electric field versus the Sn fraction are plotted in Fig. 4-9 (d). For the device with a higher Sn fraction, a larger electric field is required to observe WAL. The relationship between SIA and SOC have been reported in III-V materials [112], in which the strength of SOC is the largest for the devices with the largest electric field. Intuitively, the device with a higher Sn fraction should present stronger WAL effects due to its larger atomic potential variations. The required electric fields for the transition from WL to WAL should be smaller. However, our results show an opposite trend, suggesting that there are other mechanisms responsible for these counter-intuitive results. Great matches between the experimental

data and the fitting curves by the HLN model were obtained, which validates the

assumption that only the k-cubic term of Rashba SOC dominates.

4-3 Extraction of characteristic times ($\tau_\phi, \tau_{so}, \tau_{pre}$) and characteristic lengths (L_ϕ, L_{so}, L_{pre})

After extracting B_ϕ and B_{so} through the HLN equation, we use the relationship of

$\tau_{\phi(so)} = \hbar/(4eDB_{\phi(so)})$ to evaluate the corresponding lifetimes [63, 113]. Here, $B_{\phi(so)}$

represent the characteristic magnetic field corresponding to the phase-coherence time (τ_ϕ)

and spin-relaxation time (τ_{so}), and $D(= V_F^2 \times \tau_{tr}/2)$ is the diffusion coefficient. V_F is

the Fermi velocity and τ_{tr} is the carrier transport lifetime. Fig. 4-10 (a) shows the

characteristic times (τ_ϕ and τ_{so}) versus the carrier density and Fig. 4-10 (b) shows the

corresponding characteristic lengths (L_ϕ and L_{so}) by $L_{\phi(so)} = \sqrt{D\tau_{\phi(so)}}$. The circled

points represent the transition from WL to WAL (or the onset of WAL). The spin-

relaxation time decreases monotonically with the carrier density, which is due to the

stronger SOC effect [36]. As the carrier densities increase by 38%, 45%, and 32%, the

spin-relaxation time is reduced by 77%, 85%, and 75% for the $Ge_{0.94}Sn_{0.06}$, $Ge_{0.91}Sn_{0.09}$,

and $Ge_{0.89}Sn_{0.11}$ devices, respectively. For a comparison, the spin-relaxation time of

2DHG in a Ge QW was reduced by a factor of 63% with a density increase of 49% [36]

69

Table 4-1 $\Delta\tau_{so}$, Δp_{2D}, and the ratio of $|\Delta\tau_{so}|/\Delta p_{2D}$ for Ge, Ge$_{0.94}$Sn$_{0.06}$, Ge$_{0.91}$Sn$_{0.09}$, and Ge$_{0.89}$Sn$_{0.11}$.

Physical parameters	Ge [36]	Ge$_{0.94}$Sn$_{0.06}$	Ge$_{0.91}$Sn$_{0.09}$	Ge$_{0.89}$Sn$_{0.11}$
$\Delta\tau_{so}$	-63%	-77%	-85%	-75%
Δp_{2D}	49%	38%	45%	32%
Ratio ($|\Delta\tau_{so}|/\Delta p_{2D}$)	1.29	2.03	1.89	2.34

(Table 4-1). For a given density, the spin-relaxation time is longer in GeSn with a higher

Sn fraction. This is counter-intuitive, and we will elaborate on this trend in the following

section.

We now turn to the density dependence of the phase-coherence time. There are two

major scattering sources to account for the dephasing. The first one is the hole-phonon

scattering and the other is the hole-hole scattering [52]. Fig. 4-10 (a) shows the phase-

coherence times increase slightly with the carrier density. Since the data are measured at

T = 1.2 K, only few phonon modes are activated and the hole-phonon interaction could

be ignored. Therefore, the increasing trend could be attributed to the reduction of hole-
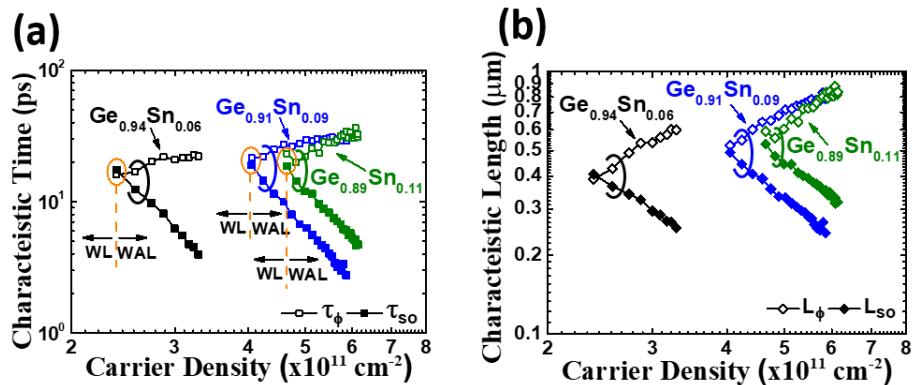
Fig. 4-10 (a) Characteristic time (phase-coherence time (τ_ϕ) and spin-relaxation time (τ_{so})) and (b) characteristic length (phase-coherence length (L_ϕ) and spin-relaxation length (L_{so})) versus density for three GeSn/Ge heterostructures.
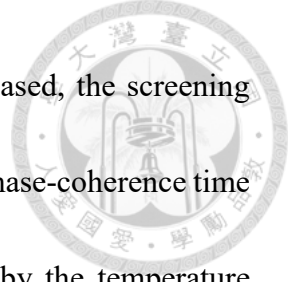
hole scattering events. Although the density inside the QW is increased, the screening

effect further suppresses the hole-hole interaction [107]. Hence, the phase-coherence time

would increase. The dephasing mechanism is further investigated by the temperature

dependence of phase-coherence time in section 4.5.

To investigate spin transport in the GeSn/Ge heterostructures, the spin-precession

length (L_{pre}) and the mean free path (L_{tr}) were calculated and compared. The

characteristic lengths are given by $L_{pre(tr)} = V_F \times \tau_{pre(tr)}$, where the Fermi velocity is

defined as $V_F = \hbar k_F / m^*$, and τ_{tr} is defined as $\tau_{tr} = m^* \mu / e$. The Fermi wavevector

(k_F) and mobility (μ) are derived by the Hall measurement results, and the effective mass

is extracted from the temperature-dependent SdH oscillations (section 3-3) [97]. The spin-

precession time (τ_{pre}) can be calculated by using the DP spin-relaxation theory [64]. The

DP mechanism is used to describe the spin-relaxation due to the random variations of the

effective magnetic field during the transport (Fig. 4-11 (a)). The Rashba SOC creates a k-

dependent magnetic field (B_{Rashba}) in the 2DHG plane. The direction of the effective

magnetic field changes randomly since the 2DHG carriers frequently collide with

impurities. Thus, the momentum direction and the spin direction are altered rapidly, so
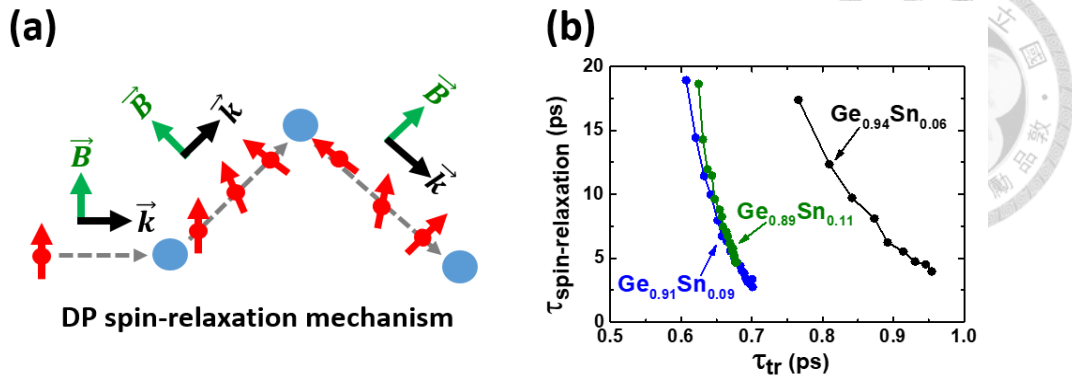
Fig. 4-11 (a) Schematic of DP spin-relaxation mechanism. (b) Spin-relaxation time versus transport lifetime for different GeSn/Ge heterostructures.

the spin direction is randomized. One feature of the DP mechanism is that the spin-relaxation time is inversely proportional to the transport lifetime [67]. There is little time for spins to respond to the fast-changing Rashba field if the collisions occur too frequently. As the carrier density increases, the mobility becomes higher and the scattering lifetime becomes longer, leading to a shorter spin-relaxation time (Fig. 4-12 (b)).

We further use the equation of $1/\tau_{so} = 2|\Omega_3|^2 \tau_{tr}$ [114] from the DP theory to derive the spin-precession frequency (Ω_3) and spin-precession time ($\tau_{pre} = 1/\Omega_3$). The transport lifetime (τ_{tr}), spin-precession time (τ_{pre}), spin-precession length (L_{pre}), and mean free path (L_{tr}) are plotted against the carrier density in Fig. 4-12. The spin-precession length is longer than the mean free path for all devices, which suggests that the system is in the spin-diffusive regime and validates the use of the HLN formula in this work. For the spin-FET applications [2], the devices must be operated in the spin-ballistic

72
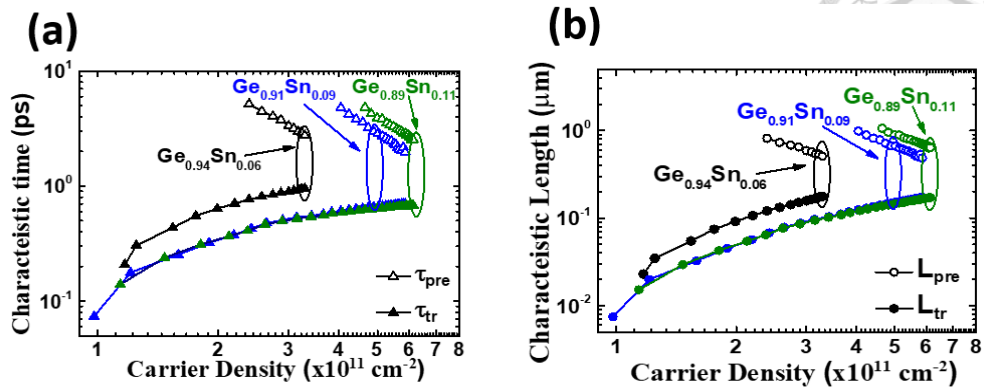
Fig. 4-12 (a) Characteristic time (spin-precession time (τ_{pre}) and transport lifetime (τ_{tr})) and (b) characteristic length (spin-precession length (L_{pre}) and mean free path (L_{tr})) versus density for three GeSn/Ge heterostructures.

regime ($L_{pre} < L_{tr}$), where a spin can complete at least one full cycle of precession along

a certain axis before scattering. Therefore, by designing a shorter channel length such that

carriers transport ballistically through the channel, the spin orientations can be controlled

through Rashba SOC without scattering disturbance. In our case, the spin ballistic

transport can be achieved by further increasing the carrier density, which results in a

shortened spin-precession time and a longer transport time due to the stronger SOC and

screening effects. This can be done simultaneously by top gating the undoped GeSn/Ge

heterostructures to modulate the carrier density.

4-4 Strain effect on Rashba SOC

To further investigate the Sn effects on the SOC strength in the GeSn QW, the k-cubic Rashba coefficients (α_3) and the spin-splitting energy (Δ_{so}) were estimated by the expression $\hbar\Omega_3 = \Delta_{so} = \alpha_3 E_z k_F^3$ [14]. α_3 can be derived with the average electric field (E_z) calculated by Gauss's law and the Fermi wavevetor by the Hall density ($k_F = \sqrt{2\pi p_{2D}}$). The spin degeneracy in the HH band is broken due to the SOC effect with energy shifts of $\pm\Delta_{so}$, so the energy difference between two spin subbands at a given k_F is $2\Delta_{so}$ (Fig. 4-1). Fig. 4-13 shows the spin-splitting energy as a function of carrier density, and the red-dashed line represents the theoretical prediction ($\Delta_{so} \propto p_{2D}^{5/2}$) for the k-cubic Rashba SOC [14]. For all GeSn/Ge heterostructures, as the carrier density increases by gating, the spin splitting energy is increased due to the enhanced Rashba SOC effect with the slopes close to the theoretical prediction.
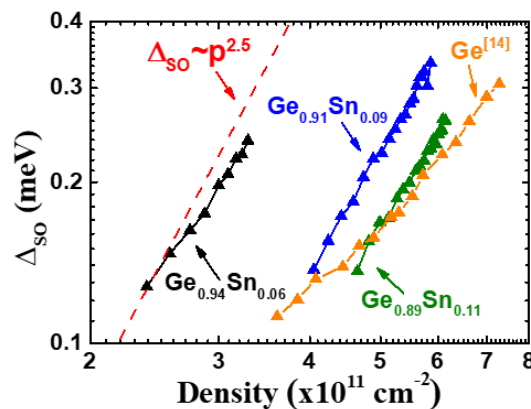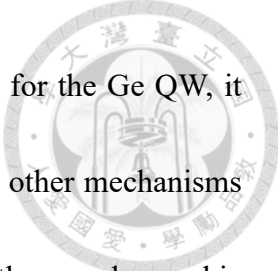
Fig. 4-13 Spin splitting energy (Δ_{so}) versus carrier density for three GeSn/Ge heterostructures and Ge QW [14]. The red-dashed line represents a theoretical curve predicted by the k-cubic relationship [14].

74

While the splitting energy for all GeSn QWs is larger than that for the Ge QW, it decreases as the Sn fraction increases. Our data strongly suggest that other mechanisms such as strains in the epitaxial films might come into play [115]. For the pseudomorphic heterostructures used in this work, the lattice mismatch leads to strains in the epitaxially grown films. For III-V ternary or quaternary materials, the lattice mismatch is mitigated easily by tuning the compositions in the compounds, so spin-orbit energy splitting in the hole bands induced by strains can be avoided. For group-IV epitaxy, strains occur commonly due to the different lattice constants of the constituents (C, Si, Ge, and Sn). The strains result in band splitting and deformations of the LH and HH subbands. In addition, the deeper confinement potential for a GeSn QW with a higher Sn fraction can further enhance this energy splitting. For the GeSn/Ge heterostructures, due to the large lattice mismatch between Ge and Sn (∼ 15% [116]), the strain effects are expected to be significant. The strain effects on SOC have been reported for III-V materials both experimentally [115] and theoretically [10, 15], but not yet demonstrated for any group-IV materials and their compounds.

The physics of the suppressed Rashba SOC effects for the GeSn devices with a higher Sn fraction is described as follows. For 2DHG in the GeSn/Ge heterostructures, the total angular momentum $(\vec{J} = \vec{L} + \vec{S})$ is mainly quantized along the growth (z) direction of the GeSn/Ge heterostructures [10, 15, 117], since only the z-axis maintains

75
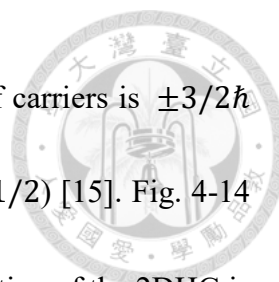
the rotational symmetry. The z-component of angular momentum of carriers is $\pm3/2\hbar$ for the HH states ($m_j \pm 3/2$) and $\pm1/2\hbar$ for the LH states ($m_j \pm 1/2$) [15]. Fig. 4-14 (a) shows the spin orientations of holes in the HH state. Since the motion of the 2DHG is confined in the x-y plane and the electric field is along the z-direction, the resulting effective magnetic field (B_{Rashba}) created by the Rashba SOC also lies in the x-y plane [63] with the SOC Hamiltonian of $H_{so} = \left(\frac{\hbar}{4m_0^2c^2}\right)\vec{\sigma}\cdot(-\nabla V \times \vec{P})$ [10]. If, for example, the effective magnetic field B_{Rashba} points to x-axis, the spin would tend to precess along this axis due to the quantization of the angular momentum in the x direction (Fig. 4-14 (b)). Under the uncertainty principle, a spin cannot be measured with two definite components of angular momentum along two orthogonal axes. This would result in two
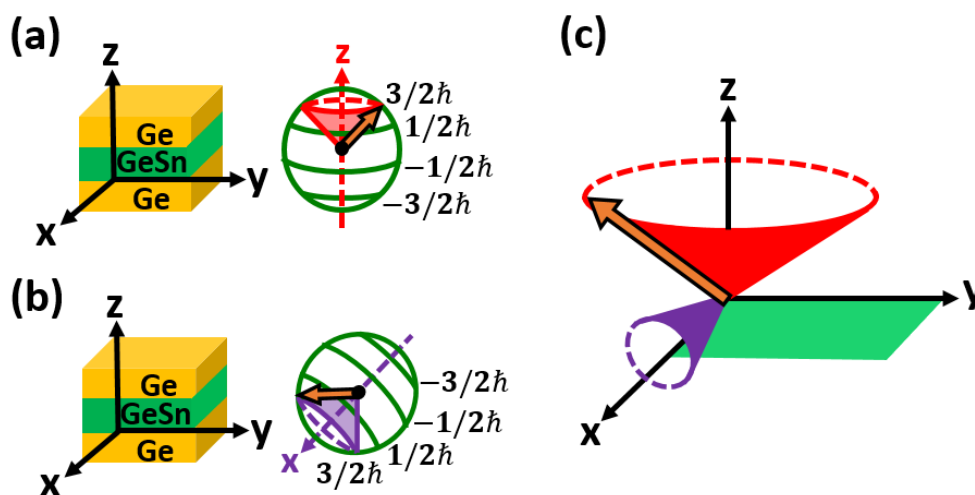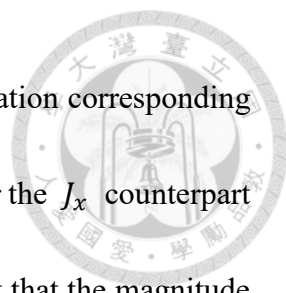
Fig. 4-14 (a) The spin orientation of HH states in a GeSn QW due to the quantum confinement effect. (b) The spin orientation in the HH states under an induced magnetic field by SOC (B_{Rashba}). (c) Competition between the quantum confinement (J_z quantization) and the SOC effects (J_x quantization).

competing axes for the spin rotation (Fig. 4-14 (c)). The J_z quantization corresponding to the energy spiltting of the HH and LH bands (Δ_{hl}) is dominant over the J_x counterpart associated with the spin-splitting energy (Δ_{so}). This is due to the fact that the magnitude of the HH-LH energy splitting in the strained GeSn layer is relatively large (~ 10 meV) [118, 119] compared to our experimental results of the spin-splitting energy, which is only on the order of 0.1 meV. Thus, the quantization along the z-axis is dominant. Moreover, as the Sn fraction is higher, the larger compressive strain and deeper valence band potential further enhances the splitting of the HH and LH bands, resulting in a larger Δ_{hl}. This makes the effects of J_z quantization even stronger than J_x, suppressing the Rashba SOC strength further. A similar mechanism has been reported in prior works showing the anisotropy of Zeeman splitting [120, 121].

From the discussion above, the increased energy splitting of the HH and LH bands (Δ_{hl}) due to the larger compressive strain and confinement potential results in the stronger quantization of J_z than that of J_x and simultaneously reduces the spin-splitting energy (Δ_{so}). The negative dependency of Δ_{so} on Δ_{hl} is reflected on the Δ_{hl} dependence of the k-cubic term in the Rashba coefficient (α_3). This coefficient α_3 for the first HH subbands is given by the third-order Löwdin perturbation theory [15, 117, 122],

$$\alpha_3 = \frac{e\hbar^4}{m_0^2} c\gamma_3(\gamma_2 + \gamma_3)\left[\frac{1}{\Delta_{11}^{hl}}\left(\frac{1}{\Delta_{12}^{hl}} - \frac{1}{\Delta_{12}^{hh}}\right) + \frac{1}{\Delta_{12}^{hl}\Delta_{12}^{hh}}\right] \qquad \text{Eq. 4-5}$$

where c is a constant depending on the QW structure and is $64/9\pi^2$ for an infinitely deep

77
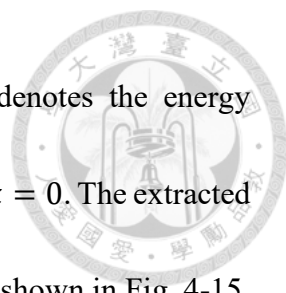
rectangular QW [15], γ_i are the Lüttinger parameter, and Δ_{ij}^{hl} denotes the energy difference between the ith HH subband and j^{th} LH subband energy at $k = 0$. The extracted Rashba coefficients of the k-cubic terms versus electric field (E_z) are shown in Fig. 4-15. As predicted by Eq. 4-5, for the GeSn/Ge heterostructure with a higher Sn fraction, its HH-LH splitting energy is larger, leading to the smaller Rashba coefficient.

For all GeSn QWs, α_3 is larger than that in the Ge QW, showing the potentials of the GeSn-based devices for spintronic applications. Note that for Ge$_{0.94}$Sn$_{0.06}$ and Ge devices, there is a negative dependency of α_3 on the electric field while for Ge$_{0.91}$Sn$_{0.09}$ and Ge$_{0.89}$Sn$_{0.11}$ devices, α_3 is insensitive to E_z. The negative trend has been observed in Al$_{0.3}$Ga$_{0.7}$As/GaAs structures [117], which was due to a further splitting between the HH and LH bands by gating. This effect is even more pronounced in a hetero-junction triangular QW because the confinement potential of a triangular QW depends on the band
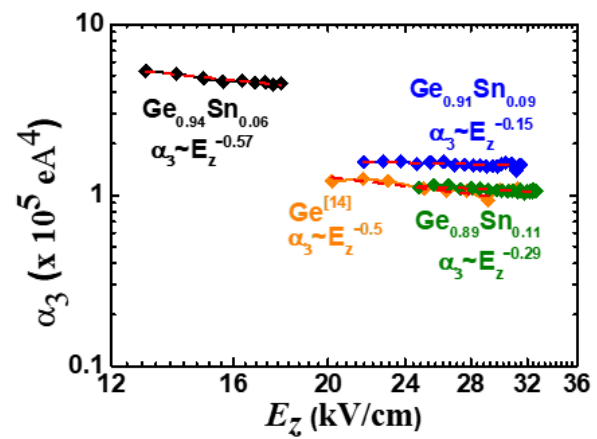
Fig. 4-15 Spin-orbit coefficient (α_3) versus vertical electric field (E_z).
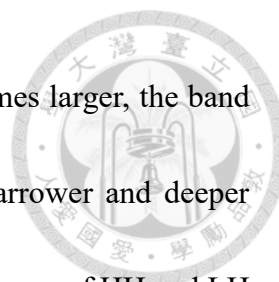
bending of the structure [117] (Fig. 4-16). As the electric field becomes larger, the band bending at the heterostructure is more pronounced, leading to a narrower and deeper triangular QW. With a stronger quantum confinement, the splitting energy of HH and LH bands becomes larger, resulting in a decrease of Rashba coefficient (α_3) with the triangular potential approximation ($\alpha_3 \propto E_z^{-s}, s = 4/3$) [117]. For a square QW, the confinement potential mainly depends on the band offsets at the heterojunction (Fig. 4-16). The external electric field only causes minor effects on the splitting of HH and LH bands. The dependence of the Rashba coefficient on the electric field should be weaker [14, 122], and indeed a weak dependence ($s = 0.5$) for the $Ge_{0.94}Sn_{0.06}$ and Ge heterostructures was observed. On the other hand, if the energy splitting of the HH and LH bands is dominated by the strain effects, the effects of HH-LH splitting through the electric field would be even weaker. Hence, $Ge_{0.91}Sn_{0.09}$ and $Ge_{0.89}Sn_{0.11}$ heterostructures show a much weaker dependence of α_3 on the electric field.
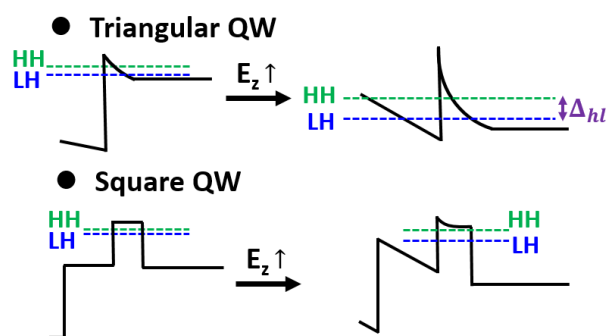
Fig. 4-16 Splitting energy between the HH and LH states by gating a triangular and square QW.

4-5 Temperature dependence of weak localization and weak-anti localization in GeSn/Ge heterostructures
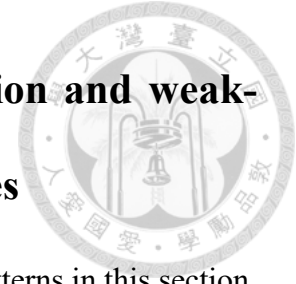
We investigate the temperature dependence of the WL/WAL patterns in this section. Fig. 4-17 shows the magneto-conductivity at different temperatures (4, 3, 2, 1.6, and 1.2 K) for the $Ge_{0.94}Sn_{0.06}$/Ge, $Ge_{0.91}Sn_{0.09}$/Ge, and $Ge_{0.89}Sn_{0.11}$/Ge heterostructures. Those patterns could be divided into three types based on the regime of carrier density. At a low carrier density regime (Fig. 4-17 (a)-(c)) where only WL patterns are observed, the WL patterns are more pronounced as the temperature is reduced. At an intermediate carrier density regime (Fig. 4-17 (d)-(f)), a transition from WL to WAL occurs as the temperature is reduced. The curves in Fig. 4-17 (d)-(f) have been shifted vertically in order to show the transition curves (orange curves) clearly. In a high density regime (Fig. 4-17 (g)-(i)), the WAL patterns are more pronounced at lower temperatures. To explain this trend, we need to understand how the phase-coherence length (L_{ϕ}) and spin-relaxation length (L_{so}) change with the temperature because the WL/WAL patterns highly depend on the relative length between L_{ϕ} and L_{so}.

The spin-relaxation length is proportional to the product of spin-relaxation time (τ_{so}) and diffusion coefficient (D) with the relationship $L_{so} = \sqrt{D\tau_{so}}$ [63]. Based on the DP spin-relaxation mechanism (Fig. 4-11 (a)), there are two factors influencing the spin-

80
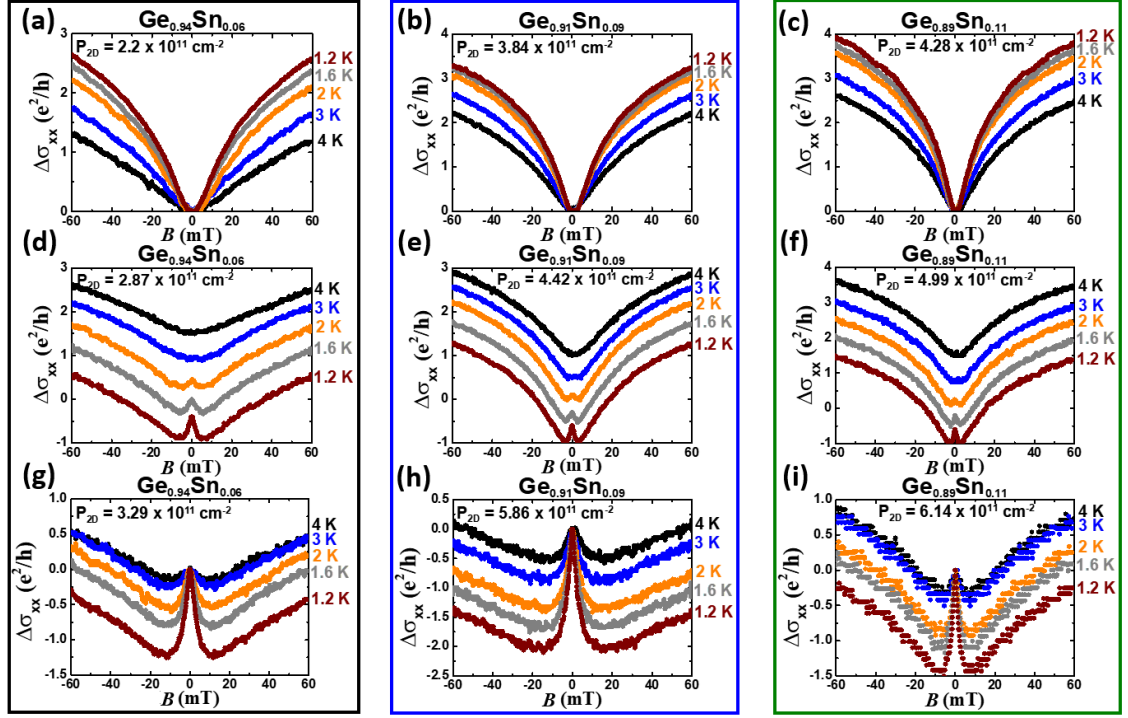
Fig. 4-17 The temperature dependence of WL/WAL patterns. (a)-(c) show the WL patterns at a low density regime. (d)-(f) show the transitions from WL to WAL at $T = 2$ K at an intermediate density regime. The data are shifted vertically to show the transition curves clearly. (g)-(i) show the WAL patterns at a high density regime.

relaxation time: the transport lifetime (τ_{tr}) and the strength of effective magnetic field (B_{Rashba}). The transport lifetime is inversely proportional to the spin-relaxation time, which barely changes (less than 3 %) from T = 4 K to 1.2 K for all heterostructures in this work. The effective magnetic field is determined by the z-direction electric field (E_z) and the Fermi wavevector (k_F). Both of them depend on the carrier density ($E_z = ep_{2D}/\epsilon$ and $k_F = \sqrt{2\pi p_{2D}}$) and have no dependence on temperature. The diffusion coefficient ($D = V_F^2 \times \tau_{tr}/2$) also varies slightly at this temperature range. Therefore, we can deduce the spin-relaxation length without too much impact by temperature difference.
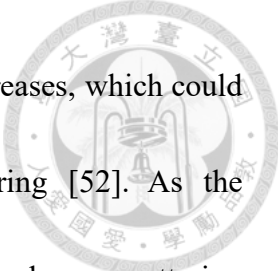
On the other hand, a phase-coherence length depends on the temperature exponentially. A phase-coherence length is given by $L_\phi = \sqrt{D\tau_\phi}$ [14]. However, the

phase-coherence time decreases exponentially as the temperature increases, which could be attributed to the hole-phonon scattering or hole-hole scattering [52]. As the temperature increases, more phonon modes are activated and the hole-phonon scattering rate ($1/\tau_{ph}$) becomes higher with a power law relation of $\tau_{ph} \propto T^{-2}$ [123]. In addition, a higher temperature also leads to an increase of the hole density because more holes have energies higher than the Fermi level, leading to a stronger hole-hole scattering rate ($\tau_{hh} \propto T^{-1}$) [123, 124]. Both processes can cause dephasing and the effective dephasing rate should be proportional to the sum ($1/\tau_\phi = 1/\tau_{ph} + 1/\tau_{hh}$). Therefore, the phase-coherence length is enhanced as the temperature is reduced.

We use Fig. 4-18 to explain the trend observed in Fig. 4-17 In a low density regime (Fig. 4-18 (a)) where the SOC effect is weak, the spin-relaxation length is much longer than the phase-coherence length. Therefore, no WAL pattern is observed and the WL pattern is more pronounced as the phase-coherence length becomes longer at lower temperatures. At an intermediate density regime (Fig. 4-18 (b)), the spin-relaxation length is slightly longer than the phase-coherence length. As the temperature decreases, the spin-relaxation length barely changes, but the phase-coherence length is increased exponentially. As a result, a transition occurs when the phase-coherence length becomes longer than the spin-relaxation length. Finally, in a high density regime (Fig. 4-18 (c))

82
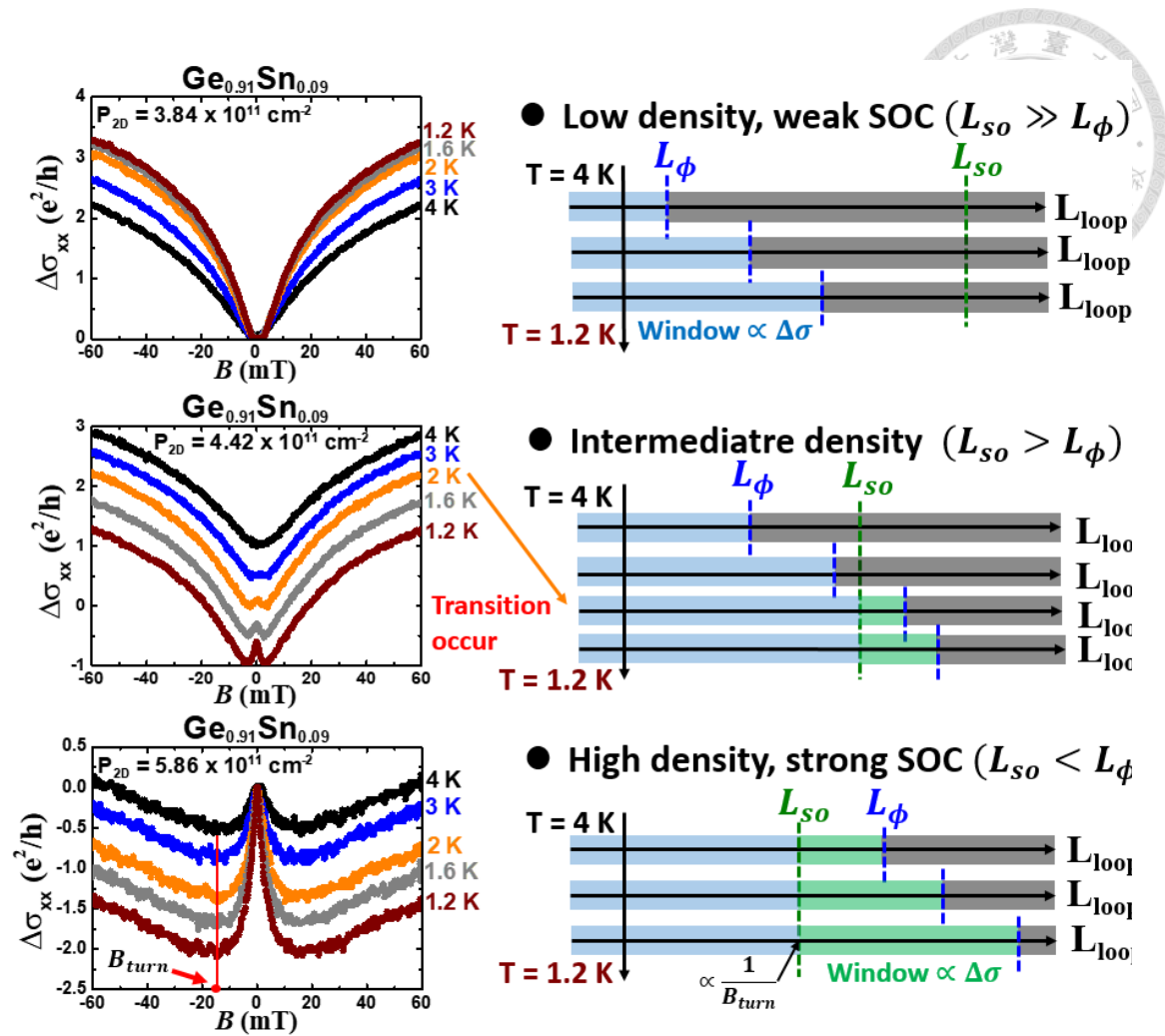
Fig. 4-18 Temperature dependence of WL/WAL patterns for the $Ge_{0.91}Sn_{0.09}$ structure at (a) a low, (b) an intermediate, and (c) a high density regimes with the relation between L_ϕ and L_{so} at different temperatures.

where the SOC effect is very strong, the spin-relaxation length is smaller than phase-coherence length. As the phase-coherence length becomes longer, more loops satisfy the relation of $L_{so} < L_{loop} < L_\phi$, and hence the WAL effect becomes stronger. Furthermore, since the spin-relaxation length does not change with temperature, the value of B_{turn} remains the same.
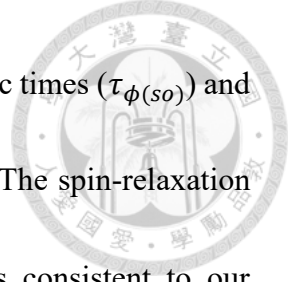
By fitting with the HLN formula, we can derive the characteristic times ($\tau_{\phi(so)}$) and

characteristic lengths ($L_{\phi(so)}$) at different temperatures (Fig. 4-19). The spin-relaxation

time (length) has weak dependence on the temperature, which is consistent to our

previous arguments. The phase-coherence time shows a relation of $\tau_\phi \propto T^{-1}$

(equivalent to $L_\phi \propto T^{-0.5}$ because of $L_\phi \propto \sqrt{\tau_\phi}$), indicating the hole-hole scattering

mechanism is dominant. The hole-hole scattering rate can be described by [123, 124].

$$
\begin{aligned}
\frac{1}{\tau_\phi} &= \frac{\pi}{2} \frac{(k_B T)^2}{\hbar E_F} ln \frac{E_F}{k_B \tau_{tr}}, \text{when } T > \frac{\hbar}{k_B \tau_{tr}} \\
&= \frac{k_B T}{2\pi N_0 D \hbar^2} ln(\pi D N_0 \hbar), \text{when } T < \frac{\hbar}{k_B \tau_{tr}}
\end{aligned}
\qquad \text{Eq. 4-6}
$$

$N_0 = \frac{m^*}{\pi \hbar^2}$ is the 2D density of states, D is the diffusion coefficient, and k_B is the

Boltzmann constant. In our case, the transport lifetime (τ_{tr}) is at the order of 1 ps (Fig.

4-12 (a)), and the corresponding temperature by Eq. 4-6 is 7.6 K. Since the data was taken
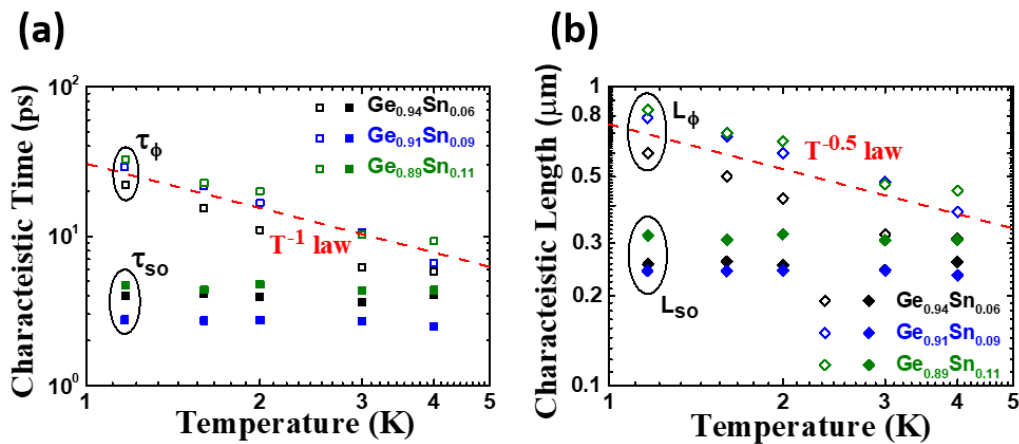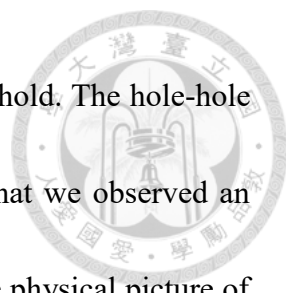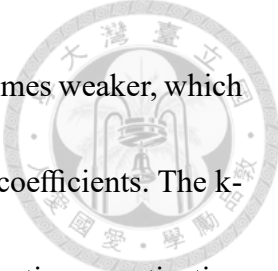
Fig. 4-19 Characteristic times (phase-coherence time (τ_ϕ) and spin-relaxation time (τ_{so})) and
(b) characteristic lengths (phase-coherence length (L_ϕ) and spin-relaxation length (L_{so})) versus
temperature for three GeSn/Ge heterostructures.

at a temperature lower than 4 K, the $\tau_\phi \propto T^{-1}$ relationship should hold. The hole-hole scattering mechanism also justifies our discussion (Fig. 4-10 (a)) that we observed an increasing phase-coherence time as the carrier density increases. The physical picture of hole-hole scattering can be depicted as a hole being influenced by the electric field generated by all other holes in the valence band. Therefore, the dephasing mechanism would be suppressed when the carrier density increases due to the stronger screening effect [107].

4-6 Summary

In summary, we analyzed the Rashba spin-orbit coupling in the GeSn/Ge heterostructures with three different Sn fractions of 6%, 9%, and 11% by fitting the WL/WAL patterns with the HLN formula. We observe the strongest Rashba SOC among all group-IV materials in the GeSn/Ge heterostructures. The strength of the Rashba SOC can be modulated by tuning the carrier density via gating. Transitions from WL to WAL were observed for all GeSn/Ge heterostructures, and the spin-relaxation and phase-coherence times were extracted by the magneto-conductivity measurement results. As the carrier density increases, the spin-relaxation time decreases due to the stronger Rashba SOC effect while the phase-coherence time increases slightly. Experimental results show that the GeSn/Ge heterostructures are in the spin-diffusive regime.

As the Sn fraction in GeSn increases, the spin-orbit coupling becomes weaker, which is attributed to the effects of compressive strains on the Rashba SOC coefficients. The k-cubic term (α_3) by the quantum confinement effect results in a z-direction quantization while the SOC-induced magnetic field leads to an in-plane (x-y plane) quantization. Two effects compete, and the stronger compressive strain and confinement potential enhance the z-direction quantization and further reduces the spin-splitting energy and thus, the Rashba SOC effect. Finally, the power law relation of $\tau_\phi \propto T^{-1}$ suggests that the hole-hole interaction is the dominant mechanism for the dephasing . Our results suggest undoped GeSn/Ge heterostructures are promising for group-IV based spintronics and fast qubit devices because of its strong SOC effects, gate tunability, and compatibility to the Si VLSI technology.
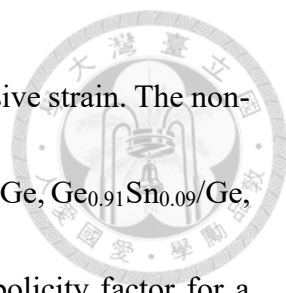
Chapter 5

Conclusion and Future Work

5-1 Conclusion

This thesis demonstrates the first 2DHGs in the undoped GeSn/Ge heterostructures with different Sn fractions of 6, 9, and 11%. The electrical and magneto-transport properties including SdH oscillations and quantum Hall plateaus are investigated by Hall measurements at cryogenic temperatures. Non-parabolicity effect on the hole effective mass and the SOC effect in the undoped GeSn/Ge heterostructures are also studied. The gated Hall bar devices of the GeSn/Ge heterostructures show transistor characteristics. The highest mobility measured by Hall measurements at 1.2 K is 20,000 cm^2/Vs with a power law relation of $\mu = p_{2D}^{\alpha}$ with $\alpha = 0.4{\sim}0.7$, which suggests that the mobility is limited by the background impurity scattering. Clear SdH oscillations and integer quantum Hall plateaus are observed under a magnetic field of up to 5 T. We extract the hole effective mass and quantum lifetime through the temperature-dependent SdH oscillations. The calculated Dingle ratios are close to one, indicating the large-angle scattering effect is dominant. The effective mass shows good linearity with the carrier density, which suggests the non-parabolicity effects are dominant in the GeSn QWs. The effective mass ranges from 0.07 m$_0$ to 0.10 m$_0$ with the carrier density varying from 2.7×10^{11} cm^{-2} to 6.1×10^{11} cm^{-2}. The effective mass is smaller in the GeSn/Ge

heterostructure with a higher Sn fraction due to the stronger compressive strain. The non-parabolicity factor is 8.0 eV^{-1}, 4.9 eV^{-1}, and 4.0 eV^{-1} for Ge$_{0.94}$Sn$_{0.06}$/Ge, Ge$_{0.91}$Sn$_{0.09}$/Ge, Ge$_{0.89}$Sn$_{0.11}$/Ge heterostructures, respectively. The smaller non-parabolicity factor for a higher Sn fraction is attributed to the weaker band-mixing between the HH and LH bands with a larger HH-LH splitting.

We also investigate the Rashba SOC effects by fitting the magneto-conductivity to the HLN formula. Transitions from WL to WAL are observed for all GeSn/Ge heterostructures. Phase-coherence time (τ_ϕ), spin-relaxation time (τ_{so}), spin-precession time (τ_{pre}), spin-splitting energy (Δ_{so}), and k-cubic Rashba coefficients (α_3) are extracted. Strongest Rashba SOC effects among all group-IV materials are observed in the GeSn/Ge heterostructure with a Sn fraction of 6 %, and the SOC strength can be modulated by gating. The spin-relaxation time varies up to 85% and the spin-splitting energy is enhanced by a factor of 2 by increasing the carrier density. Experimental results show that the mean free path is shorter than the spin-precession length, indicating the GeSn/Ge heterostructures are in the spin-diffusive regime. As the Sn fraction in GeSn increases, the spin-orbit coupling becomes weaker, which is attributed to the effects of compressive strains on the k-cubic Rashba coefficients.

5-2 Future work

According to what has been done in this thesis, there are three main directions which can be further explored:

1. Distinguish the Sn effect and strain effect on Rashba SOC

    The Rashba SOC effect is stronger when adding Sn into Ge crystals, but weaker under a larger compressive strain. The Sn effect and strain effect are intertwined in the GeSn/Ge heterostructures in this thesis. As the Sn fraction increases, the strain is also enhanced. By a careful design of the epitaxial structure in the future, the Sn effect and strain effect should be able to probe separately.

2. Investigation of SOC effects in bulk Ge(Sn)

    There are many surface states at the Ge(Sn) surface or the Ge(Sn)/oxide interface [125], which would create surface electric fields and lead to SIA and WAL close to the surface [62]. We can apply gate biases on a junctionless FET to balance the electric field induced by those surface defects to reach a flat band condition, where the electric field becomes zero and the WAL effects should be suppressed significantly. By doing so, we can study the influence of surface states on the Rashba SOC in Ge or GeSn.

3. <u>g-factor in the GeSn/Ge heterostructures.</u>
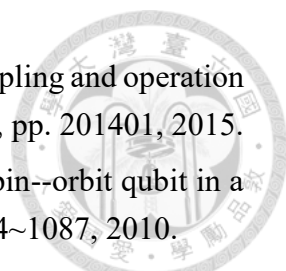
In spin-based quantum computing devices, a constant magnetic field is required to break the spin-degeneracy, and the resulting two energy states serve as the qubit "1" and "0". The splitting energy is called the Zeeman splitting energy ($\Delta_{Zeeman} = g\mu_B B$), where g is the g-factor and μ_B is the Bohr magneton. Therefore, a larger g-factor means that a relatively small magnetic field can be used to break the degeneracy. The reported g-factor of Ge is 28 in Ref. [33]. However, there is no work on the g-factors in a GeSn-based quantum well yet. By extracting the g-factors in the GeSn/Ge heterostructure, we can have a deeper understanding of the magneto-properties of the GeSn/Ge heterostructures for spin-based quantum computing applications.

In summary, those three directions focus on the quantum transport properties in the GeSn/Ge heterostructures, which have not been well-explored so far. Since GeSn has great potential for future electronic application, a thorough understanding of this material is important. The results of those projects will be very useful for both condensed matter physics and device applications.
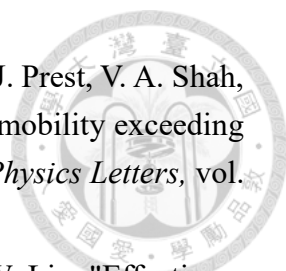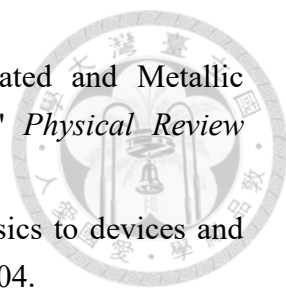
Bibliography

[1]   T. N. Theis, P. M. Solomon, "In quest of the "next switch": prospects for greatly reduced power dissipation in a successor to the silicon field-effect transistor," *Proceedings of the IEEE,* vol. 98, no. 12, pp. 2005~2014, 2010.

[2]   S. Sugahara, J. Nitta, "Spin-transistor electronics: an overview and outlook," *Proceedings of the IEEE,* vol. 98, no. 12, pp. 2124~2154, 2010.

[3]   O. Golonzka, J. Alzate, U. Arslan, M. Bohr, P. Bai, J. Brockman, B. Buford,C. Connor, N. Das, B. Doyle, T. Ghani, F. Hamzaoglu, P. Heil, P. Hentges, R. Jahan, D. Kencke, B. Lin, M. Lu, M. Mainuddin, M. Meterelliyoz, P. Nguyen, D. Nikonov, K. O'brien, "MRAM as embedded non-volatile memory solution for 22FFL FinFET technology," in *2018 International Electron Devices Meeting*, San Francisco, CA, USA, 2018.

[4]   W. J. Gallagher, E. Chien, T. Chiang, J. Huang, M. Shih, C. Y. Wang, C. Bair, G. Lee, Y. Shih, C. Lee, R. Wang, K. Shen, J. J. Wu, W. Wang, H. Chuang, "Recent progress and next directions for embedded MRAM technology," in *Symposium on VLSI Circuits*, Kyoto, Japan, 2019.

[5]   N. Sato, F. Xue, R. M. White, C. Bi, S. X. Wang, "Two-terminal spin-orbit torque magnetoresistive random access memory," *Nature Electronics,* vol. 1, no. 9, pp. 508~511, 2018.

[6]   S. Datta, B. Das, "Electronic analog of the electro-optic modulator," *Applied Physics Lettrers,* vol. 56, no. 7, pp. 665, 1990.

[7]   D. D. Awschalom, M. E. Flatt´e, "Challenges for semiconductor spintronics," *Nature Physics,* vol. 3, no. 3, pp. 153~159, 2007.

[8]   P. Chuang, S.-C. Ho, L. W. Smith, F. Sfigakis, M. Pepper, C.-H. Chen, J.-C. Fan, J. P. Griffiths, I. Farrer, H. E. Beere, G. A. C. Jones, D. A. Ritchie, T.-M. Chen, "All-electric all-semiconductor spin field-effect transistors," *Nature Nanotechnology,* vol. 10, no. 1, pp. 35~39, 2015.

[9]   H. C. Koo, J. H. Kwon, J. Eom, J. Chang, S. H. Han, M. Johnson, "Control of spin precession in a spin-injected field effect transistor," *Science,* vol. 325, no. 5947, pp. 1515~1518, 2010.

[10]   R. Winkler, S. Papadakis, E. De Poortere, M. Shayegan, Spin-Orbit Coupling in Two-Dimensional Electron and Hole Systems, Springer, 2003.

[11]   M. Veldhorst, R. Ruskov, C. H. Yang, J. C. C. Hwang, F. E. Hudson, M. E. Flatte,
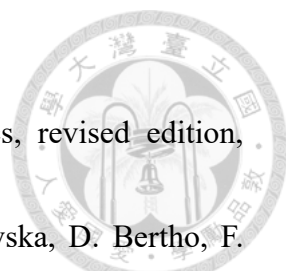
C. Tahan, K. M. Itoh, A. Morello, A. S. Dzurak, "Spin-orbit coupling and operation of multivalley spin qubits," *Physical Review B,* vol. 92, no. 20, pp. 201401, 2015.

[12] S. Nadj-Perge, S. Frolov, E. Bakkers, L. P. Kouwenhoven, "Spin--orbit qubit in a semiconductor nanowire," *Nature,* vol. 468, no. 7327, pp. 1084~1087, 2010.

[13] N. W. Hendrickx, D. P. Franke, A. Sammak, G. Scappucci, M. Veldhorst, "Fast two-qubit logic with holes in germanium," *Nature,* vol. 577, no. 7791, pp. 487~491, 2020.

[14] C.-T. Chou, N. T. Jacobson, J. E. Moussa, A. D. Baczewski, Y. Chuang, C.-Y. Liu, "Weak anti-localization of two-dimensional holes in germanium beyond the diffusive regime," *Nanoscale,* vol. 10, no. 44, pp. 20559~20564, 2018.

[15] R. Winkler, D. Culcer, S. J. Papadakis, B. Habib, M. Shayegan, "Spin orientation of holes in quantum wells," *Semiconductor Science and Technology,* vol. 23, no. 11, pp. 114017, 2008.

[16] C.-T. Tai, P.-Y. Chiu, C.-Y. Liu, H.-S. Kao, C. T. Harris, T.-M. Lu, C.-T. Hsieh, S.-W. Chang, J.-Y. Li, "Strain Effects on Rashba Spin-Orbit Coupling of Two-Dimensional Hole Gases in GeSn/Ge Heterostructures," *Advanced Material Under review.*

[17] Y. Huang, F. Lu, Y. Tsou, H. Ye, S. Lin, W. Huang, C. W. Liu, "Vertically Stacked Strained 3-GeSn-Nanosheet pGAAFETs on Si Using GeSn/Ge CVD Epitaxial Growth and the Optimum Selective Channel Release Process," *IEEE Electron Device Letters,* vol. 39, no. 9, pp. 1274~1277, 2018.

[18] V. Umansky, M. Heiblum, Y. Levinson, J. Smet, J.Nubler, M. Dole, "MBE growth of ultra-low disorder 2DEG with mobility exceeding $35x10^6$ cm^2/Vs," *Journal of Crystal Growth,* vol. 311, no. 7, pp. 1658~1661, 2009.

[19] M. Y. Melnikov, A. A. Shashkin, V. T. Dolgopolov, S.-H. Huang, C. W. Liu, S. V. Kravchenko, "Ultra-high mobility two-dimensional electron gas in a SiGe/Si/SiGe quantum well," *Applied Physics Letters,* vol. 106, no. 9, pp. 092102, 2015.

[20] C. H. Yang, W. H. Lim, F. A. Zwanenburg, A. S. Dzurak, "Dynamically controlled charge sensing of a few-electron silicon quantum dot," *AIP Advances,* vol. 1, no. 4, pp. 042111, 2011.

[21] J. H. Davies, The physics of low-dimensional semiconductors: an introduction, Cambridge university press, 1998.

[22] K. Saeedi, S. Simmons, J. Z. Salvail, P. Dluhy, H. Riemann, N. V. Abrosimov, P. Becker, H. -J. Pohl, J. J. L. Morton, M. L. W. Thewalt, "Room-Temperature Quantum Bit Storage Exceeding 39 Minutes Using Ionized Donors in Silicon-28,"

Science, vol. 342, no. 6160, pp. 830~833, 2013.

[23] D. Sabbagh, N. Thomas, J. Torres, R. Pillarisetty, P. Amin, H.C. George, J. Roberts, L. Lampert, L. Massa, S.V. Amitonov, J.M. Boter, G. Droulers, H.G.J. Eenink, M. van Hezel, D. Donelson, M. Veldhorst, L.M.K. Vandersypen, J.S. Clarke, G. Scappucci et.al., "Quantum Transport Properties of Industrial ^{28}Si/^{28}SiO2," *Physical Review Applied,* vol. 12, no. 1, pp. 014013, 2019.

[24] N. W. Hendrickx, W. I. L. Lawrie, M. Russ, F. van Riggelen, S. L. de Snoo, R. N. Schouten, A. Sammak, G. Scappucci, M. Veldhorst, "A four-qubit germanium quantum processor," *arXiv preprint arXiv:2009.04268,* 2020.

[25] Y. He, S. K. Gorman, D. Keith, L. Kranz, J. G. Keizer, M. Y. Simmons, "A two-qubit gate between phosphorus donor electrons in silicon," *Nature,* vol. 571, no. 7765, pp. 371~375, 2019.

[26] M. Veldhorst, C. H. Yang, J. C. C. Hwang, W. Huang, J. P. Dehollain, J. T. Muhonen, S. Simmons, A. Laucht, F. E. Hudson, K. M. Itoh, A. Morello, A. S. Dzurak, "A two-qubit logic gate in silicon," *Nature,* vol. 526, no. 7573, pp. 410~414, 2015.

[27] M. Veldhorst, J. C. C. Hwang, C. H. Yang, A. W. Leenstra, B. de Ronde, J. P. Dehollain, J. T. Muhonen, F. E. Hudson, K. M. Itoh, A. Morello, A. S. Dzurak, "An addressable quantum dot qubit with fault-tolerant control-fidelity," *Nature Nanotechnology,* vol. 9, no. 12, pp. 981~985, 2014.

[28] Y. Xu, F. K. Unseld, A. Corna, A. M. J. Zwerver, A. Sammak, D. Brousse, N. Samkharadze, S. V. Amitonov, M. Veldhorst, G. Scappucci, R. Ishihara, L. M. K. Vandersypen, "On-chip Integration of Si/SiGe-based Quantum Dots and Switched-capacitor Circuits," *Applied Physics Letters,* vol. 117, no. 14, p. 144002, 2020.

[29] L. Petit, H. G. J. Eenink, M. Russ, W. I. L. Lawrie, N. W. Hendrickx, S. G. J. Philips, J. S. Clarke, L. M. K. Vandersypen, M. Veldhorst, "Universal quantum logic in hot silicon qubits," *Nature,* vol. 580, no. 7803, pp. 355~359, 2020.

[30] J.M. Boter, X. Xue, T. Krähenmann, T.F. Watson, V.N. Premakumar, D.R. Ward, D.E. Savage, M.G. Lagally, M. Friesen, S.N. Coppersmith, M.A. Eriksson, R. Joynt, L.M.K. Vandersypen, "Spatial Noise Correlations in a Si/SiGe Two-Qubit Device from Bell State Coherences," *Physical Review B,* vol. 101, no. 23, pp. 235133, 2020.

[31] Z. Wilamowski, W. Jantsch, H. Malissa, U. Rossler, "Evidence and evaluation of the Bychkov-Rashba effect in SiGe/Si/SiGe quantum wells," *Physical Review B,* vol. 66, no. 19, pp. 195315, 2002.

[32] A. Dobbie, M. Myronov, R. J. H. Morris, A. H. A. Hassan, M. J. Prest, V. A. Shah, E. H. C. Parker, T. E. Whall, D. R. Leadley, "Ultra-high hole mobility exceeding one million in a strained germanium quantum well," *Applied Physics Letters,* vol. 101, no. 17, pp. 172108, 2012.

[33] T. M. Lu, C. T. Harris, S.-H. Huang, Y. Chuang, J.-Y. Li, C. W. Liu, "Effective g factor of low-density two-dimensional holes in a Ge quantum well," *Applied Physics Letters,* vol. 111, no. 10, pp. 102108, 2017.

[34] W. J. Hardy, C. T. Harris, Y. -H. Su, Y. Chuang, J. Moussa, L. N. Maurer, J. -Y. Li, T. -M. Lu, D. R. Luhman, "Single and double hole quantum dots in strained Ge / SiGe quantum wells," *Nanotechnology,* vol. 30, no. 21, pp. 215202, 2019.

[35] C. Morrison, M. Myronov, "Electronic transport anisotropy of 2D carriers in biaxial compressive strained germanium," *Applied Physics Letters,* vol. 111, no. 19, pp. 192103, 2017.

[36] R. Moriya, K. Sawano, Y. Hoshi, S. Masubuchi, Y. Shiraki, A. Wild, C. Neumann, "Cubic Rashba Spin-Orbit Interaction of a Two-Dimensional Hole Gas in a Strained-Ge/SiGe Quantum Well," *Physical Review Letters,* vol. 113, no. 8, pp. 086601, 2014.

[37] C. Morrison, P. Wiśniewski, S. D. Rhead, J. Foronda, D. R. Leadley, M. Myronov, "Observation of Rashba zero-field spin splitting in a strained germanium 2D hole gas," *Applied Physics Letters,* vol. 105, no. 18, pp. 182401, 2014.

[38] K. S. Cho, T.-Y. Huang, H.-S. Wang, M.-G. Lin, T.-M. Chen, C.-T. Liang, Y. F. Chen, "Zero-field spin splitting in modulation-doped $Al_xGa_{1-x}N$/GaN two-dimensional electron systems," *Applied Physics Letters,* vol. 86, no. 22, pp. 222102, 2005.

[39] J. Luo, H. Munekata, F. F. Fang, P. J. Stiles, "Observation of the zero-field spin splitting of the ground electron subband in GaSb-InAs-GaSb quantum wells," *Physical Review B,* vol. 38, no. 14, pp. 10142, 1988.

[40] J. Luo, H. Munekata, F. F. Fang, P. J. Stiles, "Effects of inversion asymmetry on electron energy band structures in GaSb/InAs/GaSb quantum wells," *Physical Review B,* vol. 41, no. 11, pp. 7685, 1990.

[41] B. Das, D. C. Miller, S. Datta, R. Reifenberger, W. P. Hong, P. K. Bhattacharya, J. Singh, M. Jaffe, "Evidence for spin splitting in $In_xGa_{1-x}As/In_{0.52}Al_{0.48}As$ heterostructures as B→0," *Physical Review B,* vol. 39, no. 2, pp. 1411, 1989.

[42] Y.-H. Su, Y. Chuang, C.-Y. Liu, J.-Y. Li, T.-M. Lu, "Effects of surface tunneling of two-dimensional hole gases in undoped Ge/GeSi heterostructures," *Physical Review Materials,* vol. 1, no. 4, pp. 044601, 2017.
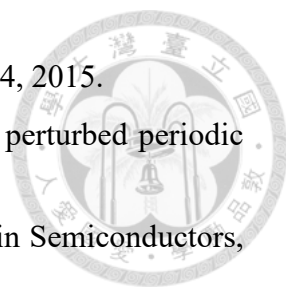
[43] Y. Gul, M. Myronov, S. N. Holmes, M. Pepper, "Activated and Metallic Conduction in p-Type Modulation-Doped Ge-Sn Devices," *Physical Review Applied,* vol. 14, no. 5, pp. 054064, 2020.

[44] D. J. Paul, "Si/SiGe heterostructures: from material and physics to devices and circuits," *Semiconductor Science and Technology,* pp. R75, 2004.

[45] H. S. Lan, C. W. Liu, "Band alignments at strained $Ge_{1-x}Sn_x$/relaxed $Ge_{1-y}Sn_y$ heterointerfaces," *Journal of Physics D: Applied Physics,* vol. 50, no. 13, pp. 13LT02., 2017.

[46] K. Laia, P. D. Ye, W. Pan, D. C. Tsui, S. A. Lyon, M. Mühlberger, F. Schäffler, "Modulation of the high mobility two-dimensional electrons in Si/SiGe using atomic-layer-deposited gate dielectric," *Applied Physics Letters,* vol. 87, no. 14, pp. 142103, 2005.

[47] K. A. Slinker, K. L. M. Lewis, C. C. Haselby, S. Goswami, L. J. Klein, J. O. Chu, S. N. Coppersmith, R. Joynt, R. H. Blick, M. Friesen, "Quantum dots in Si/SiGe 2DEGs with Schottky top-gated leads," *New Journal of Physics,* vol. 7, no. 1, pp. 246, 2005.

[48] D. Monroe, Y. H. Xie, E. A. Fitzgerald, P. J. Silverman, G. P. Watson, "Comparison of mobility-limiting mechanisms in high-mobility $Si_{1-x}Ge_x$ heterostructures," *Journal of Vacuum Science & Technology B,* vol. 11, no. 4, pp. 1731~1737, 1993.

[49] T. M. Lu, D. C. Tsui, C.-H. Lee, C. W. Liu, "Observation of two-dimensional electron gas in a Si quantum well with mobility of 1.6×10^6 cm^2/Vs," *Applied Physics Letters,* vol. 94, no. 18, pp. 182102, 2009.

[50] R. B. Dunford, N. Griffin, D. J. Paul, M. Pepper, D. J. Robbins, A. C. Churchill, W. Y. Leong, "Schottky gating high mobility $Si/Si_{1-x}Ge_x$ 2D electron systems," *Thin Solid Films,* vol. 369, no. 1, pp. 316~319, 2000.

[51] C. Kittel, P. McEuen, Introduction to solid state physics, Wiley New York, 1976.

[52] S. Datta, Electronic transport in mesoscopic systems, Cambridge university press, 1997.

[53] G. Dresselhaus, "Spin-orbit coupling effects in zinc blende structures," *Physical Review,* vol. 100, no. 2, pp. 580, 1955.

[54] Y. A. Bychkov, E. I. Rashba, "Oscillatory effects and the magnetic susceptibility of carriers in inversion layers," *Journal of Physics C: Solid State Physics,* vol. 17, no. 33, pp. 6039, 1984.

[55] H. Riechert, S. F. Alvarado, A. N. Titkov, V. I. Safarov, "Precession of the spin polarization of photoexcited conduction electrons in the band-bending region of

GaAs (110)," *Physical Review Letters,* vol. 52, no. 25, p. 2297, 1984.

[56] P. D. Dresselhaus, C. M. A. Papavassiliou, R. G. Wheeler, R. N. Sacks, "Observation of spin precession in GaAs inversion layers using antilocalization," *Physical Review Letters,* vol. 68, no. 1, pp. 106, 1992.

[57] J. J. Krich, B. I. Halperin, "Cubic Dresselhaus Spin-Orbit Coupling in 2D Electron Quantum Dots," *Physical Review Letters,* vol. 98, no. 22, pp. 226802, 2007.

[58] F. Herling, C. Morrison, C. S. Knox, S. Zhang, O. Newell, M. Myronov, E. H. Linfield, C. H. Marrows, "Spin-orbit interaction in InAs/GaSb heterostructures quantified by weak antilocalization," *Physical Review B,* vol. 95, no. 15, pp. 155307, 2017.

[59] [Online]. Available: https://en.wikipedia.org/wiki/File:Sphalerite-unit-cell-depth-fade-3D-balls.png.

[60] L. Meier, G. Salis, I. Shorubalko, E. Gini, S. Schon, K. Ensslin, "Measurement of Rashba and Dresselhaus spin--orbit magnetic fields," *Nature Physics,* vol. 3, no. 9, pp. 650~654, 2007.

[61] S. D. Ganichev, V. V. Bel'kov, L. E. Golub, E. L. Ivchenko, P. Schneider, S. Giglberger, J. Eroms, J. D. Boeck, G. Borghs, W. Wegscheider, D. Weiss, W. Prettl, "Experimental separation of Rashba and Dresselhaus spin splittings in semiconductor quantum wells," *Physical Review Letters,* pp. 256601, 2004.

[62] P. J. Newton, R. Mansell, S. N. Holmes, M. Myronov, C. H. W. Barnes, "Weak localization and weak antilocalization in doped germanium epilayers," *Applied Physics Letters,* vol. 110, no. 6, pp. 062101, 2017.

[63] H. Nakamura, T. Koga, T. Kimura, "Experimental Evidence of Cubic Rashba Effect in an Inversion-Symmetric Oxide," *Physical Review Letters,* vol. 108, no. 20, pp. 206601, 2012.

[64] M. I. D'yakonov, V. A. Marushchak, V. I. Perel, A. N. Titkov, "The effect of strain on the spin relaxation of conduction electrons in Ill-V semiconductors," *Zh. Eksp. Teor. Fiz.*, vol. 60, pp. 1123, 1986.

[65] R. J. Elliott, "Theory of the effect of spin-orbit coupling on magnetic resonance in some semiconductors," *Physical Review,* vol. 96, no. 2, pp. 266, 1954.

[66] Y. Yafet, "g Factors and spin-lattice relaxation of conduction electrons," *Solid State Physics,* vol. 14, pp. 1~98, 1963.

[67] P. Boross, B. Dora, A. Kiss, F. Simon, "A unified theory of spin-relaxation due to spin-orbit coupling in metals and semiconductors," *Scientific Reports,* vol. 3, no. 1, pp. 1~5, 2013.

[68] J. Rammer, Quantum Transport Theory, Perseus Books, 1998.

[69] J. J. Sakurai, E. D. Commins, Modern quantum mechanics, revised edition, American Association of Physics Teachers, 1995.

[70] W. Knap, C. Skierbiszewski, A. Zduniak, E. Litwin-Staszewska, D. Bertho, F. Kobbi, J. L. Robert, G. E. Pikus, F. G. Pikus, S. V. Iordanskii, V. Mosser, K. Zekentes, Y. B. Lyanda-Geller, "Weak antilocalization and spin precession in quantum wells," *Physical Review B,* vol. 53, no. 7, pp. 3912, 1996.

[71] V. R. D'Costa, C. S. Cook, A. G. Birdwell, C. L. Littler, M. Canonico, S. Zollner, J. Kouvetakis, J. Menéndez, "Optical critical points of thin-film $Ge_{1-y}Sn_y$ alloys: A comparative $Ge_{1-y}Sn_y/Ge_{1-x}Si_x$ study," *Physical Review B,* vol. 73, no. 12, pp. 125207, 2006.

[72] M. Oehme, K. Kostecki, T. Arguirov, G. Mussler, K. Ye, M. Gollhofer, M. Schmid, M. Kaschel, R. A. Körner, M. Kittler, D. Buca,E. Kasper, J. Schulze, "GeSn Heterojunction LEDs on Si Substrates," *IEEE Photonics Technology Letters,* vol. 26, no. 2, pp. 187~189, 2013.

[73] J. Werner, M. Oehme, M. Schmid, M. Kaschel, A. Schirmer, E. Kasper, J. Schulze, "Germanium-tin pin photodetectors integrated on silicon grown by molecular beam epitaxy," *Applied Physics Letters,* vol. 98, no. 6, pp. 061108, 2011.

[74] S. Wirths, R. Geiger, N. von den Driesch, G. Mussler, T. Stoica, S. Mantl, Z. Ikonic, M. Luysberg, S. Chiussi, J.-M. Hartmann, H. Sigg, J. Faist, D. Buca, D. GrAtzmacher, "Lasing in direct-bandgap GeSn alloy grown on Si," *Nature Photonics,* vol. 9, no. 2, p. 88~92, 2015.

[75] Y.-S. Huang, C.-H. Huang, F.-L. Lu, C.-Y. Lin, H.-Y. Ye, I.-H. Wong, S.-R. Jan, H.-S. Lan, C. W. Liu, Y.-C. Huang, H. Chung, C.-P. Chang, S. S. Chu, S. Kuppurao, "Record High Mobility (428 cm^2/Vs) of CVD-grown Ge/Strained $Ge_{0.91}Sn_{0.09}$ /Ge Quantum Well p-MOSFETs," in *IEEE International Electron Devices Meeting (IEDM)*, San Francisco, CA, USA, 2016.

[76] T.-H. Liu, P.-Y. Chiu, Y. Chuang, C.-Y. Liu, C.-H. Shen, G.-L. Luo, J.-Y. Li, "High-Mobility GeSn n-Channel MOSFETs by Low-Temperature Chemical Vapor Deposition and Microwave Annealing," *IEEE Electron Device Letters,* vol. 39, no. 4, pp. 468~471, 2018.

[77] H.-S. Lan, C. W. Liu, "Hole Effective Mass of Strained $Ge_{1-x}Sn_x$ Alloys P-Channel Quantum-Well MOSFETs on (001),(110), and (111) Ge Substrates," *ECS Transactions,* vol. 75, no. 8, pp. 571, 2016.

[78] T. M. Lu, Z. F. Li, D. C. Tsui, M. J. Manfra, L. N. Pfeiffer, K. W. West, "Cyclotron mass of two-dimensional holes in (100) oriented Ga As/ Al Ga As

heterostructures," *Applied Physics Letters,* vol. 92, no. 1, pp. 012109, 2008.

[79] K. Sawano, Y. Kunishi, Y. Shiraki, K. Toyama, T. Okamoto, N. Usami, and K. Nakagawa, "Strain dependence of hole effective mass and scattering mechanism in strained Ge channel structures," *Applied Physics Letters,* vol. 95, no. 12, pp. 162103, 2006.

[80] B. Rößner, G. Isella, H. V. Känel, "Effective mass in remotely doped Ge quantum wells," *Applied Physics Letters,* vol. 82, no. 5, pp. 754, 2003.

[81] M. Lodari, A. Tosato, D. Sabbagh, M. A. Schubert, G. Capellini, A. Sammak, M. Veldhorst, G. Scappucci, "Light effective hole mass in undoped Ge/SiGe quantum wells," *Physical Review B,* vol. 100, no. 4, pp. 041304, 2019.

[82] A. Baskaran, P. Smereka, "Mechanisms of stranski-krastanov growth," *Journal of Applied Physics,* vol. 111, no. 4, pp. 044321, 2012.

[83] H.-C. Luan, D. R. Lim, K. K. Lee, K. M. Chen, J. G. Sandland, K. Wada, L. C. Kimerling, "High-quality Ge epilayers on Si with low threading-dislocation densities," *Applied Physics Letters,* vol. 75, no. 19, pp. 2909, 1999.

[84] T. Tsukamoto, N. Hirose, A. Kasamatsu, T. Mimura, T. Matsui, Y. Suda, "Investigation of Sn surface segregation during GeSn epitaxial growth by Auger electron spectroscopy and energy dispersive x-ray spectroscopy," *Applied Physics Letters,* vol. 106, no. 5, pp. 052103, 2015.

[85] H. Li, Y. X. Cui, K. Y. Wu, W. K. Tseng, H. H. Cheng, H. Chen, "Strain relaxation and Sn segregation in GeSn epilayers under thermal treatment," *Applied Physics Letters,* vol. 102, no. 25, pp. 251907, 2013.

[86] T. K. P. Luong, M. T. Dau, M. A. Zrir, M. Stoffel, V. Le Thanh, M. Petit, A. Ghrib, "Control of tensile strain and interdiffusion in Ge/Si (001) epilayers grown by molecular-beam epitaxy," *Journal of Applied Physics,* vol. 114, no. 8, pp. 083504, 2013.

[87] G.-E. Chang, S.-W. Chang, S. L. Chuang, "Strain-Balanced Ge_zSn_{1-z}–$Si_xGe_ySn_{1-x-y}$ Multiple-Quantum-Well Lasers," *IEEE Journal of Quantum Electronics,* vol. 46, no. 12, pp. 1813~1820, 2010.

[88] Y.-H. Su, K.-Y. Chou, Y. Chuang, T.-M. Lu, J.-Y. Li, "Electron mobility enhancement in an undoped Si/SiGe heterostructure by remote carrier screening," *Journal of Applied Physics,* vol. 125, no. 23, pp. 235705, 2019.

[89] K.-Y. Chou, N.-W. Hsu, Y.-H. Su, C.-T. Chou, P.-Y. Chiu, Y. Chuang, J.-Y. Li, "Temperature dependence of DC transport characteristics for a two-dimensional electron gas in an undoped Si/SiGe heterostructure," *Applied Physics Letters,* vol.

112, no. 8, pp. 083502, 2018.

[90] K.-Y. Chou, "DC and AC Characteristic of Two-Dimensional Electron Gases in Undoped Silicon/Silicon Germanium Heterostructures," *M.S. thesis, NTU, Taipei, Taiwan,* 2016.

[91] Y.-H. Su, "Effects of surface tunneling in undoped Si/SiGe and Ge/GeSi heterostructures," *M.S. thesis, NTU, Taipei, Taiwan,* 2017.

[92] N.-W. Hsu, "Cryogenic non-volatile memory devices based on undoped Si/SiGe heterostructures," *M.S. thesis, NTU, Taipei, Taiwan,* 2019.

[93] M. V. Fischetti, S. E. Laux, "Band structure, deformation potentials, and carrier mobility in strained Si, Ge, and SiGe alloys," *Journal of Applied Physics,* vol. 80, no. 4, pp. 2234, 1996.

[94] Saumitra R. Mehrotra, Abhijeet Paul, Gerhard Klimeck, "Atomistic approach to alloy scattering in $Si_{1-x}Ge_x$," *Applied Physics Letters,* vol. 98, no. 17, pp. 173503, 2011.

[95] D. Laroche, S.-H. Huang, Y. Chuang, J.-Y. Li, C. W. Liu, T. M. Lu, "Magneto-transport analysis of an ultra-low-density two-dimensional hole gas in an undoped strained Ge/SiGe heterostructure," *Applied Physics Letters,* vol. 108, no. 23, pp. 233504, 2016.

[96] A. Gold, "Mobility and metal–insulator transition of the two-dimensional electron gas in SiGe/Si/SiGe quantum wells," *Journal of Applied Physics,* vol. 108, no. 6, pp. 063710, 2010.

[97] I. B. Berkutov, V. V. Andrievskii, Yu. F. Komnik, Yu. A. Kolesnichenko, "Magnetotransport studies of SiGe-based p-type heterostructures: Problems with the determination of effective mass," *Low Temperature Physics,* vol. 38, no. 12, pp. 1145~1152, 2012.

[98] T. E. Whall, N. L. Mattey, A. D. Plews, P. J. Phillips, 0. A. Mironov, R. J. Nicholas, M. J. Kearney, "Effective mass and quantum lifetime in a $Si/Si_{0.87}Ge_{0.13}/Si$ two-dimensional hole gas," *Applied Physics Letters,* vol. 64, no. 3, pp. 357, 1994.

[99] A. Gold, "Scattering time and single-particle relaxation time in a disordered two-dimensional electron gas," *Physical Review B,* vol. 38, no. 15, pp. 10798, 1988.

[100] D. Laroche, S.-H. Huang, E. Nielsen, Y. Chuang, J.-Y. Li, C.-W. Liu, T.-M. Lu, "Scattering mechanisms in shallow undoped Si/SiGe quantum wells," *AIP Advances,* vol. 5, no. 10, pp. 107106, 2015.

[101] X. Mi, T. M. Hazard, C. Payette, K. Wang, D. M. Zajac, J. V. Cady, J. R. Petta, "Magnetotransport studies of mobility limiting mechanisms in undoped Si/SiGe

heterostructures," *Physical Review B,* vol. 92, no. 3, pp. 035304, 2015.

[102] J. M. Lüttinger, W. Kohn, "Motion of electrons and holes in perturbed periodic fields," *Physical Review,* vol. 97, no. 4, pp. 869, 1955.

[103] G. L. Bir, G. E. Pikus, Symmetry and Strain-Induced Effects in Semiconductors, New York: John Wiley & Sons, 1974.

[104] S. L. Chuang, Physics of Photonic Devices, 2nd ed., New Jersey: John Wiley & Sons,Hoboken, 2009.

[105] S.-Q. Liu, S.-T. Yen, "Extraction of eight-band k·p parameters from empirical pseudopotentials for GeSn," *Journal of Applied Physics,* vol. 125, no. 24, pp. 245701, 2019.

[106] B. K. Ridley, Electrons and phonons in semiconductor multilayers, Vol. 5, Cambridge University Press, 2009.

[107] S. McPhail, C. E. Yasin, A. R. Hamilton, M. Y. Simmons, E. H. Linfield, M. Pepper, "Weak localization in high-quality two-dimensional systems," *Physical Review B,* vol. 70, no. 24, pp. 245311, 2004.

[108] S. Hikami, A. I. Larkin, Y. Nagaoka, "Spin-orbit interaction and magnetoresistance in the two dimensional random system," *Progress of Theoretical Physics,* vol. 63, no. 2, pp. 707~710, 1980.

[109] C. Morrison, C. Casteleiro, D. R. Leadley, M. Myronov, "Complex quantum transport in a modulation doped strained Ge quantum well heterostructure with a high mobility 2D hole gas," *Applied Physics Letters,* vol. 109, no. 10, pp. 102103, 2016.

[110] L. E. Golub, "Weak antilocalization in high-mobility two-dimensional systems," *Physical Review B,* vol. 71, no. 23, pp. 235310, 2005.

[111] J. L. Devore, Probability and Statistics for Engineering and the Sciences, Spinger, 2008.

[112] T. Koga, J. Nitta, T. Akazaki, H. Takayanagi, "Rashba spin-orbit coupling probed by the weak antilocalization analysis in InAlAs/InGaAs/InAlAs quantum wells as a function of quantum well asymmetry," *Physical Review Letters,* vol. 89, no. 4, pp. 046801, 2002.

[113] S. A. Studenikin, P. T. Coleridge, N. Ahmed, P. J. Poole, A. Sachrajda, "Experimental study of weak antilocalization effects in a high-mobility $In_xGa_{1-x}As$/InP quantum well," *Physical Review B,* vol. 68, no. 3, pp. 035317, 2003.

[114] G. M. Minkov, A. A. Sherstobitov, A. V. Germanenko, O. E. Rut, V. A. Larionova, B. N. Zvonkov, "Antilocalization and spin-orbit coupling in the hole gas in strained

GaAs/In$_x$Ga$_{1-x}$As/GaAs quantum well heterostructures," *Physical Review B,* vol. 71, no. 16, pp. 165312, 2005.

[115] B. Habib, J. Shabani, E. P. De Poortere, M. Shayegan, R. Winkler, "Tuning of the spin-orbit interaction in two-dimensional GaAs holes via strain," *Physical Review B,* vol. 75, no. 15, pp. 153304, 2007.

[116] N. W. Ashcroft, N. D. Mermin, Solid state physics, New York: Holt, Rinehart and Winston, 1976.

[117] B. Habib, E. Tutuc, S. Melinte, M. Shayegan, D. Wasserman, S. A. Lyon, R. Winkler, "Negative differential Rashba effect in two-dimensional hole systems," *Applied Physics Letters,* vol. 85, no. 15, pp. 3151, 2004.

[118] K. Zelazna, M. Polak, P. Scharoch, J. Serafinczuk, M. Gladysiewicz, J. Misiewicz,, "Electronic band structure of compressively strained Ge$_{1-x}$Sn$_x$ with x< 0.11 studied by contactless electroreflectance," *Applied Physics Letters,* vol. 106, no. 14, pp. 142102, 2015.

[119] R. Chen, S. Gupta, Y.-C. Huang, Y. Huo, C. W. Rudy, E. Sanchez, Y. Kim, T. I. Kamins, K. C. Saraswat, J. S. Harris, "Demonstration of a Ge/GeSn/Ge Quantum-Well Microdisk Resonator on Silicon: Enabling High-Quality Ge(Sn) Materials for Micro- and Nanophotonics," *Nano Letters,* vol. 14, no. 1, pp. 37~43, 2014.

[120] K.-M. Haendel, R. Winkler, U. Denker, O. Schmidt, R. J. Haug, "Giant Anisotropy of Zeeman Splitting of Quantum Confined Acceptors in Si/Ge," *Physical Review Letters,* vol. 96, no. 8, pp. 086403, 2006.

[121] R. Danneau, O. Klochan, W. Clarke, L. Ho, A. Micolich, M. Simmons, A. Hamilton, "Zeeman Splitting in Ballistic Hole Quantum Wires," *Physical Review Letters,* vol. 97, no. 2, pp. 026403, 2006.

[122] R. Winkler, H. Noh, E. Tutuc, M. Shayegan, "Anomalous Rashba spin splitting in two-dimensional hole systems," *Physical Review B,* vol. 65, no. 15, pp. 155303, 2002.

[123] J. J. Lin, J. P. Bird, "Recent experimental studies of electron dephasing in metal and semiconductor mesoscopic structures," *Journal of Physics: Condensed Matter,* vol. 14, no. 18, pp. R501~R596, 2002.

[124] K. K. Cho, D. C. Tsui, "Dephasing time and one-dimensional localization of two-dimensional electrons in GaAs/Al$_x$Ga$_{1-x}$As heterostructures," *Physical Review B,* vol. 36, no. 14, pp. 7751, 1987.

[125] J. Chen, H.-G Piao, Z. Luo, X. Zhang, "Enhanced linear magnetoresistance of germanium at room temperature due to surface imperfection," *Applied Physics*

Letters, vol. 106, no. 17, pp. 173503, 2015.

Related Publication List

Journal

1. C.-T. Tai, P.-Y. Chiu, C.-Y. Liu, H.-S. Kao, C. T. Harris, T.-M. Lu, C.-T. Hsieh, S.-W. Chang, and J.-Y. Li, "Strain Effects on Rashba Spin-Orbit Coupling of Two-dimensional Hole Gases in GeSn/Ge Heterostructures"
(under revision by Advanced Materials)
2. C.-T. Tai, P.-Y. Chiu, C.-Y. Liu, H.-S. Kao, C. T. Harris, T.-M. Lu, C.-T. Hsieh, S.-W. Chang, and J.-Y. Li, "Effect of Non-parabolicity in Valence Band on Hole Effective Mass in GeSn/Ge Heterostructures"
(manuscript to be submitted to Physical Review B)

Conference

1. C.-T. Tai, P.-Y. Chiu, Y. Chuang, C.-Y. Liu, T.-M. Wang, C.-Y. Lin, C. T. Harris, T.-M. Lu, and J.-Y. Li, "Weak Anti-localization in Undoped Ge/GeSn Heterostructures," *2020 APS March Meeting* Session L42, Denver, CO, U.S.A., Mar. 2 – 6, 2020. (Oral)
2. C.-T. Tai, P.-Y. Chiu, Y. Chuang, C.-Y. Liu, T.-M. Wang, C.-Y. Lin, C. T. Harris, T.-M. Lu, and J.-Y. Li, "Demonstration of Two-dimensional Hole Gases (2DHG) in Strained GeSn Quantum Wells," *2020 APS March Meeting* Session D27, Denver, CO, U.S.A., Mar. 2 – 6, 2020. (Oral)
3. C.-T. Tai, P.-Y. Chiu, Y. Chuang, C.-Y. Liu, T.-M. Wang, C.-Y. Lin, C. T. Harris, T. M. Lu, and J.-Y. Li, "Magneto-transport and effective mass of two dimensional hole gases in modulation- doped and undoped GeSn/Ge heterostructures," *2020 Annual Meeting of the Physical Society of Taiwan*, Ping-Tung, Taiwan, Feb. 5 – 7, 2020. (Oral)
4. C.-T. Tai, P.-Y. Chiu, C.-Y. Lin, C.-Y. Liu, H.-S. Kao, C. T. Harris, T.-M. Lu, and J.-Y. Li, "Rashba Spin-Orbit Coupling in GeSn/Ge Heterostructures for Quantum Computing Applications," *2020 International Workshop on Quantum Computing*, New Taipei City, Taiwan, Aug. 31 – Sep.1, 2020 (Poster)